Universidad de Alcalá

Programa de Doctorado en
Tecnologías de la Información Geográfica

DEVELOPMENT AND ANALYSIS OF GLOBAL LONG–TERM BURNED AREA BASED ON AVHRR-LTDR DATA

Tesis Doctoral presentada por
GONZALO OTÓN AZOFRA

Director:
DR. EMILIO CHUVIECO SALINERO

Alcalá de Henares, 2021.

"Sic Gloria Labore"
("En el trabajo está la gloria")
Lema del primer escudo de Madrid

CONTENTS

AGRADECIMIENTOS

Me siento realmente afortunado de poder dedicar estas palabras que vienen a continuación y de haber tenido esta oportunidad profesional en la vida. Agradezco el poder haber encontrado tanta gente buena en mi camino, que me hayan permitido lograr mis objetivos profesionales y personales. El camino no ha sido fácil pero cuando lo compartes con personas que te aprecian, nunca dejas de creer. En mi vida me siento agradecido a aquellos que han confiado en mí, cuando quizás otras personas no lo harían. Cada día trabajo para ser una mejor persona y un mejor profesional, aplicando las enseñanzas de todos aquellos que habéis estado a mi lado. Por ello, os dedico estas palabras de agradecimiento, que, aunque siempre se van a quedar escasas, reflejan mis sentimientos.

Mi mentor Emilio Chuvieco, estaré eternamente agradecido por la oportunidad que me has dado y la profesión que me has enseñado. La paciencia, el compromiso, la profesionalidad y el cariño con los que me has tratado todos estos años han sido realmente de un valor incalculable. El apoyo que me has ofrecido en todos los momentos han sido vitales para que hayamos triunfado. Gracias de corazón Emilio.

Mis queridos padres, esto también es vuestro triunfo. Los años de trabajo, de sacrificios, de esfuerzos para darme la mejor vida posible y los mejores estudios han merecido la pena. Gracias a vosotros he cumplido mis sueños y me he convertido en la persona que quería ser. Siempre he contado con vuestra infinita ayuda, comprensión y entrega. Solo os puedo decir desde lo más profundo de mi ser, Gracias.

A mi pareja Geovanna, gracias por hacerme feliz, me siento afortunado de compartir mi vida contigo. Gracias por tu paciencia y comprensión en estos años. Has llenado mi vida de alegría y siempre has estado a mi lado ante cualquier situación. Aprecio tus consejos, tus ganas de escucharme, tu confianza y tu dedicación. Tu apoyo y tu sonrisa han hecho todos mis días más llevaderos y bonitos.

Mis íntimos amigos, siempre habéis estado a mi lado. Joshua, anaia, te agradezco todos tus consejos, conversaciones, ideas, apoyo y toda tu ayuda. Rubén, siempre estás ahí para ayudar, hablar, aconsejar, animar o lo que haga falta, con la mejor de tus sonrisas. Magí, aprecio nuestras conversaciones, tu apoyo, tu dedicada experiencia y tu ayuda, incluso en situaciones de peligro. Tarek, agradezco tu leal amistad, tus palabras, tu integridad y tu confianza. Pablo Barreira, te agradezco tus claros consejos y amena compañía. Alba, gracias por las buenas conversaciones, tu simpatía y tu confianza.

Mis apreciados doctores y grandes amigos, Lucre, Mariano y Alex Ariza. Gracias porque en todo momento he podido contar con vosotros para cualquier cosa, me habéis aconsejado, ayudado y animado.

Gracias al sótano y a mis amigos, que lo han llenado de buenos momentos, compañerismo y felicidad. Macarena, Pablo, Roberto, Nacho, y nuestros amigos de estancia German y Felix, gracias por vuestra alegría, confianza y apoyo. Fernando y Dani, os agradezco vuestra simpatía, acogida, y disposición a ayudar. A los amigos de COMPLUTIG, siempre personas simpáticas y trabajadoras. Dani Reinoso y Héctor, os agradezco que compartáis vuestra experiencia y simpatía con esa calidad humana.

Gracias a mi excepcional amigo, Luis Cepa, siempre tengo en mente tus consejos y tus sabias palabras. Mi buen amigo Miguel, siempre disponible para lo que haga falta. A mi gran amigo Ferdi y al Pop'n'Roll, gracias por todos los buenos momentos. My admired Janet, thank you for teaching me a new language, for your dedication, willingness to help and kindness.

Thank you to my supervisors from my international short-stays, José Miguel Pereira and Mike Flannigan. You helped me to be a better researcher, I appreciate your advice, your willingness to help and your hospitality. Both stays were a terrific experience. Thanks to the people that I met there and made my life easier: Giando, Roger, Luca, Rodrigo, Jaime, Dante, Xinlii, Samuel and Carol.

Gracias a Javier Salas y a su estupendo trabajo en la Escuela de doctorado. Su labor en la dirección ha sido sobresaliente, en beneficio de todos los doctorandos. Agradecer a Patxi y a la comisión académica al completo (Macu y Montse) su excelente labor y compromiso con los estudiantes y el doctorado. Siempre disponibles a ayudar, nos habéis ofrecido todo aquello que hemos pedido o necesitado para mejorar.

Mi agradecimiento al proyecto FireCCI y a la Agencia Espacial Europea por financiar la tesis, y permitir desarrollarme como investigador. También, al Departamento de Geología, Geografía y Medioambiente por acogerme y a la Universidad de Alcalá por entregarme dos ayudas de movilidad para realizar mis estancias en el extranjero.

A todos y a cada uno de vosotros, Gracias.
Gonzalo.

RESUMEN

La tesis doctoral propone la extensión temporal de la información global de área quemada obtenida a partir de imágenes de satélite. Un nuevo y consistente producto global de área quemada fue desarrollado ofreciendo datos por casi cuarenta años. El producto fue generado, analizado y validado, además de aplicado en el estudio global de tendencias espaciales y temporales. El trabajo fue financiado y desarrollado bajo el proyecto *Fire Disturbance* (Fire_cci) perteneciente al programa *Climate Change initiative* (CCI) de la Agencia Espacial Europea (ESA).

La motivación principal de esta tesis fue la ausencia de productos globales de área quemada en una escala temporal larga. Un producto de estas características contribuye a rellenar un vacío en la información necesaria para los modelos del clima y el estudio del cambio climático. Para llevar a cabo este objetivo fue preciso utilizar la base de datos de imágenes globales de satélite más extensa disponible, los datos pertenecientes al sensor *Advanced Very High Resolution Radiometer* (AVHRR) y de los satélites *National Oceanic and Atmospheric Administration* (NOAA). Las limitaciones que hubo que afrontar con imágenes de baja resolución son altas, aunque su potencial es muy elevado. Por ello, se hizo uso de un algoritmo novedoso que introdujo una visión renovada para afrontar estas limitaciones y detectar área quemada. Un innovador índice sintético y la obtención de proporciones de área quemada por cada pixel, hizo de este algoritmo y producto, únicos. Además, una validación y un estudio espacio-temporal fue realizado por primera vez en una serie temporal larga de casi cuarenta años. La tesis se estructura es seis capítulos: introducción, cuatro publicaciones en revistas internacionales y conclusiones.

El primer capítulo, es una introducción acerca de la importancia de los incendios forestales, y su relación con el cambio climático y el ciclo del carbono. Los incendios suponen la variable natural que más emisiones causan a la atmosfera y son de gran importancia en el estudio del clima y de los modelos climáticos. Para el estudio histórico de esta perturbación se han utilizado inventarios climáticos, y más recientemente con la entrada de la teledetección, productos de área quemada. Al inicio de esta tesis, existían estos productos para el periodo 2001 en adelante, y nuestro interés fue ampliar globalmente hacia atrás, veinte años, con el uso de información AVHRR. Además, una visión global de la tesis es detallada mediante la exposición de la hipótesis, objetivos y logros.

El segundo capítulo presenta el primer prototipo de producto de área quemada global con una serie temporal larga (1982-2017). El producto Beta fue derivado de datos *Land*

Long Term Data Record (LTDR) basados en imágenes del sensor AVHRR. Las limitaciones de los datos de entrada fueron descritas y el algoritmo fue detallado para conocer su funcionamiento. Los datos de entrada fueron convertidos en compuestos temporales de máxima temperatura, se aplicó un criterio simple para descartar nubes y se eliminaron las zonas no combustibles. Un índice sintético fue creado para mejorar la señal de quemado, teniendo en cuenta la variabilidad temporal. Se generaron modelos globales mensuales con *Random Forest* (RF) y fueron entrenados con clasificaciones binarias del producto de área quemada de la *National Aeronautics and Space Administration* (NASA), MCD64A1. El resultado de los modelos se ofreció como un producto de probabilidades de quemado, las cuales fueron binarizadas y dadas proporciones de área quemada mediante su análisis junto a MCD64A1. Este producto desarrollado fue el primero que presentó proporciones de área quemada, en vez de un producto binario. El producto final fue inter-comparado y evaluado con un buen comportamiento en zonas tropicales, pero con limitaciones en las zonas boreales. Además, presentaba unas marcadas tendencias relacionadas con el fin de vida de los satélites y su degradación. Este artículo fue publicado en la revista *Remote Sensing* con un índice de impacto de 6.6 en SCOPUS y 4.848 en *Journal Citation Reports* (JCR).

El tercer capítulo, mejora y corrige las principales limitaciones encontradas en el anterior prototipo. De tal forma, fue generado el primer producto global consistente de área quemada que cubre una serie temporal larga (1982-2018). En este capítulo el algoritmo desarrollado fue explicado y el producto evaluado. Los datos de entrada volvieron a ser el producto LTDR convertido en compuestos mensuales, y las zonas no combustibles. Las nubes fueron detectadas mediante un conjunto de criterios para su posterior descarte. El índice sintético, desarrollado en el producto anterior, fue empleado de nuevo. En esta ocasión, se generaron modelos mensuales de RF globales y boreales para mejorar la detección, ya que las zonas boreales presentaron limitaciones en el anterior producto Beta. Este nuevo modelo utilizó para el entrenamiento el producto FireCCI51, generado en el marco del mismo proyecto FireCCI a partir de datos *Moderate Resolution Imaging Spectroradiometer* (MODIS) de 250m. Este producto demostró ser más sensible a incendios pequeños y con mejor detección en áreas boreales que el MCD64A1. Como en el modelo Beta, el resultado de nuestro nuevo modelo RF fue un producto de probabilidades de quemado, las cuales fueron sometidas a un novedoso conjunto de criterios regionales para su binarización. Estos criterios tuvieron un mejor ajuste en cada una de las imágenes de probabilidades, sobre todo a los años pre-MODIS, y corrigió el principal efecto de degradación de los sensores. Tras aplicar estos criterios, se obtuvo las proporciones de área quemada de cada pixel, con un mejorado enfoque diseñado regionalmente. El producto final se compuso de los resultados de los modelos globales y boreales, siendo el único que ofrece proporciones de área quemada. Esta información fue evaluada, analizada e inter-comparada con productos globales de área quemada,

perímetros oficiales y estudios regionales. Las principales limitaciones a las que se hacía frente fueron solventadas con éxito, demostrando un buen funcionamiento global y regional del producto. Este trabajo fue publicado en la revista International *Journal of Applied Earth Observation and Geoinformation* con un índice de impacto de 12.5 en SCOPUS y 5.933 en JCR.

El cuarto capítulo es la validación del anterior producto de área quemada con una base de datos de referencia independientes basados en perímetros Landsat. La validación fue la más extensa de las desarrolladas para evaluar productos de área quemada, abarcando casi 30 años de perímetros. Debido a la gran diferencia de resoluciones entre los dos productos, 5km del producto de área quemada frente a 30m de los perímetros de validación, se aplicó un enfoque distinto al que comúnmente se usa en la validación de estos productos de área quemada. Además, de ser el único producto de área quemada que presenta proporciones de quemado como resultado. Por ello, utilizamos la metodología de *Pareto Boundary*, la cual fue adaptada para que estos cambios tan grandes de resolución no afecten a la validación y las proporciones de quemado puedan ser evaluadas. La validación mostró que el producto es estable temporalmente y que los periodos de AVHRR tienen una precisión similar. Este estudio fue publicado en las actas de la conferencia SPIE con un índice de impacto de 0.8 en SCOPUS.

El quinto capítulo presenta un análisis espacio-temporal de tendencias, derivadas del producto de área quemada desarrollado anteriormente. El producto es el más extenso hasta el momento, lo que hizo posible un análisis temporal de tendencias en una escala larga. Además, los resultados a medio plazo fueron comparados con otro producto de área quemada, FireCCI51. Ambos productos fueron consistentes en la serie temporal común. Al extender totalmente la serie, nuevas tendencias fueron apreciadas y fueron más pronunciadas. Este análisis fue publicado en la revista *Fire* con un índice de impacto de 3.7 en SCOPUS.

Por último, el sexto capítulo son las conclusiones generales de la tesis. Se destacan los logros obtenidos derivados de la investigación y las limitaciones tratadas. También, se exponen los pasos a seguir dentro de futuras líneas de investigación.

ABSTRACT

The doctoral thesis proposes the temporal extension of global information regarding burned area, obtained from satellite images. A new and consistent global burned area product was developed, offering data for almost forty years. The product was generated, analyzed and validated, as well as applied to the global study of spatial and temporal trends. The work was financed and developed under the Fire Disturbance (Fire_cci) Project, belonging to the Climate Change Initiative (CCI) program of the European Space Agency (ESA).

The main motivation of this thesis was the absence of global burned area products on a long-term scale. A long-term product of this type contributes to fill a gap in the information needed for climate models and the study of climate change. In order to achieve this objective, the most extensive database of global satellite images available, this being data acquired by the Advanced Very High Resolution Radiometer (AVHRR) sensor from the National Oceanic and Atmospheric Administration (NOAA) satellites, was used. With low resolution images, the limitations that must be faced are high, although their potential is very high too. Therefore, a novelty algorithm was developed in order to insert a renewed vision to cope with these limitations and detect burned area. An innovative synthetic index, and burned area proportions for each pixel, make this algorithm and product unique. Furthermore, and for the first time, a validation and a spatio-temporal analysis were carried out on a long time series of nearly forty years. The thesis is structured in six chapters: introduction, four publications in international journals, and conclusions.

The first chapter is an introduction emphasizing the importance of wildfires, and their effect on climate change and the carbon cycle. Fires are the natural variable that causes most emissions into the atmosphere, and they are of great importance in the study of climate and climate models. Historically, climate inventories have been used for the study of this disturbance, and more recently, with the entry of remote sensing, of burned area products. At the beginning of this thesis, these products existed for the period 2001 onwards, and our interest was to expand globally twenty years backwards, with the use of AVHRR information. In addition, an overview of the thesis is then detailed through an explanation of its hypothesis, objectives and achievements.

The second chapter, and first of the publications, is a presentation of the first global burned area prototype having a long time series (1982-2017). The Beta product was derived from the Land Long Term Data Record (LTDR) project based on AVHRR images. The limitations of the input data were described, and the operations of the algorithm

was detailed. The input data were converted into temporal composites of maximum temperature, a simple criterion was applied to discard clouds, and the unburnable areas were removed. A synthetic index was created to improve the burned signal, taking into account the temporal variability. Monthly global models were generated with Random Forest (RF) and trained with binary classifications of NASA's (National Aeronautics and Space Administration) burned area product (MCD64A1). The result of the models was offered as a product of burned area probabilities, these having been binarized, and burned area proportions were assigned through their analysis together with MCD64A1. The product thus developed was the first product that presented burned area proportions instead of a dichotomy product. The final product was inter-compared and evaluated with good performance in tropical areas, but with limitations in boreal regions. Moreover, this product presented significant trends related to the end of lifetime of the satellites and their degradation. This article was published in the Remote Sensing Journal with an impact index of 6.6 in SCOPUS and 4.848 in Journal Citation Reports (JCR).

The third chapter discusses the improvements and corrections of the main limitations found in the previous prototype, and the way in which this first consistent global product of burned area was generated, covering a long time series (1982-2018). In this chapter, the algorithm developed was explained and the product was evaluated. The input data were once again the LTDR product converted into monthly composites, plus that for the unburnable areas. The clouds were detected through a set of criteria for their later elimination. The synthetic index developed in the previous product was used again. On this occasion, global and boreal RF monthly models were generated to improve detection in boreal areas, since these presented limitations on the previous Beta product. This new model used the FireCCI51 product for training, generated within the framework of the same FireCCI project from Moderate Resolution Imaging Spectroradiometer (MODIS) 250m data. This product proved to be more sensitive to small fires and better detection of boreal areas than MCD64A1. As in the Beta model, the result of our new RF model was a product of burned probabilities, which were subjected to a novel set of regional criteria for binarization. These criteria had a better fit in each one of the probabilities images, especially in the pre-MODIS years, and corrected the main degradation effect of the sensors. After applying these criteria, the burned area proportions of each pixel were obtained with an improved regionally designed approach. The final product was composed of the results of global and boreal models, being the only one that offers burned area proportions. This information was evaluated, analyzed and inter-compared with global burned area products, official perimeters, and regional studies. The main limitations faced were successfully solved, demonstrating a good global and regional performance of the product. This work was

published in the International Journal of Applied Earth Observation and Geoinformation with an impact index of 12.5 in SCOPUS and 5.933 in JCR.

The fourth chapter is the validation of the previous burned area product with an independent reference database based on Landsat perimeters. The validation was the most extensive of those developed to evaluate burned area products, spanning almost 30 years of perimeters. Due to the large difference in resolutions between the two products, 5km of the burned area product versus 30m of the validation perimeters, a different approach was applied instead of that which is commonly used in the validation of these burned area products. In addition, it is the only burned area product which presents burned proportions as a result. Therefore, the Pareto Boundary methodology was used, which was adapted so that these large changes in resolution do not affect the validation and the burned area proportions can be evaluated. Validation showed that the product is temporally stable and that the AVHRR products have a similar accuracy. This study was published in the SPIE conference proceedings with an impact index of 0.8 in SCOPUS.

The fifth chapter presents a spatio-temporal analysis of trends derived from the burned area product which we had developed. The product is the most extensive yet created, making possible a temporal trend analysis on a long scale. Furthermore, the medium-term results were compared with another burned area product, FireCCI51. Both products were consistent in the common time series. By fully extending the series, new and more pronounced trends were appreciated. This analysis was published in the Fire Journal with an impact index of 3.7 in SCOPUS.

Finally, the sixth chapter contains the general conclusions of the thesis. The achievements derived from the research and the limitations discussed are highlighted. Also, the steps to follow in future research are presented.

Capítulo 1

INTRODUCCIÓN

1.1. Cambio climático e incendios forestales

El cambio climático es una de las grandes preocupaciones a las que la humanidad tiene que hacer frente en este siglo. La comunidad científica lo ha estado investigando durante décadas, tanto su comportamiento como la multitud de ciclos y variables relacionadas, alarmando de sus nefastas consecuencias. Especialmente, las emisiones atmosféricas causan un gran impacto en el sistema climático, alteran la atmosfera y su composición (GCOS 2011; Granier et al. 2011; Urbanski et al. 2008; Ward et al. 2012), e influyen en el calentamiento del clima y el cambio climático (Walker et al. 2020).

Directamente relacionado, los incendios forestales como fenómeno global (Flannigan et al. 2006; GCOS 2011), son un componente crítico del sistema terrestre. Esta perturbación provoca un alto impacto en los humanos y los ecosistemas (Bond et al. 2005). La pérdida de la vegetación, disminuye su efecto sumidero y la fijación del carbono (GCOS 2011; Granier et al. 2011; Urbanski et al. 2008; Ward et al. 2012), además de provocar un importante porcentaje de las emisiones de los gases de efecto invernadero (CO2, CH4, CO, N2O y NOX) por el proceso de combustión (Ramo et al. 2021). Tanto la perdida de sumideros como el aumento de emisiones, intensifican el cambio climático. Simultáneamente, los incendios son afectados por el cambio climático y las oscilaciones climáticas, particularmente cuando ocurren olas de calor y sequias severas (Chen et al. 2016; Hantson et al. 2015; Preisler et al. 2009).

1.1.1. Ciclo del carbono

En concreto, los incendios forestales afectan al ciclo del carbono, el cual sufre cambios y es alterado (Walker et al. 2019). El carbono se encuentra almacenado tanto en la biomasa vegetal como en la materia orgánica del suelo, con distribuciones diferentes según la región del planeta. Por lo tanto, los incendios producen más emisiones en unas regiones que en otras. En particular, la materia orgánica del suelo produce grandes almacenes de carbono en las zonas boreales (Bond-Lamberty et al. 2007; Veraverbeke et al. 2021), produciendo una alta cantidad de emisiones cuando se producen incendios. CO2, CH4, N2O, entre otros gases, normalmente son emitidos por los incendios forestales y los suelos quemados (Köster et al. 2017); CO2 es el más común pero el CH4 ha sido el menos estudiado, aunque tiene un efecto importante.

Igualmente, según la región del mundo los incendios tienen un distinto origen, pudiendo ser naturales, debido a rayos (Kasischke et al. 2002), o antrópicos, debido a actividades humanas. Las regiones boreales recientemente están sufriendo un incremento de los rayos, los cuales han aumentado la cantidad de incendios (Veraverbeke et al. 2017), repercutiendo positivamente en el aumento de emisiones de carbono. Al contrario, las

regiones tropicales están más influenciadas por actividades humanas (Archibald et al. 2009) donde las tendencias reflejan un descenso de los incendios en los últimos años (Andela et al. 2017), como consecuencia de las transformaciones en el uso del suelo y en los patrones de precipitación. La relación entre incendios y seres humanos es muy importante en estas regiones tropicales y en las regiones templadas, llegando a tener influencia en el tamaño de los incendios (Hantson et al. 2015).

El estudio de las series temporales de área quemada y sus tendencias (Andela et al. 2017), da la idea de las emisiones producidas y el carbono que ha podido ser emitido a la atmosfera (Ramo et al. 2021). Las series actuales muestran una disminución de las tendencias, aunque son series temporales cortas. En consecuencia, la creación de una serie temporal larga, resulta clave para una mejor comprensión y análisis del efecto que están ocasionando los incendios sobre nuestro planeta.

La emisión de carbono a la atmosfera provoca un incremento en el calentamiento climático, el cual produce un incremento de los factores naturales adversos, un mayor secado de la vegetación, unos ecosistemas más vulnerables, además de perdida de especies y sucesión de plantas remplazadas por vegetación más combustible (Chen et al. 2021). Las citadas consecuencias están profundamente ligadas con el riesgo de incendios a la vez que una mayor frecuencia y severidad de los mismos (de Groot et al. 2013), más perdida de carbón en la vegetación y el suelo, y un aumento de las emisiones (Bond-Lamberty et al. 2007; Pellegrini et al. 2018). Por lo tanto, esto se convierte en un círculo de retroalimentación positiva (Li et al. 2017) donde el cambio climático va hacia su peor escenario.

Estas razones explican que los incendios forestales sean considerados por el *Global Climate Observing System* (GCOS) como una variable esencial del clima (GCOS 2011) y ha sido incluida en el informe de evaluación del *Intergovernmental Panel on Climate Change (*IPCC, IPCC 2021).

Para responder a los requerimientos del GCOS y al gran interés en el análisis del clima, la ESA creó en 2010 el programa CCI, el cual incluyo inicialmente 10 variables, aumentándolas recientemente hasta 25 (https://climate.esa.int/en/, último acceso noviembre 2021). Como variables de importancia incluidas en el programa CCI, encontramos: incendios, biomasa, nubes, glaciares, cobertura terrestre, lagos, nivel del mar, nieve, etc.; las cuales tienen un efecto esencial en los procesos globales y del clima. En concreto, la variable de incendios fue parte de programa inicial y por lo tanto lleva activa más de 10 años. El objetivo de esta variable y del proyecto FireCCI es el desarrollo de series temporales de área quemada globales mediante teledetección.

1.2. Modelos climáticos

Acorde con el propósito del programa CCI, se pretende mejorar los actuales modelos climáticos, facilitando a los modeladores series de datos sobre variables climáticas esenciales, que les permitan parametrizarlos mejor. Las variables esenciales del clima son indicadores físicos, químicos o biológicos, clave, que caracterizan el clima de la Tierra. Mediante un mayor conocimiento global del clima, sus interacciones y su evolución, mejoramos nuestra comprensión del cambio climático. En la actualidad el GCOS detalla 54 variables esenciales, las cuales son requeridas para apoyar al trabajo de *United Nations Framework Convention on Climate Change* (UNFCCC) y del IPCC.

La variable Incendios se ha convertido en necesaria en la mayoría de modelos climáticos existentes (Hantson et al. 2016), ya que sus emisiones generan uno de los impactos globales más significativos sobre el clima. En el caso de los incendios forestales, la fecha, el tamaño, la intensidad y la distribución espacial de los incendios son variables críticas para una mejor comprensión del rol del fuego en los modelos de emisiones atmosféricas y de carbono (Hantson et al. 2016). Por lo tanto, datos precisos y actualizados de área quemada se han vuelto ampliamente reconocidos como un parámetro relevante para los modelos de carbono y del clima, y así conocer como estos gases afectan y alteran a las dinámicas del clima, la atmosfera y su composición.

En el inicio de los modelos climáticos, los incendios forestales no eran incluidos. Aunque se tenía en cuenta una aproximación basada en un tratamiento genérico, una variable acerca de la mortalidad de las plantas debido a una perturbación (Hantson et al. 2016), o se calculaba los regímenes de incendio utilizando un índice empírico de humedad más la biomasa combustible (Thonicke et al. 2001).

Esta información de los incendios ha sido estudiada por la teledetección y se ha calculado como área quemada (Chuvieco et al. 2019). Lamentablemente, se encuentra disponible en series de tiempo cortas o regionales, pero presenta un vacío global en una serie temporal larga, lo que se ha convertido en un requerimiento del GCOS (GCOS 2016).

Antes de tener información a escala global de los incendios mediante teledetección, su obtención era un reto. Una opción era calcular el área quemada (Liu 1994) mediante la información de *Food and Agriculture Organization* (FAO) de aquellos países que facilitaban los datos. Otra opción era recurrir a los departamentos responsables de los incendios forestales de cada país, y trabajar con la información que almacenasen (FAO 2001; GFMC 2021). También se utilizaron datos presentes en la literatura, datos de campo, estudios científicos, y como en ocasiones los datos disponibles eran regionales

y se encontraban zonas sin datos, se optaba por la interpolación a esos lugares (Mouillot and Field 2005). Otras fuentes utilizadas para obtener información sobre regímenes de incendios pasados fueron los registros de carbón en los sedimentos de los lagos, que dan idea de los cambios locales producidos (Power et al. 2010), y estimaciones empíricas del intervalo de retorno de emisiones de los incendios en diferentes biomas (Mouillot et al. 2014).

En los últimos años, desde que hay datos globales mediante imágenes de satélite se han generado productos de área quemada y fuegos activos (Giglio et al. 2018; Giglio et al. 2016; Lizundia-Loiola et al. 2020), basados en los sensores de observación global existentes (Chuvieco et al. 2019). Todos estos productos globales tienen unas cortas series de tiempo, lo cual reduce la relevancia de estos conjuntos de datos para analizar tendencias entre el clima y la actividad de los incendios. A pesar de esto, su introducción ha supuesto una aportación a la comprensión de los patrones globales sobre todo en las dos últimas décadas (Krawchuk and Moritz 2014).

Esta información ha dado lugar a varios inventarios donde los datos han sido recogidos. El inventario *Reanalysis of the Tropospheric chemical composition over the past 40 years project* (RETRO, Schultz et al. 2005) recoge información de emisión de biomas quemados desde 1960 al 2000, basado en varias fuentes, como: una revisión de la literatura disponible, datos de los servicios forestales, estimaciones de varios productos de satélite y un modelo numérico. Este inventario se utilizó como base junto al producto de emisiones *Global Fire Emissions Database* (GFED, Van Der Werf et al. 2017), para crear otros inventarios como el *Atmospheric Chemistry and Climate Model Intercomparison Project* (ACCMIP, Lamarque et al. 2010) que recoge datos de 1850 al 2000. El inventario de Kloster et al. (2010) se basó en la simulación de un modelo para obtener información de incendios del siglo XX. El inventario GICC *biomass burning* (Mieville et al. 2010) obtuvo información de 1900 a 2005 de una reconstrucción histórica de la superficie quemada (Mouillot and Field 2005), de datos del producto de área quemada GBA2000 y de puntos de calor ATSR (*Along Track Scanning Radiometers*). Por último, una mayor serie temporal de emisiones históricas (1750-2015) globales de biomasa quemada son ofrecidas por CMIP6 (BB4CMIP, Van Marle et al. 2017), mediante datos de satélite, medidas y estimaciones de emisiones, y la media de seis modelos del protocolo *Fire Model Intercomparison Project* (FireMIP).

En estos inventarios se encuentran grandes diferencias de biomas quemados por la diferencia de estimación de áreas quemadas en los distintos productos disponibles (Granier et al. 2011), lo que evidencia que hay que hacer un esfuerzo por una mayor precisión y coherencia de los datos.

La mayoría de modeladores del clima enfatizan en la necesidad de extender las series de tiempo existentes de área quemada hacia atrás en el tiempo. En su mayoría precisan de series temporales globales largas, de al menos las últimas tres décadas, para una mejor comprensión de incendios a largo plazo, del clima, de la interacción con la vegetación y de su efecto en la atmosfera (Granier et al. 2011; Le Page et al. 2007; Mouillot et al. 2014). Seria idóneo que esta información pertenezca a un solo producto para una buena estabilidad y consistencia (Mouillot et al. 2014).

1.3. Cartografía de Área Quemada a nivel global

Las estimaciones de emisiones son necesarias en los modelos climáticos, y su efecto en los ciclos de carbono y el clima. Para calcular estas emisiones, la observación de la Tierra mediante imágenes de satélite ofrece una gran oportunidad para estimar las diferentes variables y mediciones necesarias, como el área quemada, la severidad o la cantidad de biomasa consumida. Esta información es crítica para evaluar los impactos al medio ambiente de los biomas quemados, al igual que para analizar las características de los regímenes de incendios y los cambios temporales.

1.3.1. Algoritmos

Los productos de área quemada están basados en tres enfoques de algoritmos: reflectividad, puntos de calor o *Hotspots* (HS), o un hibrido de estos dos enfoques anteriores.

Por un lado, los algoritmos basados en puntos de calor, tienen en cuenta las anomalías térmicas detectadas por el sensor. Estas anomalías se basan en que los incendios desprenden una mayor cantidad de calor o radianza térmica en un punto determinado. Los puntos de calor suelen ser detectados por los canales del infrarrojo medio ya que tienen una mayor sensibilidad para este propósito en esa longitud de onda (Li et al. 2001). Los productos de área quemada que utilizan únicamente los puntos de calor, asumen como área quemada la proporción de pixeles afectados y la temperatura recogida por el sensor (Giglio et al. 2005; Kaiser et al. 2012).

Por otro lado, los algoritmos basados en reflectividades, están más ligados a la parte temporal y a la detección de cambios. Estos algoritmos analizan imágenes pre y post entre las cuales ha sucedido la perturbación, y la diferencia resultante indica si ha habido un cambio (Bastarrika et al. 2014), siendo común la utilización del Infrarrojo cercano (NIR). También es habitual la utilización de índices espectrales que son más sensibles a los cambios y aumenten la señal de quemado. Los índices más comunes para la

detección de área quemada son el *Global Environment Monitoring Index* (GEMI, Pinty and Verstraete 1992), *Burned Area Index* (BAI, Chuvieco et al. 2002) y *Normalized Burn Ratio* (NBR, López García and Caselles 1991).

Por último, los algoritmos híbridos unen los dos enfoques anteriores, utilizando los puntos de calor para localizar las zonas de interés, y las reflectancias para detectar el área que ha sufrido el incendio (Giglio et al. 2018; Lizundia-Loiola et al. 2020).

Es común que estos algoritmos usen la selección de umbrales con el fin de detectar cambios. Esta metodología, suele aplicar umbrales de corte para obtener una mejor discriminación en la separación de clases (Fraser et al. 2004; Lizundia-Loiola et al. 2020; Moreno-Ruiz et al. 2013; Riaño et al. 2007b). La umbralización se ha utilizado para encontrar un mejor ajuste entre área quemada y áreas no quemadas (Bin et al. 2019; Brown et al. 2018; Vhengani et al. 2015), para obtener semillas de área quemada (Plank and Martinis 2018) o para generar puntos de calor (Giglio et al. 2016).

1.3.2. Productos globales de área quemada

Actualmente, los datos globales de área quemada están disponibles a partir de 1995, aunque no han sido consistentes hasta el año 2001 (Mouillot et al. 2014) con el sensor MODIS (Chuvieco et al. 2019). Antes de 1995 solo se disponía de datos de manera regional o continental, con el uso de los satélites NOAA y el sensor AVHRR (Li et al. 2000; Sukhinin et al. 2004). Para estos años pre-MODIS se hizo varios prototipos globales mediante un producto pre-procesado de AVHRR, *Pathfinder AVHRR Land* (PAL), degradado a 8km. Estos intentos fueron generados, por un lado, semanalmente por el *Global Burned Surface* (GBS, Carmona-Moreno et al. 2005) desde 1992 hasta 1999 y, por otro lado, mensualmente por Riaño et al. (2007a) desde 1981 a 2000, pero su calidad fue reducida y no fueron publicados.

En el año 1995 comenzó la obtención de datos del sensor ATSR-2 (1km), a principios de los 2000 los de SPOT-VEGETATION (1km) y en 2002 los *Advanced Along-Track Scanning Radiometer* (AATSR). Las primeras estimaciones de área quemada global fueron mensuales y producidas por GLOBSCAR (Simon et al. 2004) mediante ATSR-2 para el año 2000. GLOBCARBON (Plummer et al. 2005) mejoró el anterior algoritmo y fue basado en ATSR-2, SPOT-VEGETATION y AATSR desde 1998 hasta 2007, ofreciendo resultados mensuales. Los productos basados únicamente en SPOT-VEGETATION datan del año 2000 (GBA2000, mensual, Grégoire et al. 2003; Tansey et al. 2004) y fueron extendidos en los años posteriores, como el producto mensual L3JR hasta 2007 (Tansey et al. 2008) y el GEOLAND 2 hasta 2018 que entregó datos cada 10 días. Más recientemente, se

utilizaron las imágenes de Proba-V (333m y 1km) usando un algoritmo de área quemada similar a GEOLAND 2 para obtener el producto GIO-GL1 desde 2014 hasta nuestros días, con resultados cada 10 días (Tansey and Wolfs 2017).

Con la entrada de imágenes del sensor MODIS, la NASA comenzó la generación de productos de área quemada. Este sensor ofrece datos de resolución media en los cuales están basados los productos globales más precisos. En un primer momento, el primer producto lanzado fue el MCD45A1 (500m, 2001-2015, mensual, Roy et al. 2008, antiguo producto oficial de la NASA) aunque fue reemplazado y mejorado por el producto mensual MCD64A1 (500m, Giglio et al. 2018, producto oficial de la NASA), el cual cubre un periodo de tiempo de 20 años (desde 2001 hasta la actualidad). Basado en este producto y complementado con puntos de calor del sensor ATSR de la ESA, se desarrolló el producto degradado GFED (Versión 4, 0.25°, (Van Der Werf et al. 2017). Este producto dispone de información mensual de emisiones procedentes del área quemada desde 1995 hasta nuestros días.

En los últimos años, se han visto avances importantes en el desarrollo de productos de área quemada con la entrada de la ESA y el proyecto CCI. Tras el producto mensual FireCCI41 basado en el sensor *MEdium Resolution Imaging Spectrometer* (MERIS, 300m) desde 2005 a 2011 (Alonso-Canas and Chuvieco 2015), los siguientes fueron desarrollados mediante el uso de MODIS. El producto FireCCI50 (250m, 2001-2016, Chuvieco et al. 2018) y su mejora FireCCI51 (250m, 2001-2020, Lizundia-Loiola et al. 2020) aumentaron la resolución espacial al doble, en comparación con los productos de la NASA (250m y 500m, respectivamente). Ambos productos son mensuales y oficiales de la ESA.

Tanto FireCCI51 como MCD64A1 muestran una precisión similar, aunque FireCCI51 presenta una mayor sensibilidad, detectando parches quemados pequeños (Lizundia-Loiola et al. 2020; Moreno-Ruiz et al. 2020) e incendios boreales (Moreno-Ruiz et al. 2020). Además, FireCCI51 aumenta el número de pixeles quemados notablemente. FireCCI51 detecta globalmente un 10% más de área quemada que MCD64A1, e incrementa el área quemada en la mayoría de regiones continentales (10 de 14) del mundo. Significativamente, FireCCI51 detecta más área quemada (hasta un 75%) en regiones boreales y templadas de Europa y Asia. FireCCI51 también muestra una buena actuación en la región boreal americana (Moreno-Ruiz et al. 2020), siendo mejor que MCD64A1.

Recientemente, dentro del *Copernicus Climate Change Service* se han desarrollado dos productos mensuales basados en el satélite Sentinel 3 (300m) y puntos de calor MODIS. Estos productos son el CGLOPS-1 (2020-actualidad, Padilla 2021), y el C3SBA10 (2019-

actualidad, Lizundia-Loiola et al. 2021), el cual es una adaptación del algoritmo de FireCCI51.

A pesar del interés en los productos de series temporales cortas, varios autores han indicado la conveniencia de generar unas series temporales más largas para extender el análisis global de las relaciones de los incendios con el medio ambiente (GCOS 2016). Por ello es necesario obtener un producto de cobertura global que además de presentar datos de a partir del 2000, tenga en cuenta las dos décadas anteriores, de manera que esta información se encuentre concentrada en un único lugar y sea más sencillo su utilización (Granier et al. 2011; Mouillot et al. 2014). Por esta razón, iniciamos esta tesis doctoral, ya que entendíamos que la extensión temporal de los productos de área quemada existentes al legado de AVHRR (>1981) sería realmente apreciado por los investigadores envueltos en los modelos de incendios.

1.4. AVHRR

La aparición y uso de datos de baja resolución se remonta a la década de los setenta, cuando se mejoraron los sensores disponibles para la observación meteorológica, facilitando así su uso en otro tipo de aplicaciones. Estos sensores facilitaban una visión global (Loveland et al. 2000) con una frecuencia de adquisición alta (Sukhinin et al. 2004). Los datos globales disponibles más antiguos son aquellos adquirimos por el sensor AVHRR a bordo de los satélites NOAA, los cuales empezaron su misión en 1979. Este archivo histórico ofrece el periodo más largo de información global en la teledetección, más de cuarenta años, iniciándose en el año 1979, aunque la grabación digital se inició en 1981.

1.4.1. Características del sensor

Los primeros datos almacenados del sensor AVHRR fueron los *Global Area Coverage* (GAC, 4x4 km, 1981-2021), inicialmente adquiridos con el sensor AVHRR2, y posteriormente desde el año 2000, con el sensor AVHRR3. Estos datos GAC son la versión degrada de los datos originales *Local Area Coverage* (LAC, 1.1km aproximadamente en el nadir, https://www.avl.class.noaa.gov/release/data_available/avhrr/index.htm#top, último acceso en noviembre de 2021), los cuales no se empezaron a almacenar globalmente hasta 1992. Los datos GAC reducen la resolución de la imagen a bordo de los satélites en tiempo real (https://www.avl.class.noaa.gov/saa/products/search?datatype_family=AVHRR último acceso noviembre 2021, EUMESAT 2011). Se utilizan cuatro de cada cinco muestras a lo

largo de la línea de escaneo para calcular un valor medio, y solo se procesan los datos de cada tercera línea de escaneo. Como resultado, la resolución espacial de los datos GAC cerca del subpunto es ≈1 km por ≈4 km con un espacio de ≈2 km entre los pixeles a lo largo de la línea de escaneo (EUMESAT 2011; Robel et al. 2014).

Desafortunadamente, la calidad radiométrica y geométrica de las observaciones AVHRR es mucho menor que los sensores más recientes, lo que convierte su tratamiento en un reto. Además de las muchas limitaciones con las que hay que lidiar, como la baja resolución, imágenes de varios sensores, remuestreo de la resolución original, degradación del sensor (desviación orbital – variación en el paso ecuatorial del satélite, pérdida de calidad, ausencia de datos), perdida de imágenes, ruido, cambios en la longitud de onda de las bandas y errores de localización (Krasnopolsky and Breaker 1994; McGregor and Gorman 1994; Price 1991; Riaño et al. 2007b; Weber and Wunderle 2019).

La calibración original de AVHRR depara grandes retos e incertidumbres, y es diferente para los diferentes canales (EUMESAT 2011). Además de que el AVHRR3 tiene mayor consistencia radiométrica que AVHRR2 (Trishchenko et al. 2002). El sensor del visible y del infrarrojo cercano se calibraron antes del lanzamiento (Robel et al. 2014), pero la calibración es aplicada a los datos después de su adquisición con un decaimiento lineal (Holben et al. 1990), debido a que ellos no tienen una calibración efectiva a bordo del satélite. La incertidumbre en la calibración es estimada en un 5% (Robel et al. 2014). La temperatura es calibrada orbitalmente, pero el comportamiento entre la calibración de los diferentes satélites y sus efectos tienen un rango de variabilidad en su medición (hasta más de 0.5K, Mittaz et al. 2019; Trishchenko et al. 2002). También la degradación sistemática de la sensibilidad radiométrica fue observada (por debajo del 1% por año) lo que implica la reducción de la resolución radiométrica, y expande el límite superior de la temperatura medida. Las incertidumbres de medición de la calibración de AVHRR son estimadas en ±0.1 K (Trishchenko et al. 2002).

También, la corrección de la degradación del sensor es una cuestión problemática (Csiszar et al. 2003). Una de las consecuencias más importantes es la pérdida de calidad de la señal, la cual presenta un incremento de ruido que hace la detección de cambios más difícil (Trishchenko et al. 2002). Además, una segunda consecuencia es la perdida de datos, aumentando los problemas para obtener una buena señal en el pixel (Otón et al. 2019). La degradación del sensor se ve agravada por estos problemas, debido a que no puede ser medida precisamente y no tienen fácil solución.

Añadido a la degradación del sensor se presenta un problema adicional, la variación temporal en el paso del satélite por el ecuador (Csiszar et al. 2003; Ignatov et al. 2004;

Privette et al. 1995). Esta variación, medida por el ángulo solar (Weber and Wunderle 2019), produce cambios pronunciados a ángulos altos. Esto influye directamente en la pérdida de calidad de la imagen y tiene que ser corregido (Stengel et al. 2020) para una óptima utilización de los datos. Los errores causados por el ángulo solar pueden ser grandes (Los et al. 1994) y su corrección requiere de información que podría no estar disponible (Roy 1997) o ser difícil de evaluar (Privette et al. 1995). Pocos esfuerzos han sido hechos para corregir la variación de la señal en las variables climáticas geofísicas (Devasthale et al. 2012). Algunas correcciones han sido hechas a los canales del rojo y el NIR (Latifovic et al. 2012), a las temperaturas (Devasthale et al. 2012; Gutman 1999; Lieberherr and Wunderle 2018), a los índices espectrales como NDVI (Privette et al. 1995; Sellers et al. 1994) o se ha dado preferencia a eliminar los años significativamente afectados (Ji and Brown 2017). Pocos de estos estudios han sido a largo plazo (Lieberherr and Wunderle 2018) o globales (Stengel et al. 2020), y todavía no han sido ampliados a estudios de área quemada (Weber and Wunderle 2019).

A pesar de estas complicaciones, el uso de las series temporales de AVHRR es bastante atractivo desde un punto de vista climático, ya que facilitaría una extensión temporal significante de los productos de área quemada actuales. La mayoría de estas limitaciones han sido corregidas y han permitido la realización de multitud de estudios desde los años ochenta (Flannigan and Vonder Haar 1986) aunque la mayoría corresponden a análisis regionales (Chuvieco et al. 2008; Dubinin et al. 2010; Eva and Lambin 1998; Kucêra et al. 2005; Plank and Martinis 2018; Potter et al. 2005; Pu et al. 2007; Yates et al. 2009).

1.4.2. Productos generados de AVHRR

La amplia cantidad de datos AVHRR ha permitido la generación de diferentes productos globales para aprovechar dicha información, aunque han tenido que ser degradados. Los datos GAC han sido el origen para varios productos globales: *Pathfinder AVHRR Land* (PAL, 1981-2000, 0,1˚≈8km, James and Kalluri 1994), *Global Inventory Modeling and Mapping Studies* (GIMMS, 1981-2006, 0,1˚≈8km, Tucker et al. 2005) y *Land Long Term Data Record* (LTDR, 1981-to date, ≈5km, Pedelty et al. 2007). GIMMS ofrece compuestos quincenales del índice espectral NDVI, PAL dispone de datos diarios y compuestos de 10 días, y LTDR es diario con la resolución espacial más alta y la mayor serie temporal de todos ellos.

Incluso siendo datos globales, estas versiones degradadas de AVHRR han sido usadas para detectar áreas quemadas en estudios regionales, como en: África (Barbosa et al. 1999; Riaño et al. 2007b), zonas boreales (Bunn and Goetz 2006) Alaska (Moreno-Ruiz

et al. 2019), Canadá (Alcaraz-Segura et al. 2010; Goetz et al. 2006; Moreno-Ruiz et al. 2012), Siberia (García-Lázaro et al. 2018); o para analizar las tendencias espaciales y temporal de ellas en una cobertura global (Riaño et al. 2007a). Los estudios globales han presentado series temporales cortas (menores a 20 años, Carmona-Moreno et al. 2005; Riaño et al. 2007a). Por lo tanto, no se han encontrado estudios globales con series temporales largas. Estos estudios mencionados han ofrecido valores de precisión moderados, comparados con otros productos de área quemada, debido a las limitaciones espaciales y radiométricas de los sensores AVHRR.

En concreto, LTDR ofrece unas mayores ventajas para estudiar las dinámicas del fuego que los otros productos generados con AVHRR, tales como mayor resolución temporal y espacial, e información diaria. En este sentido, LTDR ha sido usado en estudios regionales de área quemada, demostrando su potencial (Moreno-Ruiz et al. 2012; García-Lázaro et al. 2018).

1.4.3. Prototipos globales de área quemada con AVHRR

Debido al potencial de los productos basados en AVHRR, los cuales recogen en una base de datos toda la información, se crearon dos prototipos globales de área quemada. Ambos conjuntos de datos se basaron en el producto PAL (imágenes diarias a 1°≈8km) y cubrieron la etapa anterior al 2001.

El primer prototipo fue el GBS, (1992-1999, Carmona-Moreno et al. 2005), basado en compuestos semanales de mínimo albedo y los canales del rojo, NIR e infrarrojo medio, para crear los índices espectrales GEMI y Vi3t. El algoritmo se basó en la detección de cambios mediante el uso de umbrales absolutos y relativos de estos índices espectrales. El segundo prototipo (1981-2000, Riaño et al. 2007a) se basó en un estudio regional anterior (1981-1999, Riaño et al. 2007b) para África y en el algoritmo de Moreno-Ruiz et al. (1999). En este enfoque se utilizaron compuestos mensuales, información contextual, umbrales y las bandas del rojo y el NIR para crear el índice espectral *Normalized Difference Vegetation Index* (NDVI).

1.4.4. Land Long Term Data Record

El producto LTDR es un conjunto de datos a largo plazo (40 años) creados por la NASA. Este producto está basado en datos GAC del NOAA-AVHRR (4x4 km). Los datos fueron adquiridos por los sensores AVHRR2/3 a bordo de los satélites NOAA-7, 9, 11, 14, 16, 18 y 19 (todos ellos tienen el paso por el ecuador alrededor de las 3pm), en orbitas ascendentes del satélite. Este producto ofrece datos diarios y globales de reflectividad

de la superficie y NDVI con una resolución especial de 0.05 grados (≈ 5 km). Estos datos están disponibles desde principios de los 80's hasta la actualidad lo cual significa cuatro décadas de información (1981-actualidad, 40 años). La disponibilidad de datos en la serie temporal presenta algunos huecos temporales, siendo el de 1994 (desde marzo a diciembre) el más representativo.

El proyecto LTDR dispone de tres productos: AVH02 TOA *Surface Reflectance Product*, AVH09 *Surface Reflectance Product* and AVH13 NDVI *Product*. En este caso, AVH09 es un producto pre-procesado, ofreciendo reflectividad en superficie y dispone de 10 canales. Los canales de reflectividad: Canal 1 (rojo, 0.58-0.68 μm), Canal 2 (infrarrojo cercano o NIR, 0.725-1.1 μm) y Canal 3 (infrarrojo medio, 3.55-3.93 μm); canales térmicos: repetido para el Canal 3 (infrarrojo medio, 3.55-3.93 μm), Canal 4 (10.5-11.3 μm) y Canal 5 (11.5-12.5 μm); y el ángulo cenital visual, ángulo cenital solar, azimut relativo y calidad (QA).

La versión 4 de este producto era la versión disponible al comienzo de la tesis. Esta versión presentaba diversos problemas (Otón and Chuvieco 2018). El principal problema fue la falta de datos en la serie temporal, especialmente en 1994 y 2000, con muchos otros breves periodos de ausencia de datos. Otro problema estuvo relacionado con la ausencia de consistencia temporal en la serie de tiempo, particularmente en la calibración del infrarrojo cercano (canal 2) y el Rojo (canal 1). Esta discontinuidad era evidente en los cambios de satélites de la serie temporal, y en especial, en el cambio de satélite y sensor del año 2000. En este último caso, se produce una reducción de valores del NIR, la cual podría ser causada por una ausencia de una calibración apropiada entre las versiones 2 y 3 del sensor AVHRR (P. Lewis, comunicación personal, 2017). Este problema no fue observado en los canales 4 y 5 de temperatura.

Posteriormente, una nueva versión (versión 5) fue liberada por la NASA, la cual aparentemente solucionó los dos principales problemas observados de la versión anterior. La falta de datos fue reducida, encontrando solo el vacío de datos de 1994 y una degradación significativa de los mismos a partir del año 2019, con algunos cortos periodos de ausencia de datos. 1994 presenta importantes huecos y ruido en las imágenes desde marzo y datos vacíos desde septiembre, debido a la degradación del satélite N11 (Otón et al. 2019; Riaño et al. 2007b; Tucker et al. 2005) y la ausencia del N13 (falló, Carmona-Moreno et al. 2005) sustituido por el N14 (Ignatov et al. 2004). Desde 2018 en adelante la calidad de los datos del satélite N19 han sido degradados notablemente, con importantes huecos y ruido en las imágenes, lo que hace a los datos inservibles para obtener resultados aceptables (https://www.usgs.gov/centers/eros/science/usgs-eros-archive-advanced-very-high-resolution-radiometer-avhrr?qt-science_center_objects=0#qt-science_center_objects,

último acceso en noviembre de 2021). Consecuentemente, datos con problemas como los anteriormente comentados no han sido utilizados en otros estudios (Hansen et al. 2018; Tian et al. 2015). Los problemas de inter-calibración con el Rojo y el NIR también han sido en gran medida solucionados, donde la continuidad entre las adquisiciones del AVHRR2 y AVHRR3 está muy mejorada.

LTDR (versión 5) tiene un pre-procesado de la NASA, donde varias correcciones y calibraciones han sido aplicadas basadas en el programa *Pathfinder* (El Saleous et al. 2000). Entre las correcciones encontramos: las radiométricas (calibración vicaria en vuelo para los canales del visible y el infrarrojo cercano), geométricas (navegación inversa para relacionar una ubicación en la Tierra con cada sensor *Instantaneous Field Of View* [IFOV]), atmosféricas (corrección para *Rayleigh scattering*, ozono, vapor de agua y aerosoles, tales como las correcciones en las erupciones del Pinatubo y el Chinchon (El Saleous et al. 2000; Vermote et al. 2009)), y correcciones *Bidirectional Reflectance Distribution Function* (BRDF) por MODIS (Villaescusa-Nadal et al. 2019b). Además, la serie de datos LTDR tiene en cuenta varias calibraciones, lo cual es una cuestión critica cuando se utilizan varios sensores en el mismo producto y varias décadas (Mittaz et al. 2019). El canal del visible y el infrarrojo cercano fueron empíricamente calibrados debido a la ausencia de calibración a bordo del satélite (El Saleous et al. 2000). También, se realizó una calibración multi-sensor, ajustando espectralmente los diferentes sensores, con el N14 como referencia (Villaescusa-Nadal et al. 2019a).

1.4.4.1. Limitaciones

A pesar de estas correcciones y calibraciones entre sensores, el producto presenta diversas inconsistencias (Beck et al. 2011; Otón et al. 2019).

En primer lugar, la reconfiguración del ancho de banda del infrarrojo medio (Canal 3) durante la introducción del nuevo sensor AVHRR3 a bordo del NOAA-16. Esta reconfiguración del canal 3, creó el canal 3a (1.6 µm) para la obtención de datos durante el día y delegó al canal original 3b (3.75 µm) a recoger datos nocturnos. Esta alteración produjo variaciones espectrales de la serie temporal en el periodo 2000-2003 (Beck et al. 2011; Pedelty et al. 2007; Trishchenko et al. 2002). En 2003 la configuración histórica fue restaurada. Además, el canal 3 mostró diferentes puntos de saturación en los canales térmicos entre sensores. El sensor AVHRR2 se saturaba a los 323,75K (50°C) y el AVHRR3 a los 336,15K (63°C) (Otón et al. 2019; Trishchenko et al. 2002). Estos problemas hacen del canal 3 inconsistente para su uso (Otón et al. 2019).

En segundo lugar, los sensores se fueron degradando a lo largo de sus años de vida e implicó variaciones significativas en su órbita, influyendo en la reflectividad. La degradación de los sensores implica amplias variaciones en la sincronización con el Sol (Csiszar et al. 2003; McGregor and Gorman 1994; Price 1991; Riaño et al. 2007b; Weber and Wunderle 2019), lo cual se debe a que carecen de un sistema de ajuste de la órbita para compensar la variación de la resistencia atmosférica (Price 1991). Esto produce un retraso en el cruce del ecuador (Privette et al. 1995), provocando variaciones de la iluminación (Csiszar et al. 2003; McGregor and Gorman 1994; Privette et al. 1995; Riaño et al. 2007b; Weber and Wunderle 2019), diferente ciclo diurno (Ignatov et al. 2004), falsas tendencias, cambios en las temperaturas de fondo (medidas de temperaturas de reflectancia y brillo, Weber and Wunderle 2019), modificaciones en las propiedades de la señal (Tian et al. 2015), y mala calidad de los datos (Otón et al. 2019). Estas variaciones y problemas aumentan según el ángulo solar es mayor (Stengel et al. 2020). La degradación del sensor es de aproximadamente ≈5-10% en la precisión relativa de los canales visibles (Los et al. 1994).

En tercer lugar, el canal QA presenta un interesante enfoque teórico pero el resultado es deficiente ya que no es preciso. La capa fue usada para identificar y descartar aquellos pixeles que contenían nubes en la imagen (Bit number 1, yes=1), pero además de identificar aquellos con nubes, el QA también seleccionaba muchos otros pixeles claros, demostrando ser inconsistente.

En cuarto lugar, las latitudes altas tienen huecos y baja calidad de las observaciones en invierno (Otón et al. 2019), debido a que los satélites cubren estas regiones en la noche (Giglio and Roy 2020).

Por lo tanto, basado en estos datos y siendo conscientes de las limitaciones, para obtener una cartografía de área quemada, el algoritmo necesitaba tener en cuenta todos estos problemas. Los datos mencionados son bastante diferentes a aquellos previamente usados en los productos de área quemada globales. Principalmente, dos dificultades surgen al diseño del algoritmo:

1. No hay puntos de calor globales disponibles para la serie temporal, pudiéndose solo encontrar HS regionales (Li et al. 2000; Sukhinin et al. 2004). Esto es debido a la rápida saturación de los canales térmicos del AVHRR y las inconsistencias que presentan. Por lo tanto, los algoritmos híbridos usados en MERIS (FireCCI41), MODIS (MCD64A1 y FireCCI51) y Sentinel-2 (FireCCISFD11 y FireCCISFD20) no pueden ser adaptados a este conjunto de datos.
2. El tamaño del pixel es considerablemente grande (5x5 km, versus 20x20m de Sentinel-2, 250x250m de MODIS o 300x300m de MERIS), y por lo tanto son

esperadas confusiones mucho más grandes con otras coberturas espectrales similares al área quemada.

A pesar de sus limitaciones y sus potenciales mejoras, el producto LTDR es una base de datos útil e importante. Estos datos han sido usados en diferentes estudios como *Vegetation Continuous Fields* (Hansen et al. 2018), fenología de superficie (Zhang et al. 2014) y detección de área quemada (García-Lázaro et al. 2018; Moreno-Ruiz et al. 2019).

1.4.4.2. Productos de área quemada basados en LTDR

Los productos de área quemada que se han desarrollado hasta el momento con datos LTDR, son todos regionales, especialmente restringidos a las zonas boreales. El equipo desarrollador de estos productos es el dirigido por Moreno-Ruiz. Estos productos se basan en un mismo algoritmo, el cual han ido mejorando y actualizando acorde a los datos disponibles. Los datos de entrada comunes son el LTDR, compuestos cada 10 días mediante máxima temperatura del T3, los canales del rojo, NIR y T3, y los índices espectrales *Burned Boreal Forest Index* (BBFI) y GEMI. El algoritmo desarrollado combina tres pasos: umbrales relativos y absolutos de antes y después de los incendios, un clasificador bayesiano, y un análisis contextual.

El primer producto (Moreno-Ruiz et al. 2012) fue creado para Canadá y se extiende desde 1984 hasta 1999. Se utilizó la versión 3 del LTDR, los umbrales del algoritmo estaban basados en 7 parámetros y el clasificador se entrenó con perímetros oficiales de Canadá.

El segundo producto (Moreno-Ruiz et al. 2013) abarcó la zona boreal de América desde 1984 hasta 1998. Los datos de entrada fueron el LTDR versión 3, como en el producto anterior. El algoritmo sufrió una importante mejoría en su primer paso, al aumentar hasta 12 los parámetros de decisión de los umbrales. En esta ocasión, el clasificador fue entrenado con perímetros oficiales de la zona de estudio (Canadá y Alaska).

El tercer producto (Moreno Ruiz et al. 2014) también cubre la zona boreal americana, pero desde el año 2001 hasta el 2011. Su algoritmo está basado en el producto anterior, aunque introduce un importante cambio en la T3. En vez de utilizar el canal aportado por la versión 3 del LTDR, lo sustituye por el Infrarrojo de MODIS (banda 31, T31, 11.03 µm).

El cuarto producto (García-Lázaro et al. 2018), se realizó para Siberia entre los años 1982-2015. El algoritmo y los datos de entrada son iguales al anterior producto, aunque

introduce además los datos del LTDR versión 4. El algoritmo usa los datos MODIS y la versión 3 del LTDR para los años 2000–2008, y la versión 4 de LTDR para los años restantes. Los datos de entrenamiento son una muestra basada en Landsat.

Por último, el quinto producto (Moreno-Ruiz et al. 2019) fue generado para Alaska en los años 1982-2015. El algoritmo y los datos de entrada fueron idénticos a los del producto anterior, entrenando con perímetros oficiales del área de estudio.

1.5. Visión general de la tesis

1.5.1. Hipótesis

Los datos AVHRR bajo el producto LTDR cubren la serie temporal más larga entre los actuales sistemas de observación de la tierra (1981-actualidad), lo que mejora las estimaciones actuales sobre las tendencias de los incendios a escala global. Además, la consistencia temporal se ve mejorada por el entrenamiento con datos MODIS, que enlaza las estimaciones históricas con las actuales.

Debido al uso de un producto único que engloba las observaciones de los 40 años, se duplica los datos de área quemada actuales, y se proporciona una mayor consistencia y coherencia en las estimaciones. La estabilidad producida permite una mejor comprensión de los regímenes de incendios, y un sustancial aporte al estudio de las emisiones y el cambio climático.

1.5.2. Objetivos

El objetivo principal del estudio es desarrollar un producto global de área quemada coherente y consistente, con la serie temporal de datos más larga del momento (1982-2018), produciendo alrededor de 20 años de incremento en los datos históricos hasta ahora disponibles. Su fiabilidad debe ser evaluada y analizada para conocer su comportamiento.

Para cumplir con este objetivo principal de la tesis, es necesario completar un conjunto de objetivos específicos, como:

- Revisión bibliográfica de los distintos productos y algoritmos de área quemada existentes. Estudio de los datos necesarios para poder desarrollar el algoritmo y análisis de los factores involucrados en los incendios.

- Obtención de la información y creación de una base de datos para su utilización en el algoritmo. Análisis y generación de variables derivadas de los datos. Preparación y pre-proceso de la base de datos para su introducción en el algoritmo.
- Creación y entrenamiento de un algoritmo global de área quemada con la base de datos desarrollada anteriormente. Ajuste y evaluación de los parámetros del algoritmo. Obtención de los modelos resultantes del algoritmo para realizar la clasificación.
- Clasificación, análisis y procesado de la base de datos para la producción del producto final.
- Evaluación, comparación y validación del producto con otros productos de área quemada disponibles, perímetros oficiales, estudios regionales y datos independientes de referencia basados en Landsat.
- Análisis de tendencias temporales y espaciales de los resultados para conocer sus tendencias.

1.5.3. Publicaciones

La tesis es presentada por compendio de artículos, los cuales forman los capítulos 2–5 y están publicados en revistas o actas de congresos indexadas en JCR o Scopus. Los cuatro artículos pertenecen a publicaciones internacionales con evaluación por pares (*peer-reviewed*).

Tabla 1.1. Índice de artículos publicados en la tesis, capítulos a los que corresponden y factores de impacto.

		Factor de impacto	
Capítulo	**Publicación**	**SCOPUS**	**JCR**
2	**Otón, G.**, Ramo, R., Lizundia-Loiola, J., & Chuvieco, E. (2019). Global Detection of Long-Term (1982–2017) Burned Area with AVHRR-LTDR Data. *Remote Sensing*, 11(18), 2079.	6.6	4.848
3	**Otón, G.**, Lizundia-Loiola, J., Pettinari M.L. & Chuvieco, E. (2021). Development of a Consistent Global Long-Term Burned Area product (1982-2018) based on AVHRR-LTDR data. *International Journal of Applied Earth Observation and Geoinformation*, 103, 102473.	12.5	5.933

La tabla continua en la siguiente página

Tabla 1 – Continuación de la anterior página

Capítulo	Publicación	Factor de impacto	
		SCOPUS	JCR
4	**Otón, G.**, Franquesa, M., Lizundia-Loiola, J., & Chuvieco, E. (2021). Validation of low spatial resolution and no-dichotomy global long-term burned area product by Pareto boundary. In, *Earth Resources and Environmental Remote Sensing/GIS Applications XII* (pp. 293-299): SPIE	0.8	–
5	**Otón, G.**, Pereira, J.M., Silva, J.M.N. & Chuvieco, E. (2021). Analysis of trends in the FireCCI global long term burned area product (1982-2018). *Fire*, 4, 74.	3.7	–

1.5.4. Financiación

La tesis fue financiada por la Agencia Espacial Europea, dentro de su programa *Climate Change Initiative*, mediante los proyectos Fire_cci *Phase* 2 (número de contracto: 4000115006/15/INB) y Fire_cci+ (número de contracto: 4000126706/19/I-NB).

1.5.5. Conjuntos de datos publicados

En esta tesis se publicaron dos productos de área quemada para una serie temporal larga, en el proyecto Fire_CCI, basados en los datos LTDR:

- **Versión 1.1 (FireCCILT11):**
  https://climate.esa.int/en/projects/fire/data/
  https://geogra.uah.es/fire_cci/fireccilt11.php
  - **Pixel (0.05°):**
    https://catalogue.ceda.ac.uk/uuid/b1bd715112ca43ab948226d11d72b85e
    https://code.earthengine.google.com/?asset=users/g_oton/FireCCILT11
  - **Grid (0.25°):**
    https://catalogue.ceda.ac.uk/uuid/62866635ab074e07b93f17fbf87a2c1a
- **Versión 1.0 Beta (FireCCILT10) – Reemplazada.**
  https://climate.esa.int/en/projects/fire/data/
  - **Grid (0.25°):**
    https://catalogue.ceda.ac.uk/uuid/4f377defc2454db9b2a6d032abfd0cbd

1.5.6. Documentos técnicos

En el trascurso de la tesis, varios documentos técnicos fueron realizados para el proyecto que financiaba la investigación:

Otón, G. & Chuvieco, E. (2021) ESA CCI ECV Fire Disturbance: O2.D3 Algorithm Theoretical Basis Document (ATBD) for AVHRR-LTDR data, version 1.0. In review.

Pettinari M.L., Chuvieco E., Lizundia-Loiola J., **Otón G.** (2021) ESA CCI ECV Fire Disturbance: D1.2 Algorithm Development Plan, version 2.1. Available at: https://climate.esa.int/en/projects/fire/key-documents/

Otón, G. (2020) ESA CCI ECV Fire Disturbance: D4.2.2 Product User Guide – AVHRR-LTDR, version 1.0. Available at: https://climate.esa.int/en/projects/fire/key-documents/.

Lizundia-Loiola J., **Otón G.**, Belenguer-Plomer M.A., Tanase M.A., Pettinari M.L. & Chuvieco E. (2020). ESA CCI ECV Fire Disturbance: D2.2 End to End Uncertainty Budget, version 1.0. Available at: https://climate.esa.int/en/projects/fire/key-documents/.

Otón, G. & Pettinari, M.L. (2019) ESA CCI ECV Fire Disturbance: D3.3.4 Product User Guide - LTDR, version 1.0. https://climate.esa.int/en/projects/fire/key-documents/.

Storm, T., Pettinari, M.L., **Otón, G.**, & Lizundia-Loiola, J. (2019). ESA CCI ECV Fire Disturbance: D3.2. Software Verification Report, version 2.4. Available from: h https://climate.esa.int/en/projects/fire/key-documents/.

Otón, G., Chuvieco, E. (2018) ESA CCI ECV Fire Disturbance: O2.D2 Algorithm Theoretical Basis Document (ATBD) for AVHRR LTDR data, version 1.0. Available from: https://climate.esa.int/en/projects/fire/key-documents/.

Pettinari, M.L., **Otón, G.** & Chuvieco, E. (2017) ESA CCI ECV Fire Disturbance: O2.D1 User Requirement Document and Product Specification Document for AVHRR, version 1.1. Available from: https://climate.esa.int/en/projects/fire/key-documents/.

1.5.7. Congresos

Durante el desarrollo de la tesis, los avances y resultados han sido presentados en diferentes eventos:

SPIE Remote Sensing Digital Forum 2021, 13–17 de septiembre de 2021, online.

VIII Jornadas de Jóvenes Investigadores de la Universidad de Alcalá, 09–11 de diciembre de 2020, online.

III Simposio de Doctorandos de la UAH en Investigación con Tecnologías de la Información Geográfica (SITIG-UAH), 25–26 de noviembre de 2020, online.

XVIII Congreso de la Asociación Española de Teledetección, 25–27 de septiembre de 2019, Valladolid (España).

Living Planet Symposium, 13–17 de mayo en 2019, Milán (Italia).

VII Jornadas de Jóvenes Investigadores de la Universidad de Alcalá, 12–13 de diciembre de 2018, Alcalá de Henares (Madrid, España).

8th International Conference on Forest Fire Research, 10–16 de noviembre de 2018, Coimbra (Portugal).

XVIII Congreso Nacional de Tecnologías de la Información Geográfica de la Asociación de Geógrafos Españoles (AGE), 20–22 de junio de 2018, Valencia (España)

1er Simposio del Programa de Doctorado en Tecnologías de la Información Geográfica, 30 de octubre de 2017, Alcalá de Henares (Madrid, Spain).

II Taller de Doctorado en Geografía en el marco del XXV Congreso de la Asociación de Geógrafos Españoles, 24 de octubre, Madrid (España).

XVII Congreso de la Asociación Española de Teledetección, 3–7 de octubre de 2017, Murcia (España).

1.5.8. Estancias de investigación internacionales

En el trascurso de la tesis, el doctorando realizó dos estancias internacionales con equipos de gran trayectoria:

1. Lugar: Centro de investigación forestal; Departamento de recursos naturales, medioambiente y tierra; Escuela de agricultura de la Universidad de Lisboa, Lisboa, Portugal.
   Supervisor: Prof. José Miguel Pereira.
   Fechas: 05/2018 – 08/2018
2. Lugar: Laboratorio de Incendios; Departamento de recursos renovables en la Universidad de Alberta, Edmonton, Canadá.
   Supervisor: Prof. Mike Flannigan.
   Fechas: 06/2019 – 09/2019.

1.6. Referencias

Alcaraz-Segura, D., Chuvieco, E., Epstein, H.E., Kasischke, E.S., & Trishchenko, A. (2010). Debating the greening vs. browning of the North American boreal forest: differences between satellite datasets. Global Change Biology, 16, 760-770

Alonso-Canas, I., & Chuvieco, E. (2015). Global burned area mapping from ENVISAT-MERIS and MODIS active fire data. Remote Sensing Of Environment, 163, 140-152

Andela, N., Morton, D.C., Giglio, L., Chen, Y., van der Werf, G.R., Kasibhatla, P.S., DeFries, R.S., Collatz, G., Hantson, S., & Kloster, S. (2017). A human-driven decline in global burned area. Science, 356, 1356-1362

Archibald, S., Roy, D.P., Van Wilgen, B., & Scholes, R.J. (2009). What limits fire? An examination of drivers of burnt area in Southern Africa. Global Change Biology, 15, 613-630

Barbosa, P.M., Grégoire, J.M., & Pereira, J.M.C. (1999). An algorithm for extracting burned areas from time series of AVHRR GAC data applied at a continental scale. Remote Sensing Of Environment, 69, 253-263

Bastarrika, A., Alvarado, M., Artano, K., Martinez, M., Mesanza, A., Torre, L., Ramo, R., & Chuvieco, E. (2014). BAMS: A Tool for Supervised Burned Area Mapping Using Landsat Data. Remote Sensing, 6, 12360-12380

Beck, H.E., McVicar, T.R., van Dijk, A.I., Schellekens, J., de Jeu, R.A., & Bruijnzeel, L.A. (2011). Global evaluation of four AVHRR–NDVI data sets: Intercomparison and assessment against Landsat imagery. Remote Sensing Of Environment, 115, 2547-2563

Bin, W., Ming, L., Dan, J., Suju, L., Qiang, C., Chao, W., Yang, Z., Huan, Y., & Jun, Z. (2019). A Method of Automatically Extracting Forest Fire Burned Areas Using Gf-1 Remote Sensing Images. In, IGARSS 2019-2019 IEEE International Geoscience and Remote Sensing Symposium (pp. 9953-9955): IEEE

Bond-Lamberty, B., Peckham, S.D., Ahl, D.E., & Gower, S.T. (2007). Fire as the dominant driver of central Canadian boreal forest carbon balance. Nature, 450, 89-92

Bond, W.J., Woodward, F.I., & Midgley, G.F. (2005). The global distribution of ecosystems in a world without fire. New phytologist, 165, 525-538

Brown, A.R., Petropoulos, G.P., & Ferentinos, K.P. (2018). Appraisal of the Sentinel-1 & 2 use in a large-scale wildfire assessment: A case study from Portugal's fires of 2017. Applied Geography, 100, 78-89

Bunn, A.G., & Goetz, S.J. (2006). Trends in satellite-observed circumpolar photosynthetic activity from 1982 to 2003: The influence of seasonality, cover type, and vegetation density. Earth Interactions, 10, Paper n. 12: 11-19

Carmona-Moreno, C., Belward, A., Malingreau, J.P., Hartley, A., Garcia-Alegre, M., Antonovskiy, M., Buchshtaber, V., & Pivovarov, V. (2005). Characterizing interannual variations in global fire calendar using data from Earth observing satellites. Global Change Biology, 11, 1537-1555

Csiszar, I., Abuelgasim, A., Li, Z.Q., Jin, J.Z., Fraser, R., & Hao, W.M. (2003). Interannual changes of active fire detectability in North America from long-term records of the advanced very high resolution radiometer. Journal Of Geophysical Research-Atmospheres, 108, 4075, doi:4010.1029/2001JD001373,

Chen, Y., Morton, D.C., Andela, N., Giglio, L., & Randerson, J.T. (2016). How much global burned area can be forecast on seasonal time scales using sea surface temperatures? Environmental Research Letters, 11, 045001

Chen, Y., Romps, D.M., Seeley, J.T., Veraverbeke, S., Riley, W.J., Mekonnen, Z.A., & Randerson, J.T. (2021). Future increases in Arctic lightning and fire risk for permafrost carbon. Nature climate change, 11, 404-410

Chuvieco, E., Englefield, P., Trishchenko, A.P., & Luo, Y. (2008). Generation of long time series of burn area maps of the boreal forest from NOAA–AVHRR composite data. Remote Sens. Environ., 112, 2381-2396

Chuvieco, E., Lizundia-Loiola, J., Pettinari, M.L., Ramo, R., Padilla, M., Tansey, K., Mouillot, F., Laurent, P., Storm, T., & Heil, A. (2018). Generation and analysis of a new global burned area product based on MODIS 250 m reflectance bands and thermal anomalies. Earth System Science Data, 10, 2015-2031

Chuvieco, E., Martín, M.P., & Palacios, A. (2002). Assessment of different spectral indices in the red-near-infrared spectral domain for burned land discrimination. International Journal of Remote Sensing, 23, 5103-5110

Chuvieco, E., Mouillot, F., van der Werf, G.R., San Miguel, J., Tanasse, M., Koutsias, N., García, M., Yebra, M., Padilla, M., & Gitas, I. (2019). Historical background and current developments for mapping burned area from satellite Earth observation. Remote Sensing Of Environment, 225, 45-64

de Groot, W.J., Flannigan, M.D., & Cantin, A.S. (2013). Climate change impacts on future boreal fire regimes. Forest Ecology and Management, 294, 35-44

Devasthale, A., Karlsson, K.-G., Quaas, J., & Graßl, H. (2012). Correcting orbital drift signal in the time series of AVHRR derived convective cloud fraction using rotated empirical orthogonal function. Atmospheric Measurement Techniques, 5, 267-273

Dubinin, M., Potapov, P., Lushchekina, A., & Radeloff, V.C. (2010). Reconstructing long time series of burned areas in arid grasslands of southern Russia by satellite remote sensing. Remote Sensing Of Environment, 114, 1638-1648

El Saleous, N., Vermote, E., Justice, C., Townshend, J., Tucker, C., & Goward, S. (2000). Improvements in the global biospheric record from the Advanced Very High Resolution Radiometer (AVHRR). International Journal of Remote Sensing, 21, 1251-1277

EUMESAT (2011). AVHRR Level 1b Product Guide. In: EUM/OPS-EPS/MAN/04/0029 Issue: v3A Date: 21 Jan 2011. Available from: https://www.eumetsat.int/website/wcm/idc/idcplg?IdcService=GET_FILE&dDocName=PDF_AVHRR_L1B_PRODUCT_GUIDE&RevisionSelectionMethod=LatestReleased&Rendition=Web

Eva, H., & Lambin, E.F. (1998). Remote Sensing of Biomass Burning in Tropical Regions: Sampling Issues and Multisensor Approach. Remote Sensing Of Environment, 64, 292-315

FAO, G.F.F. (2001). Assessment 1990-2000. Forest Resources Assessment Working Paper—55, Rome

Flannigan, M.D., Amiro, B.D., Logan, K.A., Stocks, B., & Wotton, B. (2006). Forest fires and climate change in the 21st century. Mitigation and Adaptation Strategies for Global Change, 11, 847-859

Flannigan, M.D., & Vonder Haar, T.H. (1986). Forest fire monitoring using NOAA satellite AVHRR. Canadian Journal of Forest Research, 16, 975-982

Fraser, R.H., Hall, R.J., Landry, R., Lynham, T., Raymond, D., Lee, B., & Li, Z. (2004). Validation and calibration of Canada-wide coarse-resolution satellite burned-area maps. Photogrammetric Engineering and Remote Sensing, 70, 451-460

García-Lázaro, J., Moreno-Ruiz, J., Riaño, D., & Arbelo, M. (2018). Estimation of burned area in the Northeastern Siberian Boreal Forest from a long-term data record (LTDR) 1982–2015 time series. Remote Sensing, 10, 940

GCOS (2011). Systematic observation requirements for satellite-based products for climate, 2011 update. Geneva, Switzerland: World Meteorological Organization

GCOS (2016). The Global Observing System for Climate: Implementation Needs. Geneva, Switzerland: GCOS-200. World Meteorological Organization

GFMC (2021). Global Fire Monitoring Center. Available online: http://gfmc.online/, last accessed on October 2021.

Giglio, L., Boschetti, L., Roy, D.P., Humber, M.L., & Justice, C.O. (2018). The Collection 6 MODIS burned area mapping algorithm and product. Remote Sensing Of Environment, 217, 72-85

Giglio, L., & Roy, D. (2020). On the outstanding need for a long-term, multi-decadal, validated and quality assessed record of global burned area: Caution in the use of Advanced Very High Resolution Radiometer data. Science of Remote Sensing, 2, 100007

Giglio, L., Schroeder, W., & Justice, C.O. (2016). The collection 6 MODIS active fire detection algorithm and fire products. Remote Sensing Of Environment, 178, 31-41

Giglio, L., van der Werf, G.R., Randerson, J.T., Collatz, G.J., & Kasibhatla, P. (2005). Global estimation of burned area using MODIS active fire observations. Atmospheric Chemistry and Physics, 5, 11091-11141

Goetz, S., Fiske, G., & Bunn, A. (2006). Using satellite time-series data sets to analyze fire disturbance and forest recovery across Canada. Remote Sensing Of Environment, 92, 411-423

Granier, C., Bessagnet, B., Bond, T., D'Angiola, A., van Der Gon, H.D., Frost, G.J., Heil, A., Kaiser, J.W., Kinne, S., & Klimont, Z. (2011). Evolution of anthropogenic and biomass burning emissions of air pollutants at global and regional scales during the 1980–2010 period. Climatic Change, 109, 163-190

Grégoire, J.M., Tansey, K., & Silva, J.M.N. (2003). The GBA2000 initiative: Developing a global burned area database from SPOT-VEGETATION imagery. International Journal of Remote Sensing, 24, 1369 - 1376

Gutman, G. (1999). On the monitoring of land surface temperatures with the NOAA/AVHRR: removing the effect of satellite orbit drift. International Journal of Remote Sensing, 20, 3407-3413

Hansen, M., Song, X., DiMiceli, C., Carroll, M., Sohlberg, R., Kim, D.-H., & Townshend, J. (2018). MEaSURES Vegetation Continuous Fields ESDR: Algorithm Theoretical Basis Document (ATBD), Version 2.0. Available online: https://lpdaac.usgs.gov/documents/144/VCF5KYR_ATBD.pdf, last accessed on October 2021.

Hantson, S., Arneth, A., Harrison, S.P., Kelley, D.I., Prentice, I.C., Rabin, S.S., Archibald, S., Mouillot, F., Arnold, S.R., & Artaxo, P. (2016). The status and challenge of global fire modelling. Biogeosciences, 13, 3359-3375

Hantson, S., Pueyo, S., & Chuvieco, E. (2015). Global fire size distribution is driven by human impact and climate. Global Ecology and Biogeography, 24, 77-86

Holben, B.N., Kaufman, Y.J., & Kendall, J.D. (1990). NOAA-11 AVHRR visible and near-IR inflight calibration. International Journal of Remote Sensing, 11, 1511-1519

Ignatov, A., Laszlo, I., Harrod, E., Kidwell, K., & Goodrum, G. (2004). Equator crossing times for NOAA, ERS and EOS sun-synchronous satellites. International Journal of Remote Sensing, 25, 5255-5266

IPCC (2021). Climate Change 2021: The Physical Science Basis. Contribution of Working Group I to the Sixth Assessment Report of the Intergovernmental Panel on Climate Change. In V. Masson-Delmotte, P. Zhai, A. Pirani, S.L. Connors, C. Péan, S. Berger, N. Caud, Y. Chen, L. Goldfarb, M.I. Gomis, M. Huang, K. Leitzell, E. Lonnoy, J.B.R. Matthews, T.K. Maycock, T. Waterfield, O. Yelekçi, R. Yu, and B. Zhou (Ed.). Cambridge University Press. In Press.

James, M., & Kalluri, S.N. (1994). The Pathfinder AVHRR land data set: an improved coarse resolution data set for terrestrial monitoring. International Journal of Remote Sensing, 15, 3347-3363

Ji, L., & Brown, J.F. (2017). Effect of NOAA satellite orbital drift on AVHRR-derived phenological metrics. International Journal of Applied Earth Observation and Geoinformation, 62, 215-223

Kaiser, J., Heil, A., Andreae, M., Benedetti, A., Chubarova, N., Jones, L., Morcrette, J.-J., Razinger, M., Schultz, M., & Suttie, M. (2012). Biomass burning emissions estimated with a global fire assimilation system based on observed fire radiative power. Biogeosciences, 9, 527-554

Kasischke, E.S., Williams, D., & Barry, D. (2002). Analysis of the patterns of large fires in the boreal forest region of Alaska. International Journal of Wildland Fire, 11, 131-144

Kloster, S., Mahowald, N., Randerson, J., Thornton, P.E., Hoffman, F., Levis, S., Lawrence, P., Feddema, J., Oleson, K., & Lawrence, D. (2010). Fire dynamics during the 20th century simulated by the Community Land Model. Biogeosciences Discuss., 7, 1877-1902

Köster, E., Köster, K., Berninger, F., Aaltonen, H., Zhou, X., & Pumpanen, J. (2017). Carbon dioxide, methane and nitrous oxide fluxes from a fire chronosequence in subarctic boreal forests of Canada. Science of the Total Environment, 601, 895-905

Krasnopolsky, V.M., & Breaker, L.C. (1994). The problem of AVHRR image navigation revisited. International Journal of Remote Sensing, 15, 979-1008

Krawchuk, M., & Moritz, M. (2014). Burning issues: statistical analyses of global fire data to inform assessments of environmental change. Environmetrics, 25, 472-481

Kucêra, J., Yasuoka, Y., & Dye, D.G. (2005). Creating a forest fire database for the Far East of Asia using NOAA/AVHRR observation. International Journal of Remote Sensing, 26, 2423-2439

Lamarque, J.-F., Bond, T.C., Eyring, V., Granier, C., Heil, A., Klimont, Z., Lee, D., Liousse, C., Mieville, A., & Owen, B. (2010). Historical (1850–2000) gridded anthropogenic and biomass burning emissions of reactive gases and aerosols: methodology and application. Atmospheric Chemistry and Physics, 10, 7017-7039

Latifovic, R., Pouliot, D., & Dillabaugh, C. (2012). Identification and correction of systematic error in NOAA AVHRR long-term satellite data record. Remote Sensing Of Environment, 127, 84-97

Le Page, Y., Pereira, J., Trigo, R., Da Camara, C., Oom, D., & Mota, B. (2007). Global fire activity patterns (1996–2006) and climatic influence: an analysis using the World Fire Atlas. Atmospheric Chemistry and Physics Discussions, 7, 17299-17338

Li, F., Lawrence, D.M., & Bond-Lamberty, B. (2017). Impact of fire on global land surface air temperature and energy budget for the 20th century due to changes within ecosystems. Environmental Research Letters, 12, 044014

Li, Z., Kaufman, Y.J., Ichoku, C., Fraser, R., Trishchenko, A., Giglio, L., Jin, J., & Yu, X. (2001). A review of AVHRR-based active fire detection algorithms: Principles, limitations, and recommendations. Global and regional vegetation fire monitoring from space, planning and coordinated international effort, 199-225

Li, Z., Nadon, S., & Cihlar, J. (2000). Satellite-based detection of Canadian boreal forest fires: development and application of the algorithm. International Journal of Remote Sensing, 21, 3057-3069

Lieberherr, G., & Wunderle, S. (2018). Lake surface water temperature derived from 35 years of AVHRR sensor data for European lakes. Remote Sensing, 10, 990

Liu, M.-H. (1994). Spatial and temporal distribution of tropical biomass burning. Global Biogeochemical Cycles, 8, 495-503

Lizundia-Loiola, J., Franquesa, M., Boettcher, M., Kirches, G., Pettinari, M.L., & Chuvieco, E. (2021). Operational implementation of the burned area component of the Copernicus Climate Change Service: from MODIS 250 m to OLCI 300 m data. Earth System Science Data Discussions, 1-37

Lizundia-Loiola, J., Otón, G., Ramo, R., & Chuvieco, E. (2020). A spatio-temporal active-fire clustering approach for global burned area mapping at 250 m from MODIS data. Remote Sensing Of Environment, 236, 111493

López García, M.J., & Caselles, V. (1991). Mapping Burns and Natural Reforestation Using Thematic Mapper Data. Geocarto International, 1, 31-37

Los, S.O., Justice, C., & Tucker, C. (1994). A global 1 by 1 NDVI data set for climate studies derived from the GIMMS continental NDVI data. International Journal of Remote Sensing, 15, 3493-3518

Loveland, T.R., Reed, B.C., Brown, J.F., Ohlen, D.O., Zhu, J., Yang, L., & Merchant, J.W. (2000). Development of a global land cover characteristics database and IGBP DISCover from 1-km AVHRR data. International Journal of Remote Sensing, 21, 1303–1330

McGregor, J., & Gorman, A.J. (1994). Some considerations for using AVHRR data in climatological studies: orbital characteristics of NOAA satellites. International Journal of Remote Sensing, 15, 537-548

Mieville, A., Granier, C., Liousse, C., Guillaume, B., Mouillot, F., Lamarque, J.-F., Grégoire, J.-M., & Pétron, G. (2010). Emissions of gases and particles from biomass burning during the 20th century using satellite data and an historical reconstruction. Atmospheric Environment, 44, 1469-1477

Mittaz, J., Merchant, C.J., & Woolliams, E.R. (2019). Applying principles of metrology to historical Earth observations from satellites. Metrologia, 56, 032002

Moreno-Ruiz, J.A., Barbosa, P.M., Carmona-Moreno, C., Gregoire, J.M., & Belward, A. (1999). GLINT-BS. Global Burn Scar Detection System. Functional Description and User Manual Document. In: European Commission Technical Note I.99.167

Moreno-Ruiz, J.A., García-Lázaro, J.R., Arbelo, M., & Cantón-Garbín, M. (2020). MODIS Sensor Capability to Burned Area Mapping—Assessment of Performance and Improvements Provided by the Latest Standard Products in Boreal Regions. Sensors, 20, 5423

Moreno-Ruiz, J.A., García-Lázaro, J.R., Arbelo, M., & Riaño, D. (2019). A Comparison of Burned Area Time Series in the Alaskan Boreal Forests from Different Remote Sensing Products. Forests, 10, 363

Moreno-Ruiz, J.A., García-Lázaro, J.R., Riaño, D., & Kefauver, S.C. (2013). The Synergy of the 0.05º (5km) AVHRR Long-Term Data Record (LTDR) and Landsat TM Archive to Map Large Fires in the North American Boreal Region From 1984 to 1998. IEEE Journal of Selected Topics in Applied Earth Observations and Remote Sensing, 7, 1157-1166

Moreno-Ruiz, J.A., Riano, D., Arbelo, M., French, N.H., Ustin, S.L., & Whiting, M.L. (2012). Burned area mapping time series in Canada (1984–1999) from NOAA-AVHRR LTDR: A comparison with other remote sensing products and fire perimeters. Remote Sensing Of Environment, 117, 407-414

Moreno Ruiz, J.A.M., Lázaro, J.R.G., Cano, I.d.Á., & Leal, P.H. (2014). Burned area mapping in the North American boreal forest using Terra-MODIS LTDR (2001–2011): A comparison with the MCD45A1, MCD64A1 and BA GEOLAND-2 products. Remote Sensing, 6, 815-840

Mouillot, F., & Field, C.B. (2005). Fire history and the global carbon budget: a 1 degrees x 1 degrees fire history reconstruction for the 20th century. Global Change Biology, 11, 398-420

Mouillot, F., Schultz, M.G., Yue, C., Cadule, P., Tansey, K., Ciais, P., & Chuvieco, E. (2014). Ten years of global burned area products from spaceborne remote sensing—A review: Analysis of user needs and recommendations for future developments. International Journal of Applied Earth Observation and Geoinformation, 26, 64-79

Otón, G., & Chuvieco, E. (2018). ESA CCI ECV Fire Disturbance: O2.D2 Algorithm Theoretical Basis Document (ATBD) for AVHRR LTDR data, version 1.1. Available online: https://climate.esa.int/en/projects/fire/key-documents/, last accessed on October 2021.

Otón, G., Ramo, R., Lizundia-Loiola, J., & Chuvieco, E. (2019). Global Detection of Long-Term (1982–2017) Burned Area with AVHRR-LTDR Data. Remote Sensing, 11, 2079

Padilla, M. (2021). Copernicus Global Land Operations ”Vegetation and Energy”. Algorithm theorethical basis document: Burned area and seasonality, collection 300m. Version 3. Available online: https://land.copernicus.eu/global/sites/cgls.vito.be/files/products/CGLOPS1_ATBD_BA300m-V3_I1.10.pdf, last accessed on November 2021.

Pedelty, J., Devadiga, S., Masuoka, E., Brown, M., Pinzon, J., Tucker, C., Vermote, E., Prince, S., Nagol, J., Justice, C., Roy, D., Ju, J., Schaaf, C., Liu, J., Privette, J., & Pinheiro, A. (2007). Generating a long-term land data record from the AVHRR and MODIS instruments. In, Geoscience and Remote Sensing Symposium, 2007. IGARSS 2007. IEEE International (pp. 1021-1025): IEEE

Pellegrini, A.F., Ahlström, A., Hobbie, S.E., Reich, P.B., Nieradzik, L.P., Staver, A.C., Scharenbroch, B.C., Jumpponen, A., Anderegg, W.R., & Randerson, J.T. (2018). Fire frequency drives decadal changes in soil carbon and nitrogen and ecosystem productivity. Nature, 553, 194-198

Pinty, B., & Verstraete, M.M. (1992). GEMI: a non-linear index to monitor global vegetation from satellites. Vegetatio, 101, 15-20. https://doi.org/10.1007/bf00031911.

Plank, S., & Martinis, S. (2018). A Fully Automatic Burnt Area Mapping Processor Based on AVHRR Imagery—A TIMELINE Thematic Processor. Remote Sensing, 10, 341

Plummer, S., Arino, O., Ranera, F., Tansey, K., Chen, J., Dedieu, G., Eva, H., Piccolini, I., Leigh, R., & Borstlap, G. (2005). The GLOBCARBON initiative: multi-sensor estimation of global biophysical products for global terrestrial carbon studies. In, Envisat & ERS Symposium

Potter, C., Tan, P.N., Kumar, V., Kucharik, C., Klooster, S., Genovese, V., Cohen, W., & Healey, S. (2005). Recent History of Large-Scale Ecosystem Disturbances in North America Derived from the AVHRR Satellite Record. Ecosystems, 8, 808-824

Power, M.J., Marlon, J.R., Bartlein, P.J., & Harrison, S.P. (2010). Fire history and the Global Charcoal Database: A new tool for hypothesis testing and data exploration. Palaeogeography, Palaeoclimatology, Palaeoecology, 291, 52-59

Preisler, H.K., Burgan, R.E., Eidenshink, J.C., Klaver, J.M., & Klaver, R.W. (2009). Forecasting distributions of large federal-lands fires utilizing satellite and gridded weather information. International Journal of Wildland Fire, 18, 508-516

Price, J.C. (1991). Timing of NOAA afternoon passes. International Journal of Remote Sensing, 12, 193-198

Privette, J.L., Fowler, C., Wick, G.A., Baldwin, D., & Emery, W.J. (1995). Effects of orbital drift on Advanced Very High Resolution Radiometer products: Normalized Difference Vegetation Index and Sea Surface Temperature. Remote Sensing Of Environment, 53, 164-171

Pu, R.L., Li, Z.Q., Gong, P., Csiszar, I., Fraser, R., Hao , W.-M., Kondragunta, S., & Weng, F. (2007). Development and analysis of a 12-year daily 1-km forest fire North America from NOAA/AVHRR data. Remote Sensing Of Environment, 108, 198-208

Ramo, R., Roteta, E., Bistinas, I., Van Wees, D., Bastarrika, A., Chuvieco, E., & Van der Werf, G.R. (2021). African burned area and fire carbon emissions are strongly impacted by small fires undetected by coarse resolution satellite data. Proceedings of the National Academy of Sciences, 118, 1-7

Riaño, D., Ruiz, J.A.M., Isidoro, D., & Ustin, S.L. (2007a). Global spatial patterns and temporal trends of burned area between 1981 and 2000 using NOAA-NASA Pathfinder. Global Change Biology, 13, 40-50, doi: 10.1111/j.1365-2486.2006.01268.

Riaño, D., Ruiz, J.M., Martínez, J.B., & Ustin, S. (2007b). Burned area forecasting using past burned area records and Southern Oscillation Index for tropical Africa (1981–1999). Remote Sensing Of Environment, 107, 571-581

Robel, J., Graumann, A., Kidwell, K., Aleman, R., Ruff, I., Muckle, B., & Kleespies, T. (2014). NOAA KLM User's Guide with NOAA-N, N Prime, and MetOp Supplements. National Oceanic and Atmospheric Administration, Washington.–2530 p. Available from: https://www1.ncdc.noaa.gov/pub/data/satellite/publications/podguides/N-15%20thru%20N-19/pdf/0.0%20NOAA%20KLM%20Users%20Guide.pdf

Roy, D. (1997). Investigation of the maximum normalized difference vegetation index (NDVI) and the maximum surface temperature (Ts) AVHRR compositing procedures for the extraction of NDVI and Ts over forest. International Journal of Remote Sensing, 18, 2383-2401

Roy, D.P., Boschetti, L., & Justice, C.O. (2008). The collection 5 MODIS burned area product — Global evaluation by comparison with the MODIS active fire product. Remote Sensing Of Environment, 112, 3690-3707

Schultz, M., Heil, A., Hoelzemann, J., Spessa, A., Thonicke, K., Goldammer, J., Held, A., Pereira, J., & van het Bolscher, M. (2005). Global emissions from wildland fires from 1960 to 2000, submitted to Global Biogeochem. In: Cyc

Sellers, P.J., Tucker, C.J., Collatz, G.J., Los, S., Justice, C., Dazlich, D., & Randall, D. (1994). A global 1 by 1 NDVI data set for climate studies. Part 2: The generation of global fields of terrestrial biophysical parameters from the NDVI. International Journal of Remote Sensing, 15, 3519-3545

Simon, M., Plummer, S., Fierens, F., Hoelzemann, J.J., & Arino, O. (2004). Burnt area detection at global scale using ATSR-2: The GLOBSCAR products and their qualification. Journal of Geophysical Research - Atmospheres, 109, D14S02, doi:10.1029/2002JD003622

Stengel, M., Stapelberg, S., Sus, O., Finkensieper, S., Würzler, B., Philipp, D., Hollmann, R., Poulsen, C., Christensen, M., & McGarragh, G. (2020). Cloud_cci Advanced Very High Resolution Radiometer post meridiem (AVHRR-PM) dataset version 3: 35-year climatology of global cloud and radiation properties. Earth System Science Data, 12, 41-60

Sukhinin, A.I., French, N.H.F., Kasischke, E.S., Hewson, J.H., Soja, A.J., Csiszar, I.A., Hyer, E.J., Loboda, T., Conrad, S.G., Romasko, V.I., Pavlichenko, E.A., Miskiv, S.I., & Slinkina, O.A. (2004). AVHRR-based mapping of fires in Russia: New products for fire management and carbon cycle studies. Remote Sensing Of Environment, 93, 546-564

Tansey, K., Grégoire, J.M., Defourny, P., Leigh, R., Peckel, J.F., Bogaert, E.V., & Bartholome, J.E. (2008). A new, global, multi-annual (2000–2007) burnt area product at 1 km resolution. Geophysical Research Letters, 35, L01401, doi:10.1029/2007GL03156

Tansey, K., Grégoire, J.M., Stroppiana, D., Sousa, A., Silva, J., Pereira, J.M., Boschetti, L., Maggi, M., Brivio, P.A., Fraser, R., Flasse, S., Ershov, D., Binaghi, E., Graetz, D., & Peduzzi, P. (2004). Vegetation burning in the year 2000: Global burned area estimates from SPOT VEGETATION data. Journal of Geophysical Research - Atmospheres, 109, D14S03, doi:10.1029/2002JD003598, 2-22

Tansey, K., & Wolfs, D. (2017). Copernicus Global Land Operations ”Vegetation and Energy”. Algorithm theorethical basis document: Burned area and seasonality, collection 300m. Version 2. Available online: https://land.copernicus.eu/global/sites/cgls.vito.be/files/products/CGLOPS1_ATBD_BA300m-V1_I1.20.pdf, last accessed on November 2021.

Thonicke, K., Venevsky, S., Sitch, S., & Cramer, W. (2001). The role of fire disturbance for global vegetation dynamics: coupling fire into a Dynamic Global Vegetation Model. Global Ecology and Biogeography, 10, 661-677

Tian, F., Fensholt, R., Verbesselt, J., Grogan, K., Horion, S., & Wang, Y. (2015). Evaluating temporal consistency of long-term global NDVI datasets for trend analysis. Remote Sensing Of Environment, 163, 326-340

Trishchenko, A.P., Fedosejevs, G., Li, Z., & Cihlar, J. (2002). Trends and uncertainties in thermal calibration of AVHRR radiometers onboard NOAA-9 to NOAA-16. Journal of Geophysical Research: Atmospheres, 107, ACL 17-11-ACL 17-13

Tucker, C.J., Pinzon, J.E., Brown, M.E., Slayback, D.A., Pak, E.W., Mahoney, R., Vermote, E.F., & El Saleous, N. (2005). An extended AVHRR 8-km NDVI dataset compatible with MODIS and SPOT vegetation NDVI data. International Journal of Remote Sensing, 26, 4485-4498

Urbanski, S.P., Hao, W.M., & Baker, S. (2008). Chemical composition of wildland fire emissions. Developments in Environmental Science, 8, 79-107

Van Der Werf, G.R., Randerson, J.T., Giglio, L., Van Leeuwen, T.T., Chen, Y., Rogers, B.M., Mu, M., Van Marle, M.J., Morton, D.C., Collatz, G.J., Yokelson, R.J., & Kasibhatla, P.S. (2017). Global fire emissions estimates during 1997-2016. Earth Syst. Sci. Data,, 9, 697–720.

Van Marle, M.J., Kloster, S., Magi, B.I., Marlon, J.R., Daniau, A.-L., Field, R.D., Arneth, A., Forrest, M., Hantson, S., & Kehrwald, N.M. (2017). Historic global biomass burning emissions for CMIP6 (BB4CMIP) based on merging satellite observations with proxies and fire models (1750–2015). Geoscientific Model Development, 10, 3329-3357

Veraverbeke, S., Delcourt, C.J., Kukavskaya, E., Mack, M., Walker, X., Hessilt, T., Rogers, B., & Scholten, R.C. (2021). Direct and longer-term carbon emissions from arctic-boreal fires: a short review of recent advances. Current Opinion in Environmental Science & Health, 100277

Veraverbeke, S., Rogers, B.M., Goulden, M.L., Jandt, R.R., Miller, C.E., Wiggins, E.B., & Randerson, J.T. (2017). Lightning as a major driver of recent large fire years in North American boreal forests. Nature climate change, 7, 529-534

Vermote, E., Justice, C., Csiszar, I., Eidenshink, J., Myneni, R., Baret, F., Masuoka, E., Wolfe, R., & Devadiga, S. (2009). A Terrestrial Surface Climate Data Record for Global Change Studies [PowerPoint slides]. Retrieved from https://ltdr.modaps.eosdis.nasa.gov/ltdr/docs/AGU-Fall2009-vermote.pdf.

Vhengani, L., Frost, P., Lai, C., Booi, N., van den Dool, R., & Raath, W. (2015). Multitemporal burnt area mapping using Landsat 8: Merging multiple burnt area

indices to highlight burnt areas. In, 2015 IEEE International Geoscience and Remote Sensing Symposium (IGARSS) (pp. 4153-4156): IEEE

Villaescusa-Nadal, J.L., Franch, B., Roger, J.-C., Vermote, E.F., Skakun, S., & Justice, C. (2019a). Spectral adjustment model's analysis and application to remote sensing data. IEEE Journal of Selected Topics in Applied Earth Observations and Remote Sensing, 12, 961-972

Villaescusa-Nadal, J.L., Franch, B., Vermote, E.F., & Roger, J.-C. (2019b). Improving the AVHRR long term data record BRDF correction. Remote Sensing, 11, 502

Walker, X., Rogers, B., Veraverbeke, S., Johnstone, J., Baltzer, J., Barrett, K., Bourgeau-Chavez, L., Day, N., de Groot, W., & Dieleman, C. (2020). Fuel availability not fire weather controls boreal wildfire severity and carbon emissions. Nature climate change, 1-7

Walker, X.J., Baltzer, J.L., Cumming, S.G., Day, N.J., Ebert, C., Goetz, S., Johnstone, J.F., Potter, S., Rogers, B.M., & Schuur, E.A. (2019). Increasing wildfires threaten historic carbon sink of boreal forest soils. Nature, 572, 520-523

Ward, D., Kloster, S., Mahowald, N., Rogers, B., Randerson, J., & Hess, P. (2012). The changing radiative forcing of fires: global model estimates for past, present and future. Atmospheric Chemistry and Physics, 12.10857–10886.

Weber, H., & Wunderle, S. (2019). Drifting Effects of NOAA Satellites on Long-Term Active Fire Records of Europe. Remote Sensing, 11, 467

Yates, C.P., Edwards, A.C., & Russell-Smith, J. (2009). Big fires and their ecological impacts in Australian savannas: size and frequency matters. International Journal of Wildland Fire, 17, 768-781

Zhang, X., Tan, B., & Yu, Y. (2014). Interannual variations and trends in global land surface phenology derived from enhanced vegetation index during 1982–2010. International Journal of Biometeorology, 58, 547-564

Capítulo 2

GLOBAL DETECTION OF LONG-TERM (1982–2017) BURNED AREA WITH AVHRR-LTDR DATA

This article was published in the Remote Sensing Journal (11[18], 2079) in 2019.

Abstract

This paper presents the first global burned area (BA) product derived from the land long term data record (LTDR), a long-term 0.05-degree resolution dataset generated from advanced very high resolution radiometer (AVHRR) images. Daily images were combined in monthly composites using the maximum temperature criterion to enhance the burned signal and eliminate clouds and artifacts. A synthetic BA index was created to improve the detection of the BA signal. This index included red and near infrared reflectance, surface temperature, two spectral indices, and their temporal differences. Monthly models were generated using the random forest classifier, using the twelve monthly composites of each year as the predictors. Training data were obtained from the NASA MCD64A1 collection 6 product (500 m spatial resolution) for eight years of the overlapping period (2001–2017). This included some years with low and high fire occurrence. Results were tested with the remaining eight years. Pixels classified as burned were converted to burned proportions using the MCD64A1 product. The final product (named FireCCILT10) estimated BA in 0.05-degree cells for the 1982 to 2017 period (excluding 1994, due to input data gaps). This product is the longest global BA currently available, extending almost 20 years back from the existing NASA and ESA BA products. BA estimations from the FireCCILT10 product were compared with those from the MCD64A1 product for continental regions, obtaining high correlation values ($r2 > 0.9$), with better agreement in tropical regions rather than boreal regions. The annual average of BA of the time series was 3.12 Mkm2. Tropical Africa had the highest proportion of burnings, accounting for 74.37% of global BA. Spatial trends were found to be similar to existing global BA products, but temporal trends showed unstable annual variations, most likely linked to the changes in the AVHRR sensor and orbital decays of the NOAA satellites.

2.1. Introduction

The Global Climate Observing System (GCOS) program and the Intergovernmental Panel on Climate Change (IPCC) assessment report (Ciais et al. 2014) consider fire occurrence as one of the essential climate variables (ECV) because of its great impact on atmospheric emissions and vegetation dynamics (Bond et al. 2005; GCOS 2011; Granier et al. 2011; Urbanski et al. 2008; Ward et al. 2012). Climate modelers need information about the burned area (BA) to improve their knowledge on its role on climate dynamics. For this reason, most of the existing climate models include a fire module (Hantson et al. 2016).

Historical data on fires have been obtained through national fire statistics or from field studies (Mouillot and Field 2005; Power et al. 2010). These data have been used to generate global estimates of fire occurrence using different interpolation techniques (Mouillot and Field 2005). In the early 2000s, the first estimations of global BA derived from satellite earth observation were produced (Mouillot et al. 2014). Those products were derived from the SPOT-VEGETATION sensor at a 1 km resolution, first for the year 2000 (Grégoire et al. 2003) and then extended using similar BA algorithms for the period 2000–2007 (Tansey et al. 2008). More recently, similar approaches have been used to generate BA products from the Proba-V sensor, with 333 m resolution (Copernicus Programme 2019). NASA began generating BA products from images acquired by the MODIS sensor in the early 2000s. Two products were released from this sensor, MCD45A1 (Roy et al. 2008) and MCD64A1 (Giglio et al. 2018), both at a 500 m spatial resolution. The latter product was also the basis of the Global Fire Emission Database (GFED, now at v4, Van Der Werf et al. 2017). From the highest resolution bands of MODIS (at 250 m), a recent BA product has been released from the European Space Agency's Fire_cci project (Chuvieco et al. 2018).

All of these global products have a relatively short time series (2001 to the present), with the exception of the GFED, which extends to 1995, but contains higher uncertainties for the pre-MODIS era (<2000). This short period limits the relevance of these datasets for analyzing the relationships between climate and fire activity. For this reason, the use of advanced very high resolution radiometer (AVHRR) images is very appealing, as this sensor provides much longer temporal coverage than MODIS or SPOT-VEGETATION, spanning from 1979 to the present. Unfortunately, the AVHRR sensor has lower radiometric and geometric quality, with a 1.1 km spatial resolution at the nadir. In addition, the global archive of the full resolution AVHRR data only began in the early 1990s, so images acquired in the 1980s are only available at a degraded resolution (4 km or lower). Therefore, deriving global and accurate BA information from these data is very challenging. The AVHRR time series has been used in different regional studies to derive the BA time series, either at the full resolution of this sensor for particular regions (Chuvieco et al. 2008; Kucêra et al. 2005; Sukhinin et al. 2004) or using coarser resolution versions (8 km) with examples in Africa (Barbosa et al. 1999), Canada (Moreno Ruiz et al. 2012), Russia (García-Lázaro et al. 2018), and global coverage for the 1981–2000 period (Riaño et al. 2007). These studies have provided moderately accurate values when compared to other BA products due to the spatial and radiometric limitations of AVHRR sensors.

Despite these limitations, obtaining long BA time series from AVHRR images would be very beneficial for climate modelers as it would provide a significant temporal extension to the current BA products. This was the main motivation to conduct the present

research, which was developed within the ESA Climate Change Initiative (CCI) program's Fire_cci project (ESA 2019). Considering the existing AVHRR time series products, we selected the land long term data record (LTDR), which covers 1981–to the present at a 0.05 degree resolution (≈5 km) including acquisitions from seven different NOAA satellites (Pedelty et al. 2007). LTDR is the highest spatial resolution dataset of AVHRR images that globally covers the full lifetime of the sensor. The objective of this paper was to present the development of an algorithm to detect BA pixels from LTDR data, and analyze the outputs in relation to other existing products.

2.2. Methods

2.2.1. General Workflow

Figure 2.1 presents the flow chart with the BA algorithm structure. First, the LTDR daily data were synthetized in monthly composites and spectral indices related to the burned signal were calculated. Unburnable covers were masked out to optimize processing and avoid potential commission errors. These masked areas included bare soil, water, urban areas and permanent snow and ice, and were obtained from the Land Cover CCI project (ESA 2013). From the input bands and derived spectral indices, a synthetic BA variable (named as the LTDR BA index, or LBI to simplify) was computed. This variable tried to include the different spectral features of AVHRR data that would help to discriminate burned pixels based on experience from previous studies and LTDR sample statistics. The random forest (RF) classifier was selected to discriminate burned and unburned pixels, as it has provided good generalization potential in many recent satellite applications. To facilitate the discrimination of BA using seasonal changes, the RF models were trained using the twelve monthly LBI values of each single year as the predictor variables. The training was based on burned pixels obtained from the NASA MCD64A1 Collection 6 (from now on simply MCD64A1) BA product (Giglio et al. 2018), which produced global BA estimations from 2001 to 2017 at a 500 m spatial resolution. This product is widely used by climate modelers (Padilla et al. 2015). Previous estimations of commission and omission errors for this product were 0.336 and 0.663, respectively (Padilla et al. 2018). The MCD64A1 product was resampled at 0.05 degrees to obtain the proportion of BA within each LTDR pixel. A pixel was considered burned if it had at least 1% of BA.

The RF model was used to run the processing over the whole time series. Once the burned pixels were detected, they were assigned a proportion of BA based on the MCD64A1 dataset. Finally, the BA product (named FireCCILT10) was formatted to match the standard formats of the Fire_cci project, and made freely accessible (ESA 2019). The validation was carried out by comparing BA detections with those included in the

MCD64A1 product for those years not used in the training phase. A comparison was also made with the fire perimeters derived from national services in Australia, Canada, and California. Further details are included in the following sections.

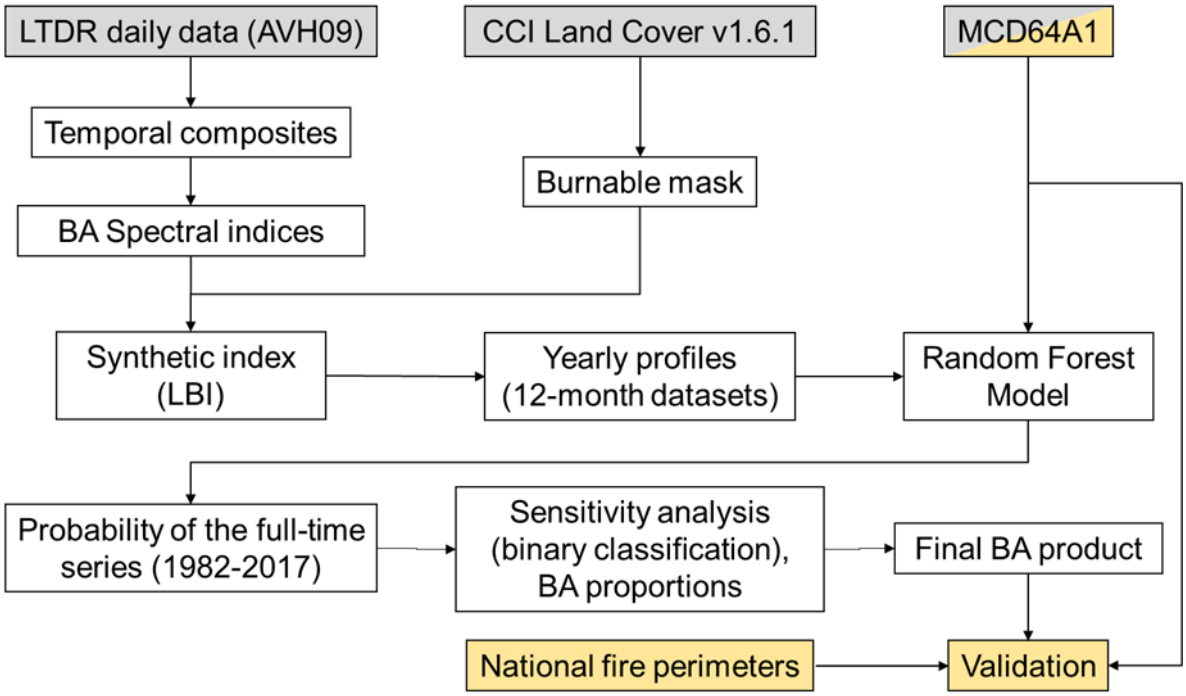

Figure 2.1. Flowchart of the methodology to obtain the FireCCILT10 BA product. The method starts with the input data (shown in grey), which are processed and converted into a BA classification. This product is validated independently in the validation step (shown in light orange).

2.2.2. Land Long Term Data Record Dataset

The LTDR Version 5 product is a dataset created by NASA to provide a corrected time series of global AVHRR coarse-resolution observations (Pedelty et al. 2007). This was generated using the global area coverage (GAC, 4 x 4 km), acquired by the AVHRR2/3 sensors on board the NOAA-7, 9, 11, 14, 16, 18, and 19 satellites (all of them have an equatorial crossing time around early afternoon). The LTDR data are available from 1981–to the present, representing the longest global time series of satellite Earth observations (38 years). However, the dataset is not fully continuous, as different observational gaps are still present. The most important one was found in 1994, which covered several months (Figure 2.2). For this reason, 1994 was not used in the generation of the FireCCILT10 product.

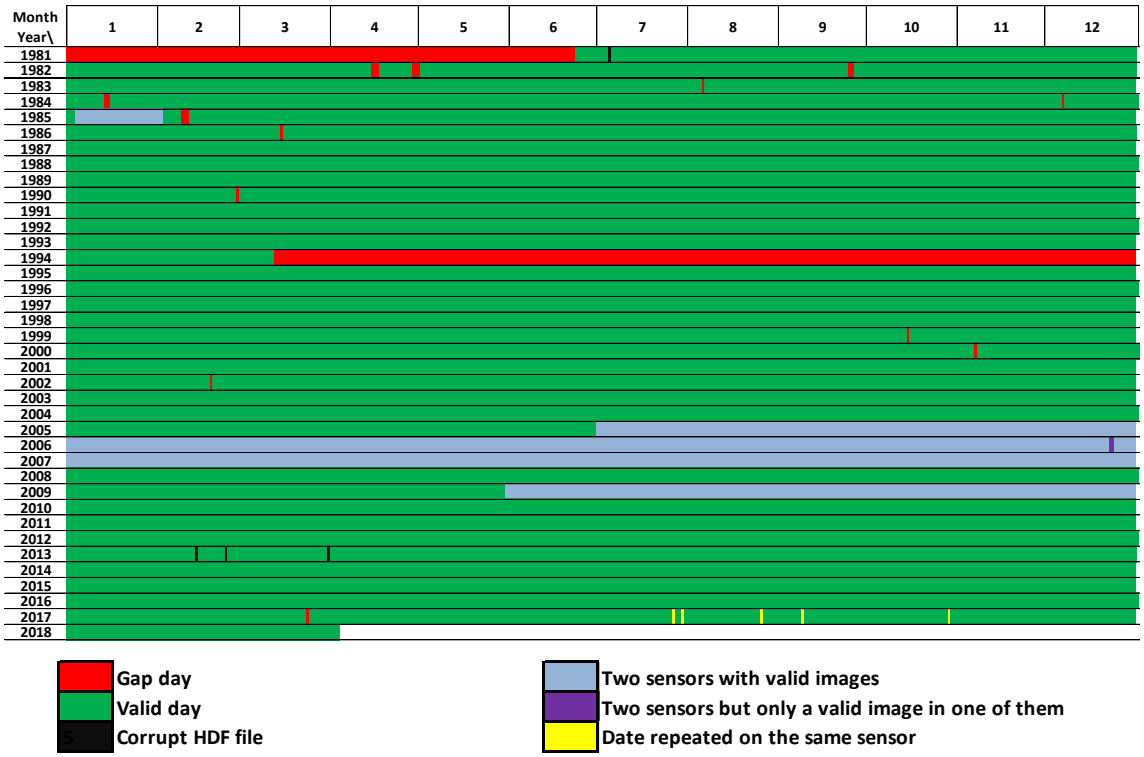

Figure 2.2. Global and daily data availability of LTDR (v5) in the time series where it was possible to find different problems such as gaps without data (as in 1994 with an eight-month gap or specific gaps in the time series), several daily images with more than one sensor, and corrupt or repeated files.

The LTDR dataset includes radiometric corrections, geometric corrections (inverse navigation to relate an Earth location to each sensor's instantaneous field of view), and atmospheric corrections (Rayleigh scattering, ozone, water vapor, and aerosol correction). For the latter, MODIS images were used to guarantee consistency, assessing the years in which they were present within the time series. However, despite the calibration among sensors, some inconsistencies were found in the visible channels (Figure 2.3) due to the degradation during the sensor's lifetime and for those periods where the new versions of the AVHRR sensor were included in the time series.

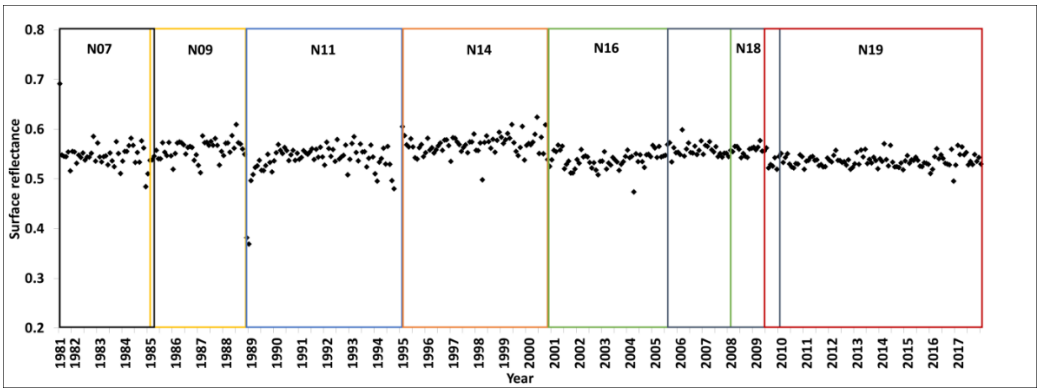

Figure 2.3. Evolution of near infrared reflectance (channel 2) in the time series. A pixel in the Sahara Desert was selected to better observe the radiometric stability of the different AVHRR sensors, as this area is very stable throughout time (Horion et al. 2014; Myneni et al. 1997). In the shift of the different sensors, the greatest instabilities were shown when new versions of the AVHRR sensor were used such as in 2000 with NOAA 16. N07 to N19 indicate the satellite where the AVHRR was mounted, meaning from the NOAA-7 to the NOAA-19 satellites.

The LTDR product has ten bands. The original bands are surface reflectance for channel 1 (0.58–0.68 µm) and channel 2 (0.725–1.1 µm) (red and near infrared, respectively), medium infrared (surface reflectance and top of atmosphere (TOA) brightness temperature for channel 3, 3.55–3.93 µm), and thermal infrared (TOA brightness temperature for channel 4, 10.3–11.3 µm and TOA brightness temperature for channel 5, 11.5–12.5 µm). In addition, LTDR includes the view zenith angle, solar zenith angle, relative azimuth, and quality assessment field (QA). Two bands show several problems. First, the AVHRR2 sensor was changed for AVHRR3 in 2000 with NOAA-16. The new version of the sensor included a change of configuration in channel 3 between daytime (channel 3a, 1.58–1.64 µm) and night-time (channel 3b, the 3.55–3.93 µm original configuration), which implied a modification of daily reflectance and temperature for this band (Figure 2.4). In 2003, the historical configuration was restored. Furthermore, saturation of channel 3 on the AVHRR2 sensor was increased in the AVHRR3 sensor to 63 degrees (Trishchenko et al. 2002), so this channel was also not consistent with previous versions (Figure 2.5). On the other hand, the QA information was found to be not sufficiently accurate as many cloudy and noise pixels observed visually were not properly masked. Therefore, this layer was finally not used.

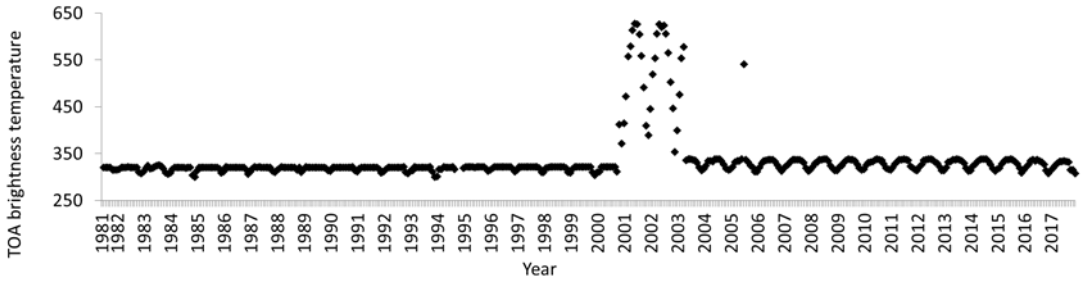

Figure 2.4. Time series of brightness temperature for channel 3 (3.55–3.93 µm) for a pixel located in the Sahara Desert. The impact of changes related to the daytime configuration of AVHRR3 (1.58–1.64) can be clearly seen between 2000–2003. In 2003, the previous configuration was restored.

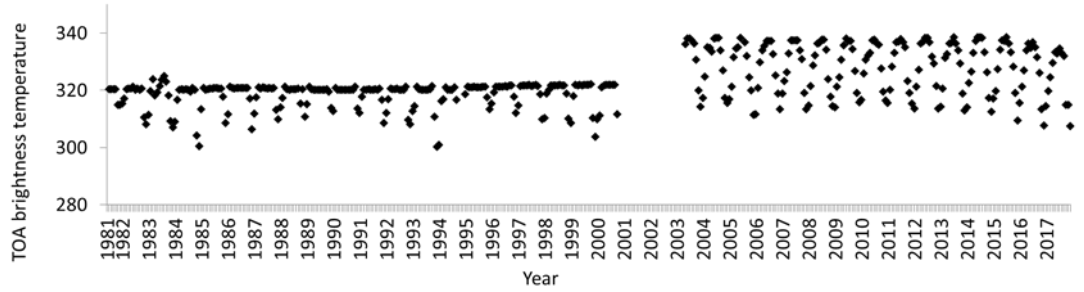

Figure 2.5. Difference between AVHRR2/3 in a Sahara Desert pixel of channel 3 (3.55–3.93 µm). The saturation between AVHRR2/3 was different: AVHRR2 was saturated at 50 °C and AVHRR3 at 63 °C. Therefore, before 2000 (AVHRR2), the data were distributed in a narrower range than after 2000 (AVHRR3). This implies a significant variation between the sensors.

2.2.3. Composites

LTDR daily data are difficult to process because they are affected by noise, clouds, shadows, very oblique angles, radiometric instability, and other artifacts. Monthly composites (Figure 2.6) have been commonly used instead (Tian et al. 2015) to retain the highest quality observations of a daily dataset. Among the different criteria for creating image composites, we selected the maximum temperature of channel 4 (10.3–11.3 µm), as it has been proven to provide good sensitivity to detect burned pixels while avoiding clouds and cloud shadows (Chuvieco et al. 2005). The compositing algorithm also included a burnable mask derived from the ESA's CCI Land Cover v1.6.1 product (ESA 2013). The land cover product was reclassified (burnable and unburnable) and resampled from the original 300 m resolution to the LTDR resolution (0.05 degree), thus obtaining the proportion of burnable area within each pixel. All pixels with a proportion of burnable area lower than 20% were masked and discarded from the analysis. We selected the year 2000 from the different available epochs of this product as being representative of the average cover conditions of the target period.

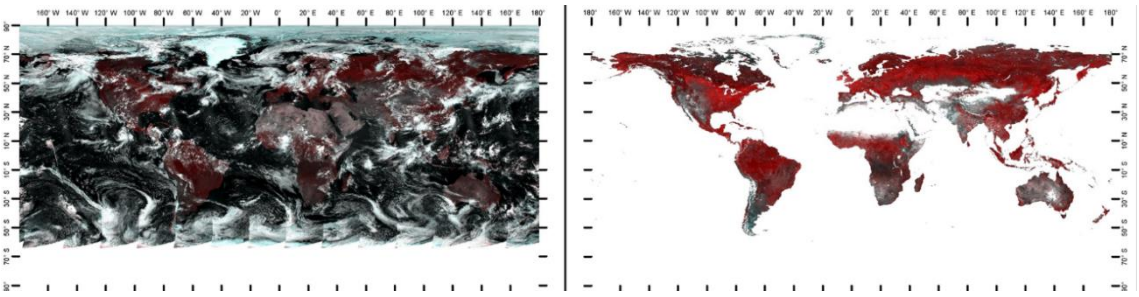

Figure 2.6. Impact of temporal compositing for the LTDR data. (Left) Daily images acquired on July 18, 2008. (Right) Monthly composite for July 2008 with the unburnable classes removed. In both cases, the RGB color composition used NIR, red, and red reflectances.

2.2.4. Input Bands

To analyze the spectral separability of burned and unburned pixels, the original bands and different spectral indices previously used in BA studies and others used for vegetation dynamics were computed (Table 2.1). In addition, the monthly temporal differences of those indices were also calculated

Table 2.1. Derived bands generated as inputs for the BA algorithm. References for previous studies using each index for BA discrimination are included.

Index	Formula	Developer	BA application
Normalized Difference Vegetation Index	$NDVI = \frac{\rho_{NIR} - \rho_{RED}}{\rho_{NIR} + \rho_{RED}}$ ρ_{NIR} = surface reflectance for channel 2 (0.725–1.1 µm) ρ_{RED} = surface reflectance for channel 1 (0.58–0.68 µm)	(Rouse et al. 1974)	(Grégoire et al. 2003; Simon et al. 2004)
Global Environmental Monitoring Index	$\mathrm{GEMI} = \eta \cdot (1 - 0{,}25 \cdot \eta) - (\frac{\rho_{RED} - 0{,}125}{1 - \rho_{RED}})$ $\eta = \frac{(2 \cdot (\rho_{NIR}{}^2 - \rho_{RED}{}^2) + 1{,}5 \cdot \rho_{NIR} + 0{,}5 \cdot \rho_{RED})}{\rho_{NIR} + \rho_{RED} + 0{,}5}$	(Pinty and Verstraete 1992)	(Barbosa et al. 1999; Chuvieco et al. 2008)
Burned Area Index	$\mathrm{BAI} = \frac{1}{(\rho c_{RED} - \rho_{RED})^2 + (\rho c_{NIR} - \rho_{NIR})^2}$ Where ρc_{NIR} and ρc_{RED} are the convergence values for burned vegetation (defined for AVHRR as 0.06 and 0.1, respectively).	(Martín and Chuvieco 1998)	(Chuvieco et al. 2008)

Table continued on next page.

Table 2.1 – continued from previous page.

Index	Formula	Developer	BA application
Soil Adjusted Vegetation Index	$SAVI = \frac{\rho_{NIR} - \rho_{RED}}{\rho_{NIR} + \rho_{RED} + L} \cdot (1 + L)$ Being L soil reflectance (in this case L = 0.5)	(Huete 1988)	(Chuvieco et al. 2002)
Modified Soil Adjusted Vegetation Index	$MSAVI = 0.5 \cdot [(2 \cdot \rho_{NIR} + 1)^2 - 2((2 \cdot \rho_{NIR} + 1)^2 - 8(\rho_{NIR} - \rho_{RED}))^{\frac{1}{2}}]$	(McGwire et al. 2000)	(Barbosa et al. 1999)
Surface Temperature	$Ts = T4 + 3.33(T4 - T5)$ T4 = TOA brightness temperature of channel 4 (~10.3–11.3 μm) T5 = TOA brightness temperature of channel 5 (~11.5–12.5 μm)	(Barbosa et al. 1997)	(Barbosa et al. 1999)

A statistical analysis was carried out to select the most sensitive variables to discriminate between burned and unburned pixels. A sampling of more than 450,000 burned and more than 50 million unburned pixels was selected. Burned pixels were extracted from the MCD64A1 product, which was used as the reference dataset to generate the classification model. We used 2008 as the calibration year for this analysis. We computed the median and interquartile range values for each input band to analyze whether expected trends (for instance, lower NDVI for higher burned proportions) of each input band were observed. Additionally, RF models were run to select the most explicative variables for BA discrimination, but the results were not conclusive.

2.2.5. LTDR Burned Area Index

Several RF models were generated from the original and derived bands (Table 2.1), but the results showed severe confusion between the burned and unburned pixels. Therefore, we decided to base our models on a dedicated synthetic index that aimed to combine the most sensitive variables for BA discrimination in a single variable. We named this index, the LTDR BA Index (LBI), which included various spectral dimensions of fire effects such as low NIR and R reflectance and GEMI values, high temperature, temporal decrease in NIR reflectance and GEMI values, and increase in temperature. These trends were observed in our dataset as well as in several previous studies on BA discrimination (Chuvieco et al. 2019).

All variables (X) were normalized (z-score), to reduce the impact of temporal instability in the time series using the means (μ) and standard deviations (σ) for each month:

$$z = \frac{X - \mu}{\sigma}$$

The final formula of the LBI was:

$$LBI = z(T5) - z(T5\_diff) - z(Red) + z(Red\_diff) - z(NIR) + z(NIR\_diff) + z(GEMI) + z(BAI) + z(BAI_t + 1)$$

where t is the monthly composite being analyzed; t + 1 is the composite of the following month and t − 1 is the composite of the previous month; diff is the difference between t − 1 and t; T5 is the TOA brightness temperature of channel 5 (~11.5–12.5 μm); Red is the surface reflectance of channel 1 (0.5–0.7 μm); and NIR is the surface reflectance of channel 2 (0.7–1.0 μm).

Figure 2.7 shows the comparison of monthly LBI values for the burned and unburned pixels in different tropical regions (Giglio et al. 2013). To facilitate the comparison between pixels in different hemispheres, the figure indicates the months before and after the fire occurrence. The higher values of LBI indicate a higher likelihood of burning. The burned pixel shows a clear variation around the date of the burning, while the unburned shows a more stable trend. The increase of LBI values before the fire may be related to an increase in vegetation dryness (thus reducing chlorophyll activity) and temperature.

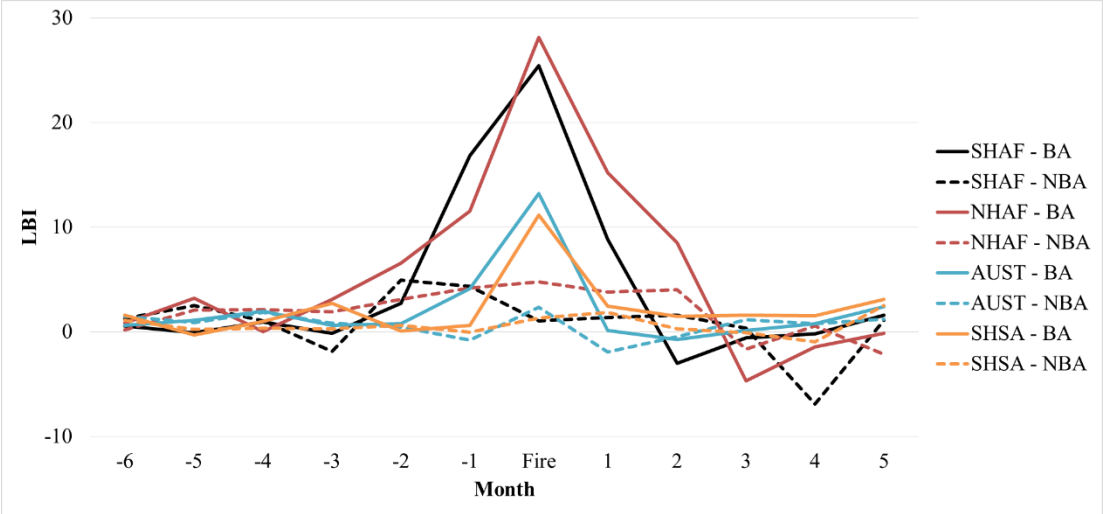

Figure 2.7. Monthly variation (2008) of the LTDR BA Index for an example of the burned area (BA) and unburned area (NBA) pixels. Southern Hemisphere South America (SHSA), Europe (EURO), Northern Hemisphere Africa (NHAF), Southern Hemisphere Africa (SHAF), and Australia and New Zealand (AUST).

Figure 2.8 shows the global LBI values in July 2008. As expected, larger values were observed in the Southern Tropical fringe of Africa, which commonly burns during this period. Great values were also observed at high latitudes (>60°) where the quality of the LTDR data decreased or artifacts were observed. These outliers did not affect BA discrimination as their temporal trend did not show the clear seasonal variability observed for burned pixels.

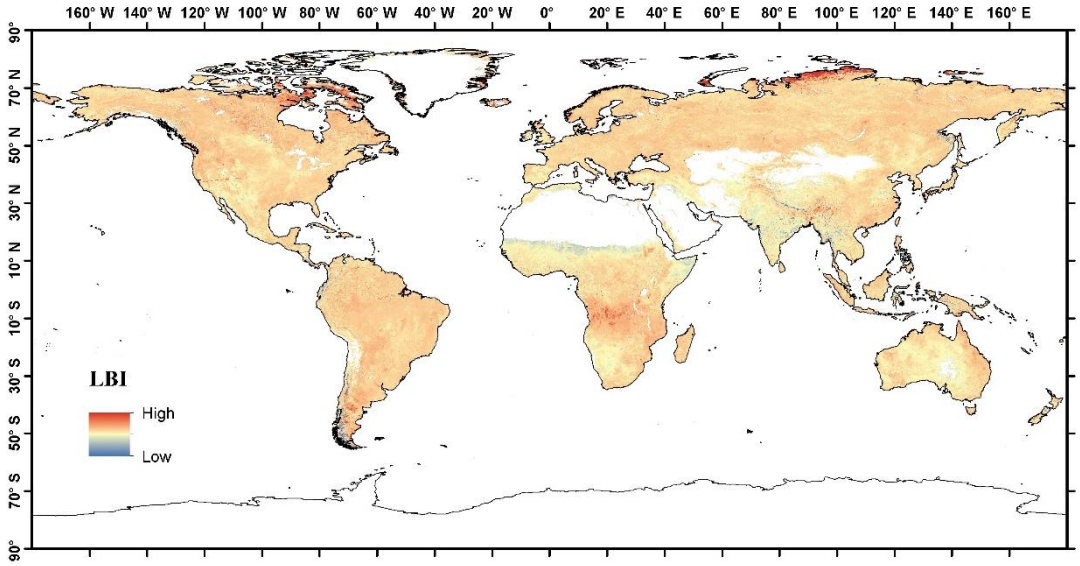

Figure 2.8. LBI values for July 2008. Higher LBI values were observed in the Southern Hemisphere tropical regions, when the dry period occurred.

2.2.6. Random Forest Model

The RF algorithm was selected to create the LTDR BA classification because it has been shown to be quite robust in many land cover classification studies (Belgiu and Drăguţ 2016; Pelletier et al. 2016; Rodriguez-Galiano et al. 2012) that also includes BA discrimination (Long et al. 2018; Ramo and Chuvieco 2017; Ramo et al. 2018). RF is a machine learning algorithm that is based on generating a combination of decision trees that are independent of each other. Each decision tree randomly selects a subset of input pixels, which are discriminated using the predictor variables. A pixel is assigned to a category according to the majority vote of the ensemble of trees.

For this particular classification, the RF parameters were defined following our previous studies (Ramo and Chuvieco 2017; Ramo et al. 2018). Six hundred decision trees were selected as this was found to be a good number to reach that had acceptable precision without greatly increasing the processing time. To cope with the high unbalanced character of our sample (the vast majority of pixels were unburned), a 10% proportion

of the BA pixels were forced to be included in each decision tree. The data entered in each tree were selected randomly, establishing only the percentage of each class.

Monthly RF models were developed to better adjust the fire conditions of each month. Several factors were considered to build the RF models: (1) the number of months during the year by analyzing the impact of the temporal seasonality on the models; (2) the number of input years to be able to obtain a generalized model that was valid for the full time series; and (3) the proportions of the burned area in the MCD64A1 that should define a pixel as burned.

RF models were run with a different number of input months within a year. When just using three months (t, t − 1 and t + 1) the model did not show good performance. The number of months was subsequently increased from seven (three months before, month of study, and three months after) to the whole year to further consider seasonal variability. The latter showed the best performance, as the 12 months included a more complete temporal evolution of the pre- and post-fire conditions.

The first RF models were trained with only one year (2008), but the resultant model performed poorly in other years. Therefore, training was based on several sets of years to avoid the overtraining bias. We found a stable and consistent model with eight years of training data (2001, 2003, 2004, 2006, 2008, 2011, 2013, and 2015) and included years with different global fire occurrences such as 2004 and 2011, which had the highest occurrence, and 2013, which had the lowest.

Finally, different RF models were trained with several proportions of BA within a pixel by taking this information from the reference MCD64A1 product. Five percentile classes (0, <25, 25–50, 50–75, >75), four classes (0, <40, 40–80, >80), three classes (0, <50, >50), and two classes (0, >80) were tested. They showed severe overtraining or inaccurate results, since most of the burned pixels were in the low percentage range. Finally, two classes (burned/unburned) were used, where burned was classified as those LTDR pixels with any proportion of burned (=>1%).

In summary, our BA product (named FireCCILT10) was based on 12 RF monthly models, each trained with eight years of data and with two output classes (burned/unburned) (Figure 2.9). In all cases, the predictor variables were the 12 monthly LBI values of each input year. The training dataset had around one million burned pixels and around thirty million unburned pixels. The RF classification was performed with the monthly models and for the full time series of the LTDR dataset excluding the year 1994. A total of 420 classifications (12 months x 35 years) were performed to obtain the final product. The

RF output provided the probability (between 0 and 1) of a pixel to be burned per month and year.

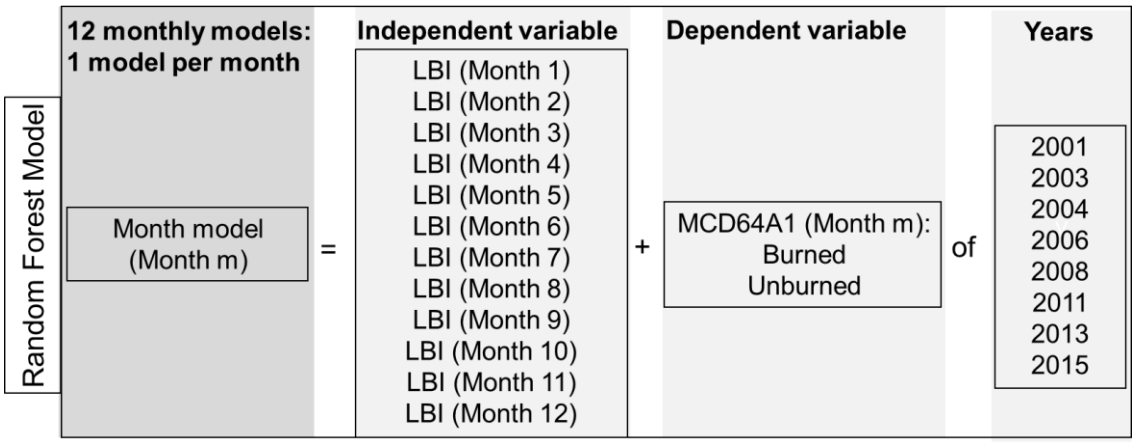

Figure 2.9. Representation and composition of the random forest model. Twelve monthly models were created using two variables with the data from eight years.

A sensitivity analysis was carried out to convert the RF probabilities into a binary classification, using MCD64A1 data for the overlapping period (2001–2016). Different cut-off thresholds (between 0.00 and 1.00) were used to evaluate the ones that classified the LTDR pixels more similarly to the MCD64A1 product. The proportion with the highest dice coefficient (DC) for each month was used. DC is a statistical index that integrates the omission and commission error of the BA class (Dice 1945). Since each year showed slight variations in the monthly thresholds, we used the median value of all years for each month as a cut off value for that month to obtain the burned–unburned classification during the whole time series. The RF probability of the burned assignment was also kept to compute the uncertainty of the BA detection, which was offered as an auxiliary variable of the final FireCCILT10 product.

2.2.7. Estimation of Burned Proportions

Once the binary classification was obtained, the final phase was to assign a certain proportion of the burned area to each burned pixel. Considering a burned LTDR pixel as fully burned was not realistic, as it is unlikely that such a large area (around 25 km2) would be completely affected by fires. For this reason, the pixels classified as burned were converted to a proportion of burned using the MCD64A1 product as a proxy of the true BA. The aim was to obtain a relationship that would provide a similar total BA to the MCD64A1 and LTDR products for the overlapping period, and then use that relation to extrapolate backwards.

This analysis was performed at a grid-cell level, with cells having a 0.25-degree spatial resolution (5 x 5 LTDR pixels). First, we computed the actual BA for each cell during the overlapping period from the MCD64A1. Then, for each cell, we estimated the proportion of burned pixels that would sum up the total BA estimated by the MCD64A1 product (Figure 2.10). This process was done for each cell and each month of the existing MCD64A1 time series.

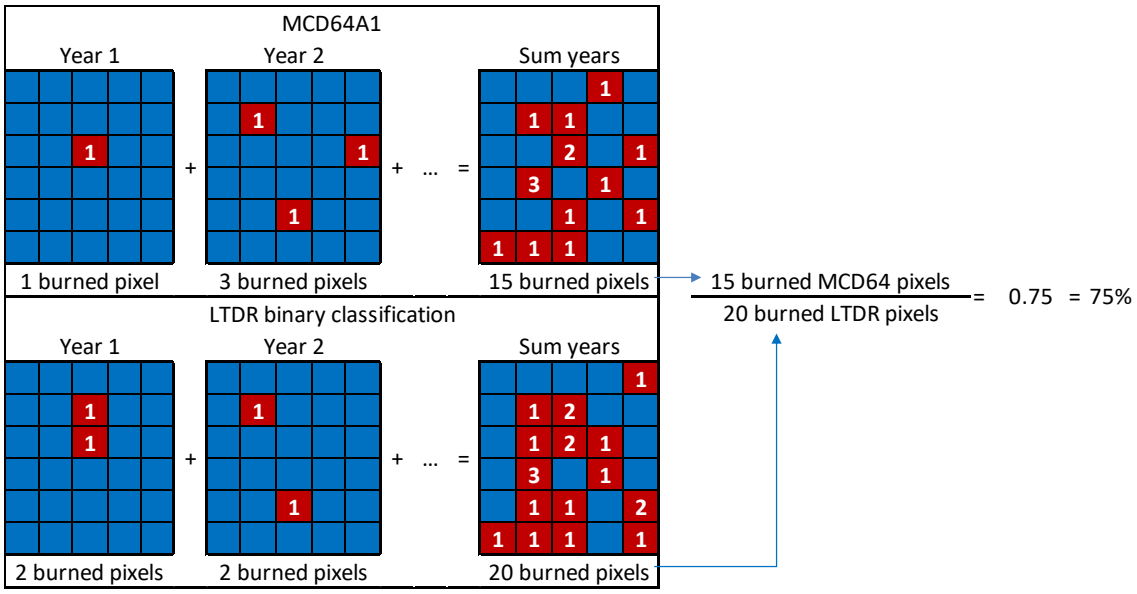

Figure 2.10. Calculation of the percentage of Burned Area for the 0.25° cell. The MCD64A1 had 15 pixels classified as burned after aggregating all years during the time series. The LTDR product had 20 pixels classified as burned for the same period. Therefore, each LTDR pixel for this cell was considered to be 75% burned.

2.2.8. Number of Observations

We computed the number of observations as a potential source of error in the classification process. This variable was computed as the total daily observations in each month minus the number of days in which each pixel had "No data values" or reflectance equal to or greater than 90% (considered noise). The total number of observations varied throughout the months (28–31 days) and the number of NOAA-AVHRR satellites (1 or 2) that were active that day. An example of this calculus is included in Figure 2.11. Generally, a higher number of observations were found nearby the Equator, while boreal regions had the lowest.

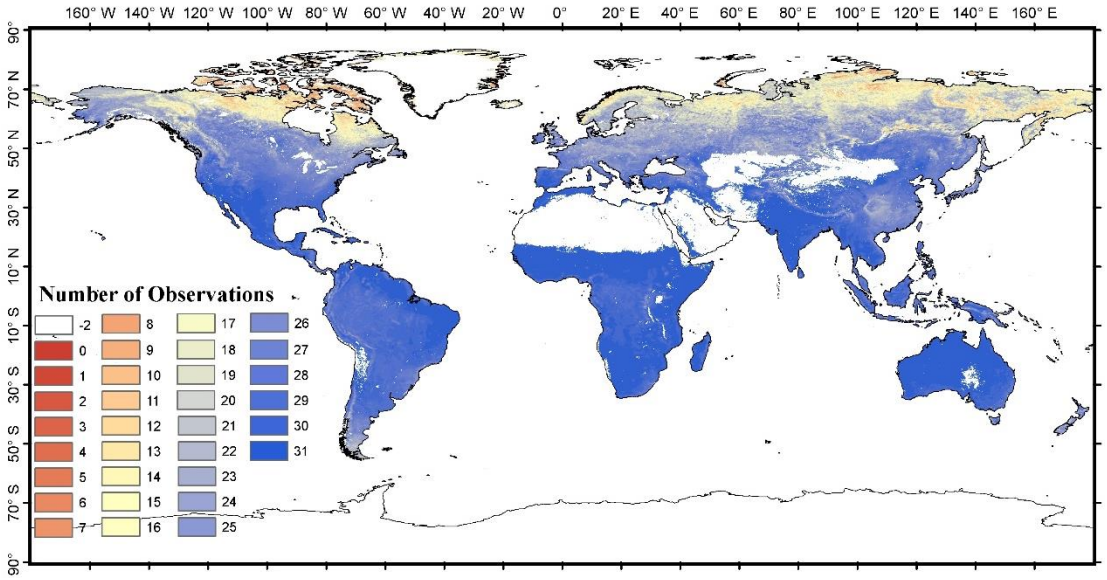

Figure 2.11. Average number of observations per month in the time series. The number of observations shows the number of good observations (without "no data values" or reflectance equal to or higher than 90%).

2.2.9. Validation

Using Landsat data to validate the product would produce unrealistic estimations of accuracy, considering the large difference in spatial resolution between these two sources of data. In addition, our product was expected to have a low temporal reporting accuracy, as it was built from monthly composites, which would make the comparison with short acquisition periods between two Landsat observations difficult.

For these reasons, a preliminary validation of the FireCCILT10 product was based on comparing the BA estimation of this product with the MCD64A1 for the eight years not used in generating the RF models (2002, 2005, 2010, 2012, 2015, 2016, and 2017). We compared areal estimations of our product with those of MCD64A1 for continental regions (Giglio et al. 2013) by computing the correlation and regression parameters for the eight years between the two datasets.

In addition, we compared our results for the long time series with several national fire perimeters, which are representative of different fire biomes and have a long time series. We included fire perimeters from the Canadian Wildland Fire Information System (Canadian Forest Service 2017), the state of California (FRAP 2019) and the North Australian Fire Information database (NAFI 2019). The first two include fire statistics that covered the full time series of our LTDR BA product.

2.3. Results

2.3.1. Spatial Patterns

Figure 2.12 shows the spatial patterns of BA detected by the FireCCILT10 product in relation to the MCD64A1 in 2016. Africa was the most burned continent, especially at the tropical fringes. A total of 74.37% of the whole BA occurred in Africa. MCD64A1 aggregated at 0.05 degrees showed only 2.5% more pixels burned than FireCCILT10, with more detections in the northern latitudes, while FireCCILT10 showed a higher concentration of BA in tropical regions. The main differences between the two products were found in boreal regions and northern South America. In Africa, great similarities were observed, specifically in sites where there was more BA.

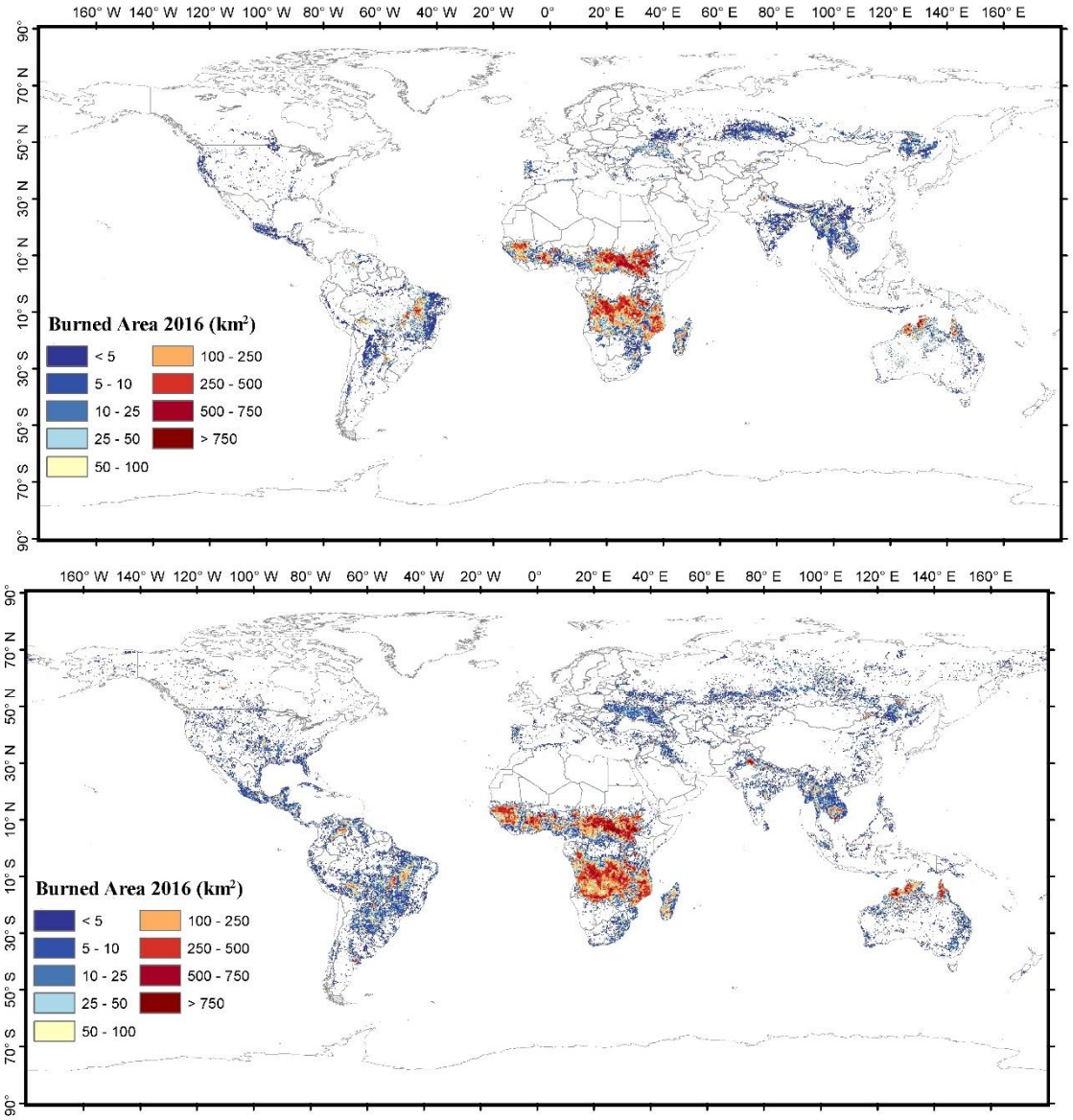

Figure 2.12. FireCCILT10 (**top**) and MCD64A1 (**bottom**) burned area in 2016.

According to the continental regions (Giglio et al. 2013), MCD64A1 estimated more BA than FireCCILT10 in each region (Table 2.2), although they showed similar spatial variability. Southern Hemisphere Africa was the most burned region, followed by Northern Hemisphere Africa. Australia and New Zealand and Southern Hemisphere South America were also greatly affected by fire in both BA products. Europe, the Middle East, and Equatorial Asia were the least burned regions.

The highest discrepancies between the MCD64A1 and the FireCCILT10 were found in boreal regions, where the latter product showed a clear underestimation. This should be related to the low quality observations of the LTDR time series in northern latitude regions, where many months had less than five valid images.

Table 2.2. Average Burned Area of the FireCCILT10 and MCD64A1 products (2001-2017) in the continental regions. Boreal North America (BONA), Temperate North America (TENA), Central America (CEAM), Northern Hemisphere South America (NHSA), Southern Hemisphere South America (SHSA), Europe (EURO), Middle East (MIDE), Northern Hemisphere Africa (NHAF), Southern Hemisphere Africa (SHAF), Boreal Asia (BOAS), Central Asia (CEAS), Southeast Asia (SEAS), Equatorial Asia (EQAS) and Australia and New Zealand (AUST).

Continental Region	**BONA**	**TENA**	**CEAM**	**NHSA**	**SHSA**	**EURO**	**MIDE**
MCD64A1 (Mkm^2)	0.428	0.478	0.468	0.894	5.002	0.186	0.239
FireCCILT10 (Mkm^2)	0.093	0.187	0.201	0.463	3.519	0.102	0.050
Continental Region	**NHAF**	**SHAF**	**BOAS**	**CEAS**	**SEAS**	**EQAS**	**AUST**
MCD64A1 (Mkm^2)	21.917	25.927	1.586	3.417	2.358	0.260	8.702
FireCCILT10 (Mkm^2)	20.348	22.984	0.745	1.378	1.948	0.100	5.204

In terms of land cover, the most affected category was tree cover, broadleaved, deciduous, closed to open (>15%) with 49.27% of the total burned area, followed by shrubland (25.59%), and rainfed cropland (8.49%).

2.3.2. Temporal Trends

The FireCCILT10 BA product includes thirty-six years of global BA (1982–2017, excluding 1994). The average yearly BA was 3.12 Mkm2, with a maximum burned area of 4.45 Mkm2 in 2011 and minimum burned area of 1.74 Mkm2 in 1988 (Figure 2.13). Annual BA estimations from the FireCCILT10 product showed a high inter-annual variability from 1982 to 2000, with more stable trends after 2001 and during the common period with MCD64A1. Decreasing BA at the end of the period (2012–2017) was observed in both products, although it was more evident in FireCCILT10.

Seasonal fire trends were distributed by regions, in particular, the northern hemispheric tropical belt at the end and beginning of the year and the southern hemispheric tropical belt in the middle of the year. Monthly average BA indicated that December and September had the highest values of BA with 0.44 Mkm2 and 0.38 Mkm2, respectively, and April (0.09 Mkm2) and May (0.10 Mkm2) had the lowest.

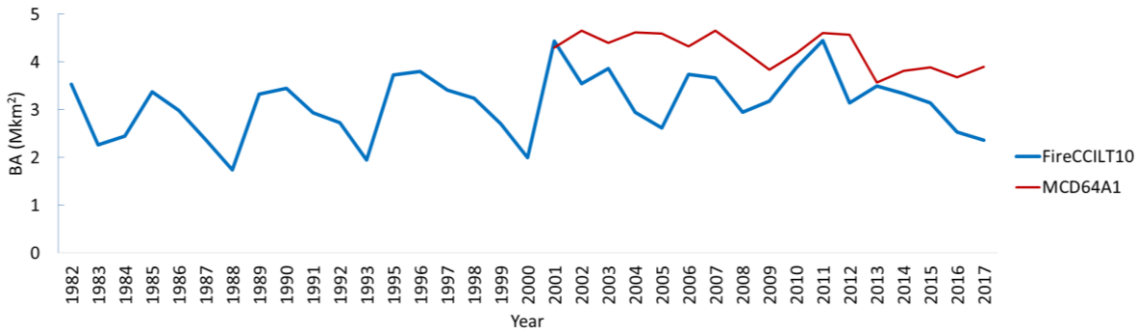

Figure 2.13. BA annual trends of the MCD64A1 and FireCCILT10 BA products.

2.3.3. Validation Results

Figure 2.14 shows the scatterplot of the BA estimations for the MCD64A1 and FireCCILT10 products in the different continental regions. Only the eight common years not used in the training phase were included in this graph. Global correlation was highly significant, although it was highly influenced by the most burned regions (both hemispheres of Tropical Africa). Average estimations for all regions indicate a tendency toward underestimation (18%), according to the slope value. Figure 2.15 shows the temporal evolution of residuals for the different continents. Residuals are the difference between the MCD64A1 and FireCCILT10 multiplied by the slope of the BA estimations. The larger values corresponded to the most burned regions, with significant underestimation in Australia in 2012 and Southern Hemisphere Africa in 2005 and 2017. A large overestimation was found in the same area in 2010 and, less relevant, in Northern Hemisphere Africa for the same year. Boreal regions and Central Asia showed a consistent underestimation in all validation years.

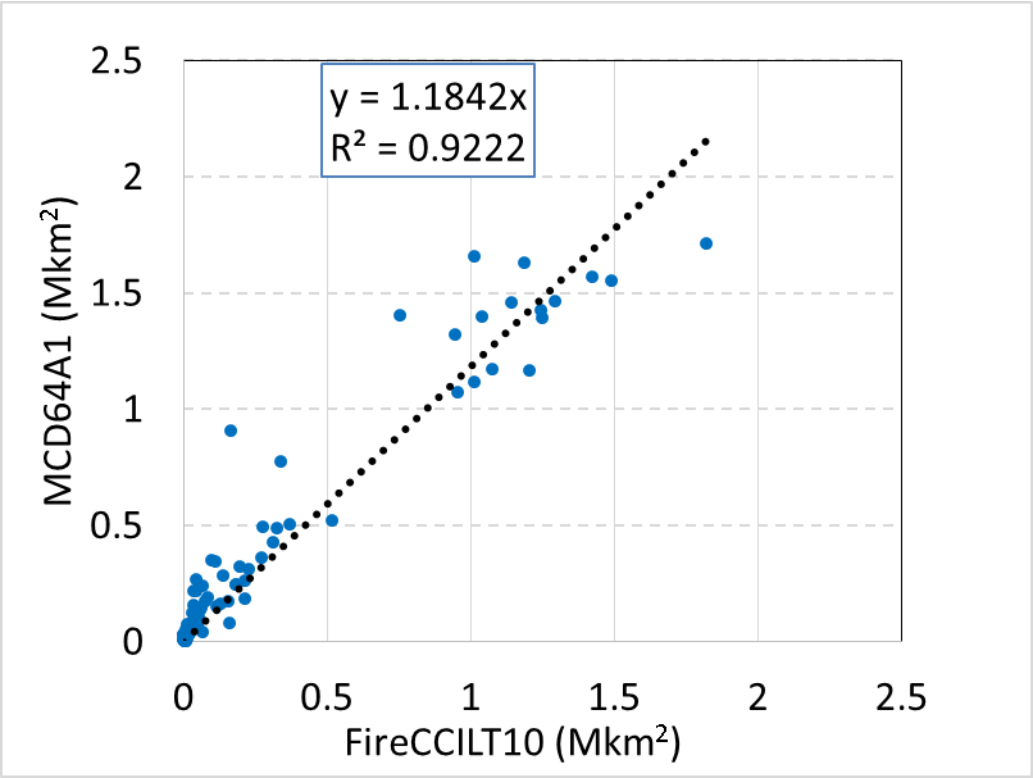

Figure 2.14. BA estimations of the MCD64A1 and FireCCILT10 products for the continental regions.

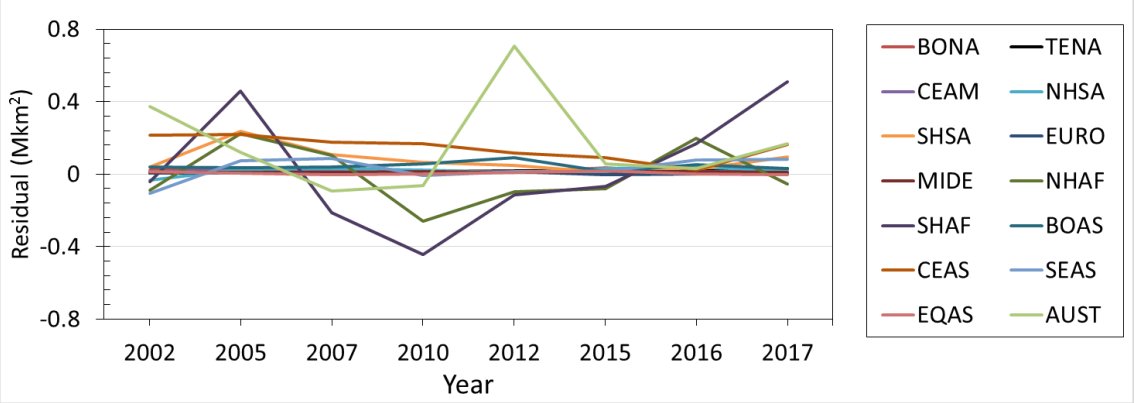

Figure 2.15. Temporal variability of residuals for the different continental regions (for acronyms see the caption of Table 2.2).

Comparison of the FireCCILT10 BA estimations and national fire perimeters (Figure 2.16) showed the limitations of our product, particularly for boreal regions (the example was from Canada), where the fire trends were not well captured, mainly in the pre-MODIS era. For California, the trends were unstable, with a high overestimation in 1992 and underestimation in 2008. The time series had better agreement with the national perimeters after 1998. The FireCCILT10 estimations for the Northern Australia BA were also unstable, with better agreement for the years with lower occurrence. This Australian database only started in 2001 as it is derived from MODIS 250 m data.

Unfortunately, there are no fire perimeters for other tropical regions, where our product should produce better agreement than for temperate or boreal regions. The agreements of the national perimeters and the MCD64A1 product were quite reasonable for the three datasets.

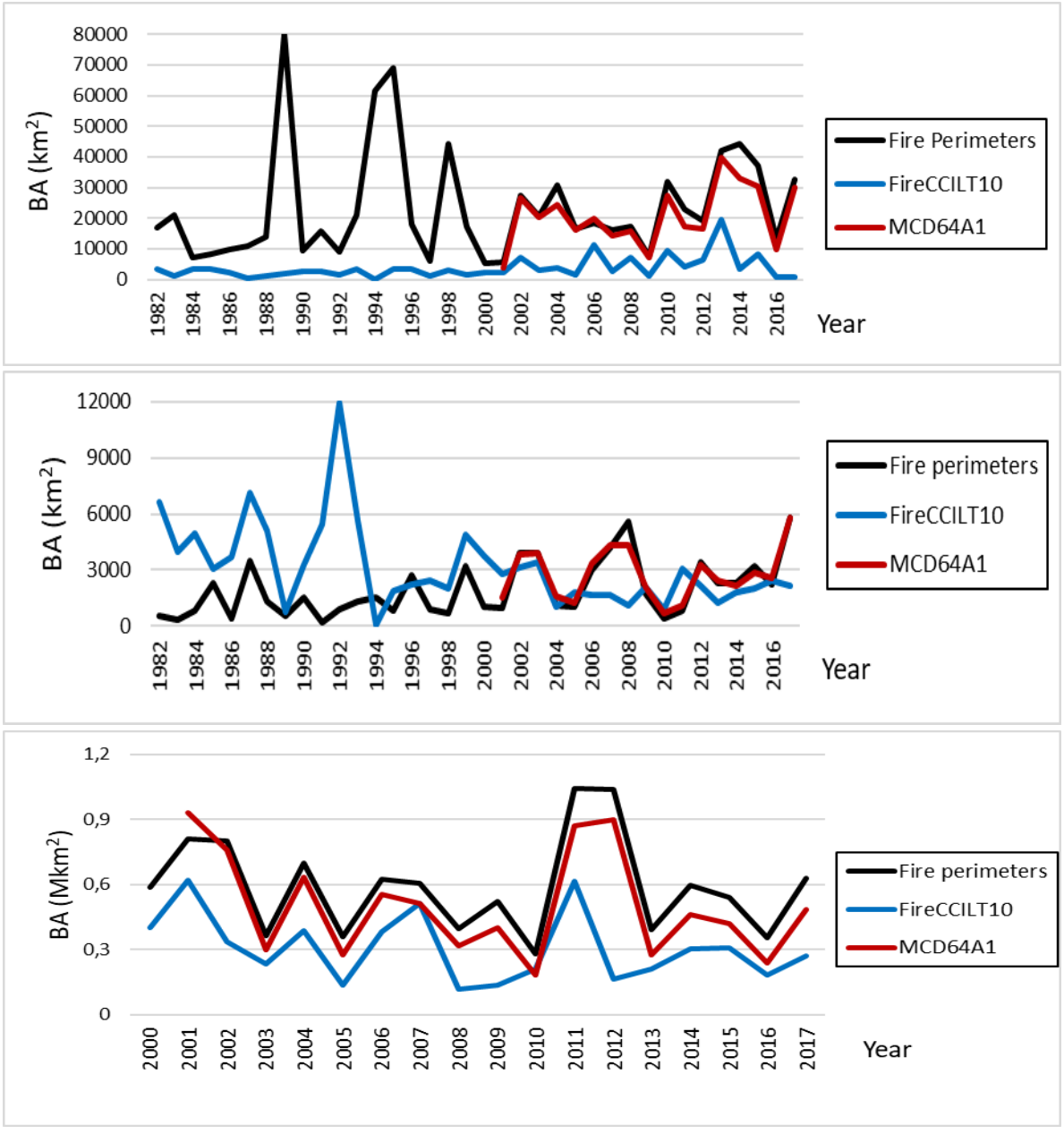

Figure 2.16. Comparison of the BA trends between FireCCILT10, MCD64A1, and the national fire perimeters: Canada (**top**), California (**center**), and Northern Australia (**bottom**). Note that the vertical scale is quite different among sites, as they have very different fire occurrences.

2.4. Discussion

This paper presents the design and prototype processing of a BA algorithm adapted to LTDR data. The final product offers the longest BA time series currently available. Considering the radiometric and spatial limitations of the LTDR data, detecting BA from this data was very challenging, but also attractive for serving the needs of the climate and atmospheric modeling community. The coarse pixel size of LTDR makes the discrimination of the burned signal very complex as a significant proportion of the 0.05° pixels had to be burned to observe significant changes in reflectance or temperature. In fact, existing global BA products based on 250 or 500 m MODIS images have shown great difficulties in discriminating BA in small fire patches or low intense fires (Chuvieco et al. 2018; Giglio et al. 2018). These problems are emphasized when working at a much coarser spatial resolution.

Classifying an LTDR pixel as fully burned might have created severe BA overestimation. Therefore, we had to develop a method to convert a binary classification to percentages of BA. We based this analysis on existing BA datasets (MCD64A1) for the common periods, which corrected overestimations, but obviously incorporated the errors of that reference BA dataset.

Another challenge of using LTDR for BA classification is related to the temporal inconsistencies of the middle infrared channel of LTDR. This channel (#3) was changed during the period 2000–2003, moving from the previous 3.7 microns range to an alternative day/night configuration. These changes, plus the lower radiometric stability of this channel, precluded its use for detecting active fires. Active fires are widely used in BA detection (Alonso-Canas and Chuvieco 2015; Chuvieco et al. 2018; Giglio et al. 2018) as their strong thermal contrast from the background is much easier to detect than reflectance changes. Consequently, discriminating burned areas without active fire information creates many difficulties in separating BA from other covers with strong temporal changes (seasonal floods, deforestation, cropping, etc.).

Another limitation of the LTDR dataset is the temporal inconsistencies of the reflectance among the satellites (Tian et al. 2015). For this reason, different years were used to train the RF models, although they were restricted to the most recent ones, when MODIS BA was available. Considering the seasonal variability of fire impacts, particularly in the Tropics, different RF models were created for each month of the year and assumed similar patterns between the pre- and post-MODIS eras.

The last limitation of the LTDR series regards to the QA inconsistencies: their low quality does not allow the identification of artifacts such as clouds.

The design of the LTDR BA algorithm was based on trying to solve all of these challenges. Composites were used instead of daily images to reduce the impact of clouds, unobserved areas, and artifacts by using the maximum temperature criterion previously tested in other studies (Chuvieco et al. 2005). However, compositing potentially reduces the temporal reporting accuracy, as the output composites may have different dates for neighbor pixels.

RF models were selected as they are more robust than other techniques to inconsistencies in input data, while they provide great generalization potential. After several RF test trainings with the original variables, it was decided to generate a synthetic index to facilitate the generalization of the RF models to global BA conditions. In addition, several authors have shown that RF models improve their accuracy with a small number of well-selected and non-redundant input variables (Dillon et al. 2011; Ramo et al. 2018). The resulting variable (named LBI) is an empirical index, derived from the statistics of burned and unburned pixels, but also based on the experience of previous BA studies (Alonso-Canas and Chuvieco 2015; Barbosa et al. 1997; Chuvieco et al. 2018; García-Lázaro et al. 2018; Ramo and Chuvieco 2017). This index included red and NIR reflectance, temperature, and some spectral indices. Both the original data and indices considered monthly values and temporal differences. All were normalized using each month's global statistics to reduce the impact of the temporal instability of the LTDR dataset. RF models were created using the annual variability of the LBI to better discriminate burned areas from other covers that have a strong temporal variation.

As expected, the FireCCILT10 product had lower accuracy values than the other global BA products based on higher resolution sensors. Further efforts are required to improve BA detection, particularly to reduce the impacts of sensor changes in the pre-MODIS era. FireCCILT10 showed good agreement with MCD64A1 at the continental level, although the performance was much higher for tropical than for temperate or boreal regions. Average yearly BA of FireCCILT10 for the common years was lower than MCD64A1 (3.37 Mkm2 versus 4.23 Mkm2, respectively). In terms of the stability of the temporal series, unrealistic changes between consecutive years were observed in the FireCCILT10 product. The factors that influenced the inter-annual variability were the number of observations, the changes in satellite orbit, and the intercalibration among the AVHRR sensors of different satellites (Tian et al. 2015).

Future efforts should concentrate on stabilizing the BA temporal series and increasing the sensitivity of the BA product to boreal and temperate regions, where fire occurrence is much less important than in tropical areas. Alternative classification methods (support vector machines, deep learning) will also be tested.

2.5. Conclusions

FireCCILT10 is the first global BA dataset developed from the LTDR product (v5) and includes the longest time series of BA (1982–2017) currently available.

The algorithm was based on a synthetic index that integrated different input variables to emphasize the burned signal. The BA algorithm was built using RF models and trained with MCD64A1 BA data. Monthly models were created with a set of contrasted years to be more generalized. The probabilities of burning were converted to binary burned maps and then to proportions of burned area by also using the MCD64A1 information for the overlapping period.

The yearly average BA was 3.12 Mkm2 in the time series, with Africa being the region with the largest extension of BA (74.37%). 2011 was the most burned year (4.45 Mkm2) and 1988 the least burned (1.74 Mkm2). There were seasonal fire trends according to the different months; December (0.44 Mkm2) and September (0.38 Mkm2) were the most burned periods. The most burned land cover classes around the world and in Africa were tree cover, broadleaved, deciduous, closed to open (>15%), shrubland, cropland, and rainfed. Temporal trends of FireCCILT10 and MCD64A1 products were found to be similar at the continental scale, but important differences were found at the national scale, particularly in boreal and temperate regions. Trends had a high inter-annual variability in the pre-MODIS (1982–1999) era and were more stable in the MODIS era (2000–2017). The estimated BA was found to be directly related to the quality of the input LTDR data (particularly the number of observations, the intercalibration among satellites, and the orbital decay of the satellites).

The FireCCILT10 dataset is freely accessible at (ESA and Fire_cci project 2019).

2.6. Acknowledgments

This research was funded by the Fire_cci project within the European Space Agency's (ESA) Climate Change Initiative Program.

2.7. References

Alonso-Canas, I., & Chuvieco, E. (2015). Global burned area mapping from ENVISAT-MERIS and MODIS active fire data. Remote Sensing Of Environment, 163, 140-152

Barbosa, P.M., Gregoire, J.-M., & Pereira, J.M.C. (1997). Detection of burned areas in Africa using a multitemporal multithreshold analysis of NOAA AVHRR GAC data. In Earth Surface Remote Sensing (G. Cecchi, E. T. Engman, contiandE. Zilioli, Eds.); 1997; Proceedings SPIE Vol. 3222, SPIE, Bellingham, WA, pp. 67–75. In

Barbosa, P.M., Grégoire, J.M., & Pereira, J.M.C. (1999). An algorithm for extracting burned areas from time series of AVHRR GAC data applied at a continental scale. Remote Sensing Of Environment, 69, 253-263

Belgiu, M., & Drăguţ, L. (2016). Random forest in remote sensing: A review of applications and future directions. ISPRS Journal of Photogrammetry and Remote Sensing, 114, 24-31

Bond, W.J., Woodward, F.I., & Midgley, G.F. (2005). The global distribution of ecosystems in a world without fire. New phytologist, 165, 525-538

Ciais, P., Sabine, C., Bala, G., Bopp, L., Brovkin, V., Canadell, J., Chhabra, A., DeFries, R., Galloway, J., & Heimann, M. (2014). Carbon and other biogeochemical cycles. In T.F. Stocker, D. Qin, G.-K. Plattner, M. Tignor, S.K. Allen, J. Boschung, A. Nauels, Y. Xia, V. Bex, & P.M. Midgley (Eds.), Climate Change 2013: The Physical Science Basis. Contribution of Working Group I to the Fifth Assessment Report of the Intergovernmental Panel on Climate Change (pp. 465-570). Cambridge: Cambridge University Press

Copernicus Programme. (2019). Available online: https://land.copernicus.eu/ (accessed on 01 September 2019).

Chuvieco, E., Englefield, P., Trishchenko, A.P., & Luo, Y. (2008). Generation of long time series of burn area maps of the boreal forest from NOAA–AVHRR composite data. Remote Sensing of Environment, vol. 112, 2381-2396

Chuvieco, E., Lizundia-Loiola, J., Pettinari, M.L., Ramo, R., Padilla, M., Tansey, K., Mouillot, F., Laurent, P., Storm, T., & Heil, A. (2018). Generation and analysis of a new global burned area product based on MODIS 250 m reflectance bands and thermal anomalies. Earth System Science Data, 10, 2015-2031

Chuvieco, E., Martín, M.P., & Palacios, A. (2002). Assessment of different spectral indices in the red-near-infrared spectral domain for burned land discrimination. International Journal of Remote Sensing, 23, 5103-5110

Chuvieco, E., Mouillot, F., van der Werf, G.R., San Miguel, J., Tanasse, M., Koutsias, N., García, M., Yebra, M., Padilla, M., & Gitas, I. (2019). Historical background and current

developments for mapping burned area from satellite Earth observation. Remote Sensing Of Environment, 225, 45-64

Chuvieco, E., Ventura, G., Martín, M.P., & Gomez, I. (2005). Assessment of multitemporal compositing techniques of MODIS and AVHRR images for burned land mapping. Remote Sensing Of Environment, 94, 450 – 462

Dice, L.R. (1945). Measures of the amount of ecologic association between species. Ecology, 26, 297-302

Dillon, G.K., Holden, Z.A., Morgan, P., Crimmins, M.A., Heyerdahl, E.K., & Luce, C.H. (2011). Both topography and climate affected forest and woodland burn severity in two regions of the western US, 1984 to 2006. Ecosphere, 2, 1-33

ESA (2013). "Land Cover CCI: Algorithm Theoretical Basis Document Version 2.". Land_Cover_CCI_ATBDv2_2.3., Louvain, Belgium, 191 pp. Available online: https://www.esa-landcover-cci.org/?q=webfm_send/75 (accessed on 02 September 2019).

ESA & Fire_cci project. (2019). Available online: https://geogra.uah.es/fire_cci/ltdr.php (accessed on 01 September 2019).

ESA. (2019). Available online: https://www.esa-fire-cci.org/ (accessed on 01 September 2019).

García-Lázaro, J., Moreno-Ruiz, J., Riaño, D., & Arbelo, M. (2018). Estimation of burned area in the Northeastern Siberian Boreal Forest from a long-term data record (LTDR) 1982–2015 time series. Remote Sensing, 10, 940

GCOS (2011). Systematic observation requirements for satellite-based products for climate, 2011 update. Geneva, Switzerland: World Meteorological Organization

Giglio, L., Boschetti, L., Roy, D.P., Humber, M.L., & Justice, C.O. (2018). The Collection 6 MODIS burned area mapping algorithm and product. Remote Sensing Of Environment, 217, 72-85

Giglio, L., Randerson, J.T., & Werf, G.R. (2013). Analysis of daily, monthly, and annual burned area using the fourth generation global fire emissions database (GFED4). Journal of Geophysical Research: Biogeosciences, 118, 317-328

Granier, C., Bessagnet, B., Bond, T., D'Angiola, A., van Der Gon, H.D., Frost, G.J., Heil, A., Kaiser, J.W., Kinne, S., & Klimont, Z. (2011). Evolution of anthropogenic and biomass

burning emissions of air pollutants at global and regional scales during the 1980–2010 period. Climatic Change, 109, 163-190

Grégoire, J.M., Tansey, K., & Silva, J.M.N. (2003). The GBA2000 initiative: Developing a global burned area database from SPOT-VEGETATION imagery. International Journal of Remote Sensing, 24, 1369 - 1376

Hantson, S., Arneth, A., Harrison, S.P., Kelley, D.I., Prentice, I.C., Rabin, S.S., Archibald, S., Mouillot, F., Arnold, S.R., & Artaxo, P. (2016). The status and challenge of global fire modelling. Biogeosciences, 13, 3359-3375

Horion, S., Fensholt, R., Tagesson, T., & Ehammer, A. (2014). Using earth observation-based dry season NDVI trends for assessment of changes in tree cover in the Sahel. International Journal of Remote Sensing, 35, 2493-2515

Huete, A.R. (1988). A soil-adjusted vegetation index (SAVI). Remote Sensing Of Environment, 25, 295-309

Kucêra, J., Yasuoka, Y., & Dye, D.G. (2005). Creating a forest fire database for the Far East of Asia using NOAA/AVHRR observation. International Journal of Remote Sensing, 26, 2423-2439

Long, T., Zhang, Z., He, G., Jiao, W., Tang, C., Wu, B., Zhang, X., Wang, G., & Yin, R. (2018). 30m resolution Global Annual Burned Area Mapping based on Landsat images and Google Earth Engine. arXiv preprint arXiv:1805.02579

Martín, M.P., & Chuvieco, E. (1998). Cartografía de grandes incendios forestales en la Península Ibérica a partir de imágenes NOAA-AVHRR. Serie Geográfica, 7, 109-128

McGwire, K.C., Minor, T., & Fenstermaker, L. (2000). Hyperspectral mixture modeling for quantifying sparse vegetation cover in arid environments. Remote Sensing Of Environment, 72, 360-374

Moreno Ruiz, J.A., Riano, D., Arbelo, M., French, N.H., Ustin, S.L., & Whiting, M.L. (2012). Burned area mapping time series in Canada (1984–1999) from NOAA-AVHRR LTDR: A comparison with other remote sensing products and fire perimeters. Remote Sensing Of Environment, 117, 407-414

Mouillot, F., & Field, C.B. (2005). Fire history and the global carbon budget: a 1 degrees x 1 degrees fire history reconstruction for the 20th century. Global Change Biology, 11, 398-420

Mouillot, F., Schultz, M.G., Yue, C., Cadule, P., Tansey, K., Ciais, P., & Chuvieco, E. (2014). Ten years of global burned area products from spaceborne remote sensing—A review: Analysis of user needs and recommendations for future developments. International Journal of Applied Earth Observation and Geoinformation, 26, 64-79

Myneni, R.B., Keeling, C., Tucker, C.J., Asrar, G., & Nemani, R.R. (1997). Increased plant growth in the northern high latitudes from 1981 to 1991. Nature, 386, 698

Canadian Forest Service, 2017. Canadian National Fire Database – Agency Fire Data. Natural Resources Canada, Canadian Forest Service, Northern Forestry Centre, Edmonton, Alberta. Available online: http://cwfis.cfs.nrcan.gc.ca/ha/nfdb (last accessed on 01 September 2019).

NAFI – North Australia & Rangelands Fire Information. (2019). Available online: www.firenorth.org.au/nafi2 (accessed on 01 September 2019).

Padilla, M., Stehman, S.V., Hantson, S., Oliva, P., Alonso-Canas, I., Bradley, A., Tansey, K., Mota, B., Pereira, J.M., & Chuvieco, E. (2015). Comparing the Accuracies of Remote Sensing Global Burned Area Products using Stratified Random Sampling and Estimation. Remote Sensing of Environment 160, 114-121

Padilla, M., Wheeler, J., & Tansey, K. (2018). ESA Climate Change Initiative – Fire_cci. D4.1.1 Product Validation Report (PVR). Available from: http://www.esa-fire-cci.org/documents (accessed on 02 September 2019).

Pedelty, J., Devadiga, S., Masuoka, E., Brown, M., Pinzon, J., Tucker, C., Vermote, E., Prince, S., Nagol, J., Justice, C., Roy, D., Ju, J., Schaaf, C., Liu, J., Privette, J., & Pinheiro, A. (2007). Generating a long-term land data record from the AVHRR and MODIS instruments. In, Geoscience and Remote Sensing Symposium, 2007. IGARSS 2007. IEEE International (pp. 1021-1025): IEEE

Pelletier, C., Valero, S., Inglada, J., Champion, N., & Dedieu, G. (2016). Assessing the robustness of Random Forests to map land cover with high resolution satellite image time series over large areas. Remote Sensing of Environment, 187, 156-168

Pinty, B., & Verstraete, M.M. (1992). GEMI: a non-linear index to monitor global vegetation from satellites. Vegetatio, 101, 15-20

Power, M.J., Marlon, J.R., Bartlein, P.J., & Harrison, S.P. (2010). Fire history and the Global Charcoal Database: A new tool for hypothesis testing and data exploration. Palaeogeography, Palaeoclimatology, Palaeoecology, 291, 52-59

Ramo, R., & Chuvieco, E. (2017). Developing a Random Forest Algorithm for MODIS Global Burned Area Classification. Remote Sensing, 9, 1193

Ramo, R., García, M., Rodríguez, D., & Chuvieco, E. (2018). A data mining approach for global burned area mapping. International Journal of Applied Earth Observation and Geoinformation, 73, 39-51

Riaño, D., Ruiz, J.A.M., Isidoro, D., & Ustin, S.L. (2007). Global spatial patterns and temporal trends of burned area between 1981 and 2000 using NOAA-NASA Pathfinder. Global Change Biology, 13, 40-50, doi: 10.1111/j.1365-2486.2006.01268.

Rodriguez-Galiano, V.F., Ghimire, B., Rogan, J., Chica-Olmo, M., & Rigol-Sanchez, J.P. (2012). An assessment of the effectiveness of a random forest classifier for land-cover classification. ISPRS Journal of Photogrammetry and Remote Sensing, 67, 93-104

Rouse, J.W., Haas, R.W., Schell, J.A., Deering, D.H., & Harlan, J.C. (1974). Monitoring the vernal advancement and retrogradation (Greenwave effect) of natural vegetation. In. Greenbelt, MD. USA: NASA/GSFC

Roy, D.P., Boschetti, L., & Justice, C.O. (2008). The collection 5 MODIS burned area product — Global evaluation by comparison with the MODIS active fire product. Remote Sensing Of Environment, 112, 3690-3707

Simon, M., Plummer, S., Fierens, F., Hoelzemann, J.J., & Arino, O. (2004). Burnt area detection at global scale using ATSR-2: The GLOBSCAR products and their qualification. Journal of Geophysical Research - Atmospheres, 109, D14S02, doi:10.1029/2002JD003622

FRAP – California Department of Forestry and Fire Protection's Fire and Resource Assessment Program. (2019). Available online: frap.fire.ca.gov (accessed on 01 September 2019).

Sukhinin, A.I., French, N.H.F., Kasischke, E.S., Hewson, J.H., Soja, A.J., Csiszar, I.A., Hyer, E.J., Loboda, T., Conrad, S.G., Romasko, V.I., Pavlichenko, E.A., Miskiv, S.I., & Slinkina, O.A. (2004). AVHRR-based mapping of fires in Russia: New products for fire management and carbon cycle studies. Remote Sensing Of Environment, 93, 546-564

Tansey, K., Grégoire, J.M., Defourny, P., Leigh, R., Peckel, J.F., Bogaert, E.V., & Bartholome, J.E. (2008). A new, global, multi-annual (2000–2007) burnt area product at 1 km resolution. Geophysical Research Letters, 35, L01401, doi:10.1029/2007GL03156

Tian, F., Fensholt, R., Verbesselt, J., Grogan, K., Horion, S., & Wang, Y. (2015). Evaluating temporal consistency of long-term global NDVI datasets for trend analysis. Remote Sensing Of Environment, 163, 326-340

Trishchenko, A.P., Fedosejevs, G., Li, Z., & Cihlar, J. (2002). Trends and uncertainties in thermal calibration of AVHRR radiometers onboard NOAA-9 to NOAA-16. Journal of Geophysical Research: Atmospheres, 107, ACL 17-11-ACL 17-13

Urbanski, S.P., Hao, W.M., & Baker, S. (2008). Chemical composition of wildland fire emissions. Developments in Environmental Science, 8, 79-107

Van Der Werf, G.R., Randerson, J.T., Giglio, L., Van Leeuwen, T.T., Chen, Y., Rogers, B.M., Mu, M., Van Marle, M.J., Morton, D.C., Collatz, G.J., Yokelson, R.J., & Kasibhatla, P.S. (2017). Global fire emissions estimates during 1997-2016. Earth System Science Data, 9, 697–720.

Ward, D., Kloster, S., Mahowald, N., Rogers, B., Randerson, J., & Hess, P. (2012). The changing radiative forcing of fires: global model estimates for past, present and future. Atmospheric Chemistry and Physics, 12

Capítulo 3

DEVELOPMENT OF A CONSISTENT GLOBAL LONG-TERM BURNED AREA PRODUCT (1982-2018) BASED ON AVHRR-LTDR DATA

This work was published in the International Journal of Applied Earth Observation and Geoinformation (103, 102473) in 2021.

Abstract

This paper presents the generation of a global long-term Burned Area (BA) product based on Advanced Very High Resolution Radiometer (AVHRR) images. The BA product was derived from the Land Long Term Data Record (LTDR), which provides a continuous dataset of geometrically and radiometrically corrected AVHRR images at 0.05° resolution (≈5km). The BA algorithm improves a Beta version of this dataset (named FireCCILT10) previously released. The new version incorporates an enhanced Random Forest (RF) classification process based on two models, one using a global sample and another one using only Boreal regions. Solar zenith angle (SZA) corrections were introduced to mitigate the impact of satellite orbital drift. Binary classifications were obtained applying probability thresholds, and BA proportions were assigned to each burned pixel. The final product includes the date of detection at 0.05° resolution and the total burned area at 0.05° and 0.25° resolution, both covering the period from 1982 to 2018 (excluding 1994). The resulting product, called FireCCILT11, estimated that 165.26 Mkm2 were globally burned between 1982 and 2018, with an annual average of 4.59 Mkm2. The largest BA was found in 2011 with 5.18 Mkm2 and the lowest was observed in 1991 with 4.09 Mkm2. The month with the highest mean BA was August, with 0.63 Mkm2, and the one with the lowest was March with 0.15 Mkm2. Africa included 66% of total BA. Inter-comparison showed high correlation values with MODIS BA products for annual BA of the common years ($r > 0.6$, %MAE < 14%). Comparison with national fire statistics of Australia, Canada and Alaska showed also high correlation values ($r > 0.8$, %MAE < 42%).

3.1. Introduction

Fire disturbance was identified by the Global Climate Observing System (GCOS) programme as an Essential Climate Variable (ECV) because of the impacts of burnings in atmospheric composition and the carbon cycle (Yue et al. 2015). To answer GCOS' needs, the European Space Agency (ESA) created in 2010 the Climate Change Initiative Programme (CCI), which included then 10 ECVs and now 21 (https://climate.esa.int/en/, last accessed July 2021). The Fire Disturbance project was part of the initial programme and therefore has been active for more than 10 years. Within this project, several global BA products from different sensors have been generated and released, including inputs from Envisat-MERIS (FireCCI41: Alonso-Canas and Chuvieco 2015), MODIS (FireCCI51: Lizundia-Loiola et al. 2020) and AVHRR (FireCCILT10: Otón et al. 2019) data. The National Aeronautics and Space Administration (NASA) have also developed BA products based on MODIS (MCD64A1: Giglio et al. 2018), in addition to those oriented towards detecting active fires. Currently, the FireCCI51 and MCD64A1, based on MODIS 250m and 500 m

bands, respectively, are the most accurate global products, widely used in different modelling studies (Chuvieco et al. 2019).

One of the recommendations of the GCOS programme was to extend the BA datasets backwards to the 80s (GCOS 2016), as all existing global products were based on sensors that were launched at the end of the 1990s or early 2000s. This requirement, also indicated by many climate modellers (Mouillot et al. 2014; Chuvieco et al. 2019), implies using the historical catalogue of the AVHRR sensor, on board the National Oceanic and Atmospheric Administration (NOAA) satellites since 1979. However, this sensor presents many limitations for generating BA datasets, as it has a coarse resolution and it is affected by changes in sensor versions, orbital drift of the satellite, acquisition problems, random noises, and location errors (McGregor and Gorman 1994; Weber and Wunderle 2019). In spite of these problems, several BA products have been generated from AVHRR images, mostly for selected regional areas (Chuvieco et al. 2008; Dubinin et al. 2010; Eva and Lambin 1998; Kucêra et al. 2005; Plank and Martinis 2018; Yates et al. 2009). These studies were based on the higher resolution version of AVHRR data (approximately 1.21 km2 at nadir). This native resolution was not archived globally until 1992. Previous acquisitions were only archived at a degraded resolution of 4x4 km, preventing the use of higher resolution AVHRR data for generating global BA products. For this reason, previous studies created global BA products only from coarser resolution AVHRR data, such as the Pathfinder AVHRR Land (PAL) dataset (Carmona-Moreno et al. 2005; Riaño et al. 2007a) with 8x8 km resolution. After releasing the PAL data, an advanced AVHRR global dataset was developed by NASA at 0.05-degree resolution (approx. 5x5 km). This product was named the Land Long Term Data Record or LTDR (Pedelty et al. 2007). LTDR data were used to generate regional BA datasets, mainly in Alaska (Moreno-Ruiz et al. 2019) and Siberia (García-Lázaro et al. 2018). The first global BA product based on LTDR and covering the full AVHRR time series was released in 2019 as a beta version within the FireCCI project (FireCCILT10, Otón et al. 2019). This prototype product included some artefacts caused by sensor problems and the impact of the orbital drift, which modified the solar zenith angle (Giglio and Roy 2020). Furthermore, the FireCCILT10 presented an underestimation of BA in boreal regions, as this Beta version was based on global models that were highly influenced by the large extent of tropical fires.

Taking into account the problems detected on the FireCCILT10 product, we have modified several processes, and used these improvements to generate a new version of this product that could provide more accurate and stable trends. In this paper, we present the new version of the algorithm and the resulting product (named FireCCILT11). We first introduce the general approach of the BA LTDR algorithm and changes made from the beta version. Then we analyse the resulting product and compare the spatial and temporal trends with existing global and regional BA datasets.

3.2. Methods

3.2.1. Algorithm basis

The methodology to obtain a BA product from LTDR data was based on several steps, as illustrated in Figure 3.1. Inputs (Section 3.2.2) were the AVHRR-LTDR data (version 5) at 0.05° resolution (≈5 km at the Equator); annual Land Cover (LC) data since 1992 (Copernicus 2019; ESA 2013); and FireCCI51 BA data (Lizundia-Loiola et al. 2020). The latter was used to train the RF (Breiman 2001) models. Temporal composites, spectral indices, and the cloud mask (Section 3.2.3.1 and Section 3.2.3.2) were calculated from the original LTDR data to obtain a synthetic index (Section 3.2.3.3) adapted to the burned signal. Two types of RF models were developed (Section 3.2.4): global and boreal, as a poor estimation of BA in boreal regions was observed in the precursor product. Henceforth, the processes were repeated for each type of model. Three sets of criteria to obtain detection thresholds were used (Section 3.2.5.1). Then a BA analysis was used to obtain proportions of BA for each detected pixel (Section 3.2.5.2). Results from the boreal model replaced those of the global model in boreal regions to generate the final product (named FireCCILT11). This product covers the period from 1982 to 2018, excluding 1994 as this year had many missing dates in the LTDR dataset. Due to the poor quality of the LTDR data in 2019 and 2020, the processing did not include those years.

The main novelties of this BA algorithm from the previous one (described in Otón and Chuvieco 2018; Otón et al. 2019) are summarized in Table 3.1, and include the changes introduced in the RF models and detection thresholds, the improvement of the cloud screening, the update of the land cover product (which in this version changes annually), and the target product for training of the model, which is now ESA FireCCI51 instead of the NASA MCD64A1.

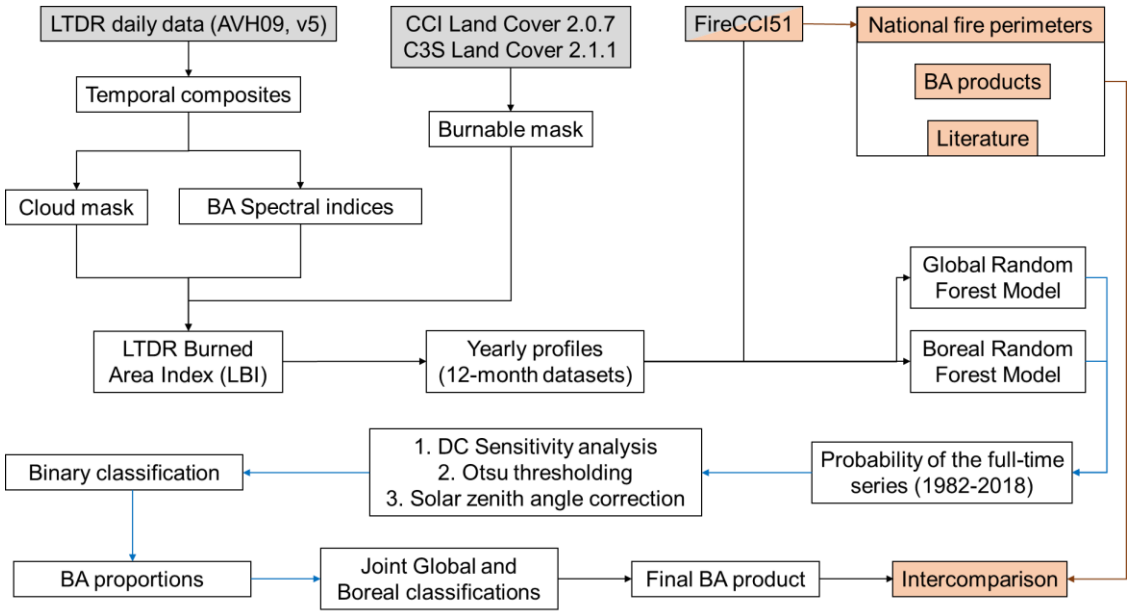

Figure 3.1. General scheme of the FireCCILT11 algorithm. Input data are shown in grey. Orange boxes and arrows indicate the data that have been used for inter-comparison. Black arrows mean that the process was run only once (common steps), while blue arrows represent processes that were run for each RF model.

Table 3.1. Changes in the BA algorithm from the FireCCILT10 Beta version.

	FireCCILT10	**FireCCILT11**
Input data		
Training data	MCD64A1 C6 product	FireCCI51 product
Land cover	A single LC in the time series (year 2000)	Annual (from 1992)
Land Cover information	ESA CCI-LC v1.6.1 product	ESA CCI-LC v2.0.7 and C3S-LC v2.1.1 products.
Cloud mask	Red and NIR values > 90%	Criteria to filter clouds (Section 3.2.3.2)
Temporal sequence		
Yearly profiles	All months within a single year	Regressive and progressive months
Random Forest models		
# samples in each tree	20k	10M
Years to train	8 years	18 years
Models	Global	Global and boreal

Table continued on next page.

Table 3.1 – continued from previous page.

	FireCCILT10	FireCCILT11
Thresholding methods		
Monthly thresholding	Global for the time series	Regional for each image
Adaptive thresholds	Dice Coefficient	Otsu method and Dice Coefficient
SZA correction	Not applied	Regional for each image (1982-2000)
BA proportions		
Monthly BA assignments	Global	Regional
Cases (Figure 3.3)	A and B	The four cases
Products		
Production years	1982-2017	1982-2018

3.2.2. Input data

The LTDR product is a long-term NASA dataset of AVHRR observations, based on the afternoon (ascending) passes of the NOAA polar orbiting satellites. The time series includes 40 years of observations collected by NOAA-7, 9, 11, 14, 16, 18, and 19. The original data were acquired by the AVHRR 2/3 sensors and stored on board at a reduced resolution, named Global Area Coverage (GAC, 4 km versus the original 1.1 km). The LTDR dataset includes daily and global GAC observations, resampled to 0.05° (≈5 km), from 1981 to date. The time series is not fully complete and presents some observational gaps. The most important two were found in 1994 and from 2018 onwards. In the first case, important gaps and noise were found in the images from March to September and empty data from September to December, due to NOAA-11 orbital degradation. From 2018 onwards the data quality has been degrading due to important gaps in the images and the presence of artefacts. Consequently, 1994, 2019 and 2020 were not used for the generation of the BA product, following also other author's suggestions (Hansen et al. 2018; Tian et al. 2015).

We used the Surface Reflectance Product of the LTDR dataset, named AVH09. It includes ten bands: reflectance for channel 1 (R1, red, 0.58–0.68 μm) and channel 2 (R2, near infrared or NIR, 0.725–1.1 μm), medium infrared reflectance and brightness temperature for channel 3 (R3 and T3, 3.55–3.93 μm), and brightness temperature for channel 4 (T4, 10.3–11.3 μm) and channel 5 (T5, 11.5–12.5 μm). In addition, the product includes view zenith angle, SZA, relative azimuth, and a quality assessment layer (QA). Despite the corrections applied by the Pathfinder program (El Saleous et al. 2000; Villaescusa-Nadal et al. 2019), some inconsistencies were observed in the visible

channels due to degradation in the sensors and the change in the AVHRR sensor from 1999 to 2000 (Beck et al. 2011; Otón et al. 2019). The reconfiguration of Channel 3 made this band inconsistent through the temporal series (Otón et al. 2019). Furthermore, the degradation of the sensors implied severe orbital drift, which created relevant problems, particularly at high SZA (Stengel et al. 2020). Therefore, the sensor degradation impacts about ≈5-10% the relative accuracy of the visible channels (Los et al. 1994). Moreover, high latitudes presented gaps and low quality observations in winter in both hemispheres (Otón et al. 2019) because the satellites cover those latitudes at night (Giglio and Roy 2020).

The ESA CCI Land Cover v2.0.7 product (CCI-LC, ESA 2013) and the Copernicus Climate Change Service (C3S) Global Land Cover v2.1.1 (C3S-LC, Copernicus 2019) products provide global and annual LC information at 300m spatial resolution. The CCI-LC product is available from 1992 to 2015 (https://climate.esa.int/en/projects/land-cover/, last accessed on July 2021), while C3S-LC offers LC information from 2016 to 2019. This last product is the continuation of the CCI-LC product and, hence, it is fully consistent with its predecessor (https://cds.climate.copernicus.eu/, last accessed on July 2021). We used the LC product to generate a burnable mask (Otón et al. 2019) to optimize the algorithm and avoid potential commission errors. For the period before 1992, the LC of the year 1992 was used.

To train the LTDR BA algorithm, we used the FireCCI51 dataset to keep consistency with other BA products of the CCI programme. This dataset was generated from the MODIS sensor at 250m resolution, using NIR reflectance and active fires (Lizundia-Loiola et al. 2020). The BA product is freely accessible and provides global and monthly BA data at 250 m and 0.25° resolution (https://climate.esa.int/en/projects/fire/, last accessed on July 2021). It has been validated using a global statistical design sample, showing similar accuracy to other global BA products (commission error (Ce) = 54.4%, omission error (Oe) =67.1%), but with a higher sensitivity detecting small burned patches (Lizundia-Loiola et al. 2020) and boreal fires (Moreno-Ruiz et al. 2020).

3.2.3. Pre-processing of LTDR data

3.2.3.1. Compositing

Composite techniques have been previously used by several authors to correct acquisition problems of daily images (Chuvieco et al. 2018; Lizundia-Loiola et al. 2020). We created monthly composites using the maximum temperature criterion, which has been previously used for BA classifications (Cihlar et al. 1994; Chuvieco et al. 2005; Roy 1997).

3.2.3.2. Cloud masking

For the development of BA products it is essential to provide cloud-free images to the algorithm (Giglio et al. 2018; Lizundia-Loiola et al. 2020). Since the standard quality flags of the LTDR product (AVH09 QA) were found not sufficiently accurate to detect cloudy pixels (Otón et al. 2019), a more refined cloud mask was generated for the composite using the criteria shown in Table 3.2.

Table 3.2. Criteria to filter clouds in the AVH09 images. If one of the conditions is met, the pixel was filtered.

Criteria	Description	Reference
Channel 1 >= 40% reflectance	delete low clouds and fire smoke	Stroppiana et al. (2002)
0.9 < Albedo < 1.1 Where: $Albedo = \frac{\text{Channel 1}}{\text{Channel 2}}$	eliminate reflectance ratio clouds	James and Kalluri (1994)
Channel 4 <= 249K	delete thermal gross clouds, high and cold clouds	James and Kalluri (1994)
Channel 5 <= 273K	cloud screening	Tucker et al. (2005)

3.2.3.3. LTDR Burned Index (LBI)

The classification of burned pixels was first tested with a wide variety of combinations of input channels and derived bands. Variable selection was performed in a statistical analysis described in the Beta version (Otón et al. 2019). The variables selected were different spectral bands and indices previously used to discriminate BA, which were included in a single spectral index to combine and enhance their sensitivity to detect BA. This index, named LTDR burned index (LBI), was generated using a linear transformation of different bands and spectral indices. The formulation of this index is:

$$LBI = z(T5) - z(T5\_diff) - z(Red) + z(Red\_diff) - z(NIR) + z(NIR\_diff) + z(GEMI) + z(BAI) + z(BAI_{t+1}) \quad (3.1)$$

(please note that the original formula of Otón et al. (2019) had an error that was later corrected: Otón et al. (2020)).

The LBI uses the temperature of channel 5 (T5), reflectance of the red (Red) and infrared channels (NIR), the Global Environmental Monitoring Index (GEMI) and the Burned Area index (BAI). GEMI (Pinty and Verstraete 1992) was defined as:

$$\mathrm{GEMI} = \eta \cdot (1 - 0{,}25 \cdot \eta) - \left(\frac{\rho_{RED} - 0{,}125}{1 - \rho_{RED}}\right) \tag{3.2}$$

$$\eta = \frac{(2 \cdot (\rho_{NIR}{}^2 - \rho_{RED}{}^2) + 1{,}5 \cdot \rho_{NIR} + 0{,}5 \cdot \rho_{RED})}{\rho_{NIR} + \rho_{RED} + 0{,}5} \tag{3.3}$$

While the BAI (Chuvieco et al. 2002) was computed as:

$$\mathrm{BAI} = \frac{1}{(\rho c_{RED} - \rho_{RED})^2 + (\rho c_{NIR} - \rho_{NIR})^2} \tag{3.4}$$

Where ρNIR and ρRED are the reflectance values of the NIR and Red channels, respectively, and ρcNIR and ρcRED are the convergence values for burned vegetation (defined for AVHRR by the authors of the index as 0.06 and 0.1, respectively). What in the formulas is called "diff" represents the difference between the composite of the month being analysed (t) and the composite of the previous month (t-1). Thus, t+1 is the composite of the following month.

LBI tried to maximize the spectral separation between burned and unburned pixels, facilitating the classification process. The basis for selecting the components of the LBI were their use in previous BA studies and the divergence values observed for training data acquired in 2008. In addition, the LBI was found less sensitive to artefacts and orbital problems than the original bands.

To increase the consistency of the temporal series, all variables were normalized using z-scores:

$$z = \frac{X - \mu}{\sigma} \tag{3.5}$$

where μ and σ are the mean and the standard deviations of the pixel values of each monthly composite and X is the value of the pixel whose LBI is being calculated. LBI was computed for each monthly composite, and the classification models were derived from several composites, including the target month and a few months before and after (see 3.2.4), to include in the BA discrimination the temporal variation of the BA signal.

3.2.4. Burned area detection models

Random Forest is a classification algorithm developed by Breiman (2001) and widely used in classification of satellite data, particularly for land cover studies (Rodriguez-Galiano et al. 2012), but also in BA detection (Ramo and Chuvieco 2017). FireCCI51 (aggregated to 0.05° resolution) was used to train the RF models for the common observation period (2001-2018, 18 years). Burned cells were considered as those that included at least one FireCCI51 pixel burned. The training of the RF model was done with 75% of the FireCCI51 database leaving the remaining 25% for validation. RF parameters were redefined and run in Scikit-learn (Pedregosa et al. 2011). We set the number of trees to six hundred for its good precision-time balance. The maximum depth of the tree is expanded with all its leaves since pruning it does not prevent possible overtraining (Rodriguez-Galiano et al. 2012). Each tree was trained with ten million samples, which were selected randomly. We assigned an extra weight of 10% to the burn class because our database was unbalanced due to the sporadic nature of fire events (Otón et al. 2019; Ramo et al. 2018). The accuracy of the models was obtained using the Out of Bag (OOB) error to learn the training quality (Bylander 2002), and R2 to learn the fit of the model with the validation data. The RF outputs were probabilities of burn.

Even though the RF classifiers were well adapted to different local conditions, we decided to run a dedicated model for boreal forests, whose BA was poorly estimated in the beta version of the LTDR BA product. This was partly caused by the differences between Boreal and Tropical fires, and the larger impact of the latter in generating global models, as most worldwide burned area occurs in Tropical regions (Dwyer et al. 2000; Melchiorre and Boschetti 2018).

Therefore, two types of monthly databases (Figure 3.2) were developed to train global and boreal monthly RF models. In the temporal aggregation, global databases contained twelve months of LBI, while for boreal databases the period of March-October was used instead, as the probability of having Boreal fires in winter is very low (Beck et al. 2011; Kucêra et al. 2005). These monthly databases were generated using five or three months previous to the burned one (auto-regressive months, Riaño et al. 2007b), and the six or four months next to the burned one (auto-progressive months) depending on the type of model (global or boreal, respectively).

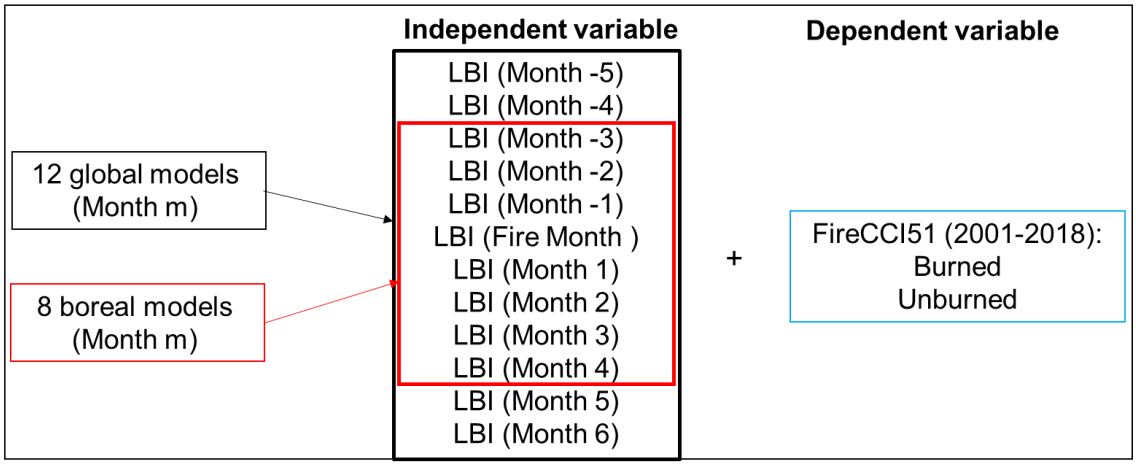

Figure 3.2. Monthly composites used to create the RF models. Monthly models were created using LBI values from several months before and after the target period. For instance, the global RF model of August had as independent variables the LBI of August, LBI of five months before August (that is, March to July) and LBI of six successive months (September to February). The dependent variable was the target BA (FireCCI51) of each target month.

3.2.5. Post-processing of model probabilities

3.2.5.1. Binary classifications and Solar zenith angle correction

Adaptive thresholds are common in algorithms to deal with different vegetation covers, in order to adapt to a diversity of conditions instead of applying only one threshold (Alonso-Canas and Chuvieco 2015; Chuvieco et al. 2018; Lizundia-Loiola et al. 2020; Plank and Martinis 2018). RF probabilities allow defining a cut-off threshold in order to find a correct point where the classification's Oe and Ce are balanced. For this reason, an adaptive, automatic and regional threshold was developed for each of the continental regions defined by Giglio et al. (2013) (available online: http://www.globalfiredata.org/data.html, last accessed on July 2021) and for each of the probability images. Thresholds were adapted using a combination of the Otsu method (Otsu 1979) and maximization of the Dice Coefficient (DC, Dice 1945). DC summarizes the omission and commission error of the BA class in a single index, indicating the conditional probability that a burned pixel in the reference data will be detected as burned by the classification. This accuracy metric has been used in several BA validation papers (Padilla et al. 2017; Padilla et al. 2015).

$$Dice\ Coefficient = \frac{2 \cdot True\ Positives}{2 \cdot True\ Positives + False\ Positives + False\ Negatives} \quad (3.6)$$

First, a sensitivity analysis was performed using iterating probability thresholds from 0 to 1 (steps of 0.01) until the threshold that provided the highest possible DC value was

found by continental region. The FireCCI51 was used as reference dataset, considering any percentage of BA > 0 to be a burned pixel. A median value (Med) per month was calculated using all the thresholds of the 2001-2018 time-series (with existing FireCCI51 data) to obtain the Med (ThresholdDC). This meant that these values were only suitable for the MODIS era, but might not be well adjusted to the previous years. Then, the Otsu method was used to obtain a second threshold fitted to each image, maintaining their variability. Otsu aims to get a threshold that maximizes the separability between two classes, while minimizing the internal one, using their histograms. Again, a median per month and continental region was calculated to obtain Med (ThresholdOtsu) for the period 2001-2018.

Next, a relative constant was calculated in the 2001-2018 period per month and continental region, to determine the Otsu correction threshold for pre-MODIS years (1982-2000), in which no training data was available:

$$Relative\ constant\ _{m,CR} = \frac{Med(Threshold_{DC})_{m,CR}}{Med(Threshold_{Otsu})_{m,CR}} \tag{3.7}$$

where m is the month, and CR is each of the continental regions. In this way, the corrected Otsu threshold has values close to the optimal DC threshold, but adapted to each image and region.

Afterwards, the detection thresholds were adapted to the variations in SZA, which was observed to be associated to the BA detection in the beta version of our product (Giglio and Roy 2020). The orbital drift of the NOAA satellites implies a delay in the satellite overpass, affecting local Sun conditions during the satellite life (Carmona-Moreno et al. 2005; Devasthale et al. 2012; Ji and Brown 2017). To mitigate this effect in the most affected period (1982-2000), we created a relative parameter to include in the corrected Otsu threshold.

$$SZAcorrection_{m,CR} = \frac{\overline{SZA}_{m,CR}}{Min\ (SZA_{m,CR})} \tag{3.8}$$

Finally, the corrected Otsu threshold was obtained with the formula:

$$\begin{aligned} Corrected\ Threshold_{Otsu,m,CR} \\ = Threshold_{Otsu,m,CR} \\ * (Relative\ constant\ _{m,CR})^{SZAcorrection_{m,CR}} \end{aligned} \tag{3.9}$$

This formula was calculated for each probability image to obtain the optimum threshold to create a binary image of burned and unburned pixels, and it was applied to both model results (global and boreal). Despite those corrections, the lack of data and the decrease of good observations that occurred at the end of the life of the satellites could not be corrected, and they remained as a limitation of the input data.

3.2.5.2. Burned area proportion assignment

Each burned pixel derived from the binary result of the detection thresholds (Section 3.2.5.1) was assigned an estimated proportion of area burned. We aimed to provide a similar total BA between the LTDR-based binary classification and the FireCCI51 products for the overlapping period, and then extrapolate this relation backwards. For each month in the FireCCI51 period, this correction was done at grid-cell level (0.25°, corresponding to 5x5 0.05°-resolution pixels) (Figure 3.3), so that the influence of the neighbour pixels was taken into account (Lizundia-Loiola et al. 2020). Four different cases were found (A to D in Figure 3.3). Case A occurred when both FireCCI51 and the binary classification detected BA. In that case, the BA proportion was obtained by dividing the total BA detected by FireCCI51 during the target month by the total BA obtained in the binary RF classification (2001-2018). Where FireCCI51 detected BA but the binary classification did not (case B) in the common time series, the area of one pixel was considered as the total BA in the binary classification. Where cells were never detected as BA in the FireCCI51 period but the binary classification detected some burned pixels (case C), or where FireCCI51 and the binary classification did not detect BA in that month during the 2001-2018 time series (case D), the median of the BA proportions (cases A and B) of each continental region was used. A limitation of this method was a possible border effect, which could occur because the algorithm was adjusted per continental regions.

The last condition was that a pixel could not be fully burned in a temporal window of six consecutive months. The final FireCCILT11 product was created substituting the global results in the boreal region with the results of the boreal model.

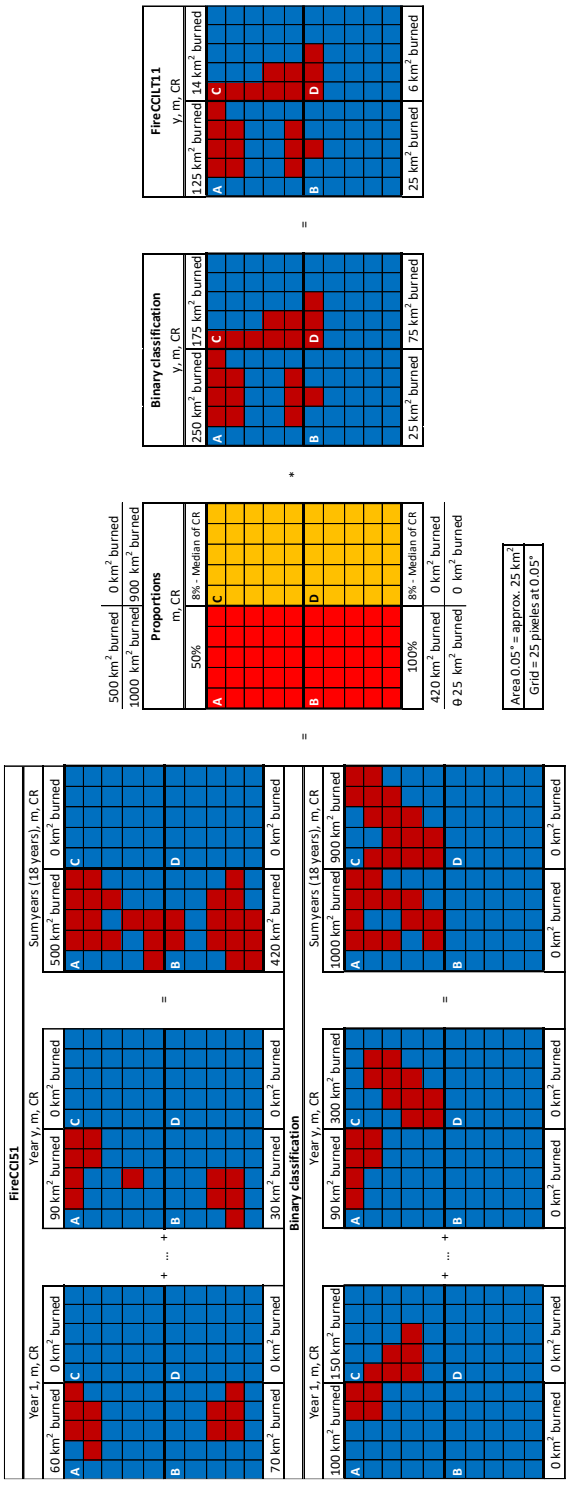

Figure 3.3. Calculation of BA proportions per grid cells (0.25°). This example shows the four classification possibilities (A-D), where y is the year, m is the month, and CR is each of the continental regions. The figure shows in the upper left the sum of FireCCI51 BA of the different years (2001-2018) and in the lower left the sum of the Binary classification BA (obtained from the RF algorithm, and deemed fully burned). In the centre, the BA proportions allocated to each grid cell is shown, which multiplied by the BA in each Binary classification image in the 1982-2018 time series allows to obtain the total burned area in each pixel.

3.2.6. Inter-comparison

The usual strategies used for validating global BA products rely on Landsat or Sentinel-2 images (Boschetti et al. 2019; Chuvieco et al. 2019). However, the resolution gap between these data (20-30 m) and the LTDR product (5 km) makes this type of validations inconvenient. Thus, the spatial and temporal consistency of the product was checked with existing global BA products and official fire perimeters. In the former case, we compared the BA of the FireCCILT11 product with the BA estimated by the FireCCI51, which was used to train our algorithm. From this comparison, commission error and omission errors and the Dice Coefficient were calculated, assuming FireCCI51 was the reference. We also included comparisons with the NASA MCD64A1 product (Giglio et al. 2018), widely used in the modelling community, and the precursor LTDR BA product, the FireCCILT10 dataset.

We also compared our results with national fire perimeters, particularly where BA perimeters were available before the MODIS era (<2000). For Boreal regions we used Canadian and Alaskan fire perimeters, collected from the Canadian National Fire Database (CNFDB, Canadian Forest Service 2017) from 1980 to 2019 and the Alaska fire history perimeters (Available online: https://fire.ak.blm.gov/predsvcs/maps.php, last accessed on July 2021) from 1940 to 2020, respectively. For Tropical regions, we did not find reference perimeters before 2000 and used instead the North Australia and rangelands fire information (NAFI, Available online: https://firenorth.org.au/nafi3/, last accessed on July 2021), from 2000 to 2018. We also used for inter-comparison some regional studies that mapped burned areas before 2000 using AVHRR data, covering the Republic of Kalmykia in southern Russia (Dubinin et al. 2010) and the Siberian Boreal Forest (García-Lázaro et al. 2018).

The comparison was performed using the Pearson correlation (r) and the Percentage of Mean Absolute Error (%MAE). %MAE corresponds to the percentage of the Mean Absolute Error (MAE) with respect to the BA mean of the reference products during the existing time series.

3.3. Results

The performance of the RF models was high, presenting an OOB error < 0.03 in the global models, and an OOB error < 0.006 in the boreal models. Furthermore, the RF models were validated with 25% of the database, offering an accuracy of $R2 > 0.97$ in the global models, and $R2 > 0.99$ in the boreal models.

3.3.1. Spatial and temporal trends

The algorithm was run with the available time series of LTDR data (1982-2018, except 1994) to create the FireCCILT11 dataset. This dataset is comprised by two products: monthly pixel files at 0.05° resolution, including date of detection according to the composite, confidence level, BA and number of observations, and monthly grid files at 0.25° resolution, including for each cell total BA, standard error, fraction of burnable area and fraction of observed area.

Figure 3.4 shows the spatial distribution of total BA for two years. The spatial patterns of BA are consistent with other global BA products, with higher occurrence in the Tropical dry belts, particularly in Africa, Northern Australia, Colombia-Venezuela, the Brazilian Cerrado, Cambodia, Eastern India, and Central Asia. As in other global BA products, the FireCCILT11 product estimated that Africa was the most extensively burned continent (with 66% of global BA). Spatial trends were similar in the time series, including periods when the LTDR input was obtained from the AVHRR2 sensor (before 2000) and from the AVHRR3 (after 2000), as observed in the examples of Figure 3.4.

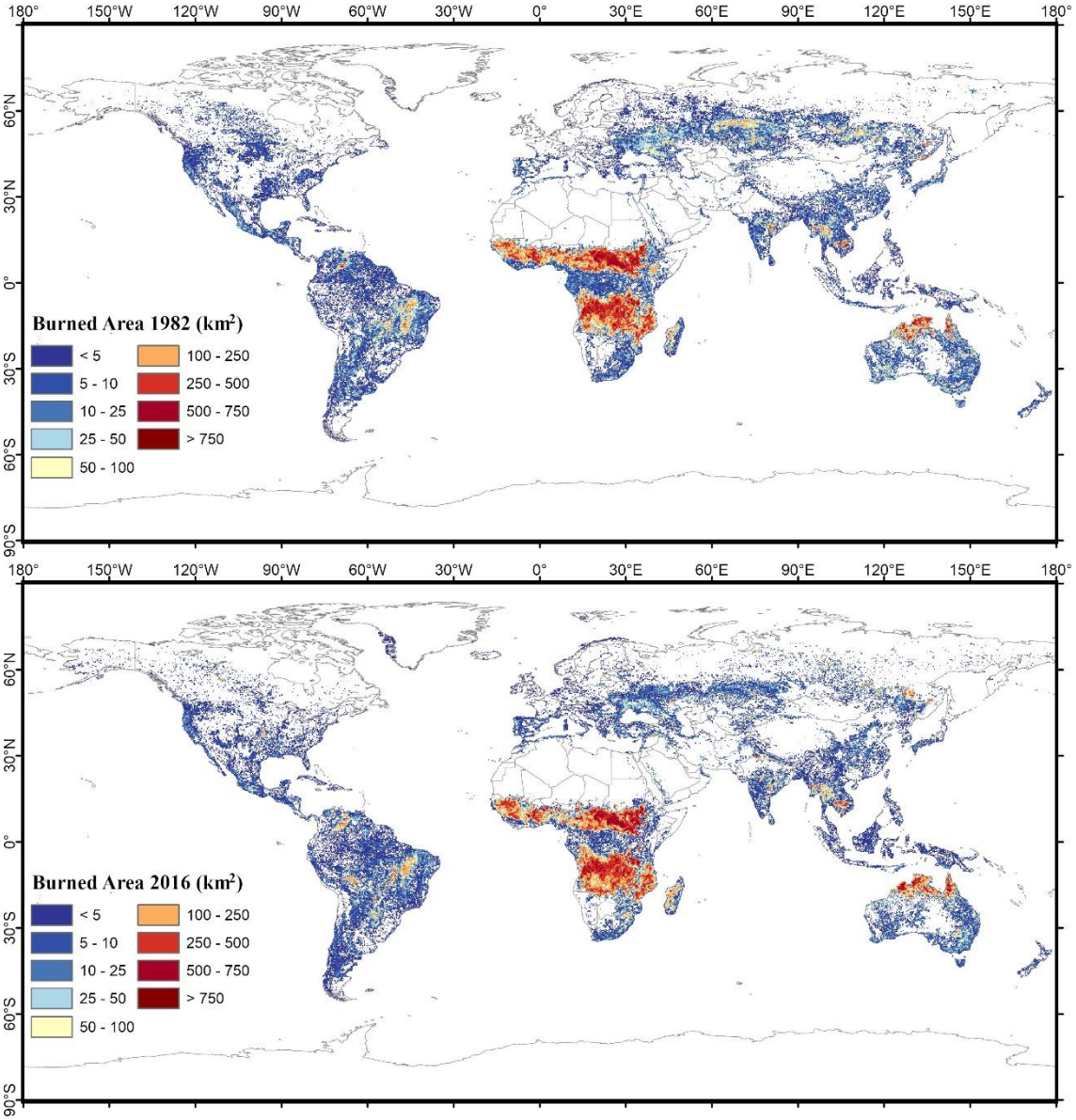

Figure 3.4. Annual FireCCILT11 BA (at 0.25° resolution) for two different periods. 1982 belongs to the 1982-2000 period with the AVHRR2 sensor and 2016 belongs to the 2001-2018 period with the AVHRR3 sensor.

The annual BA average estimated by the FireCCILT11 product was 4.59 Mkm2, with an accumulated BA of 165.26 Mkm2 for the period 1982-2018 (excluding 1994), of which 79.08 Mkm2 were from 1982-2000 and 86.18 Mkm2 from 2001-2018. The maximum annual BA was observed in 2011, with 5.18 Mkm2, and the least-burned year was 1991 with 4.09 Mkm2. August was the month with the largest BA, with an average of 0.63 Mkm2, while March showed the lowest value with 0.15 Mkm2.

3.3.2. Comparison with global BA products

Figure 3.5 shows the yearly evolution of BA in the FireCCILT11 product, comparing it with the beta version of the product and existing MODIS-based BA datasets. For the common period, the annual trends of FireCCILT11 are similar to the two MODIS products (FireCCI51 and MCD64A1), with high correlation values (r = 0.87 with MCD64A1 and r = 0.6 with FireCCI51) and low %MAE: 14% with MCD64A1 and 6% with FireCCI51. FireCCILT11 has a lower correlation with FireCCI51 but it also has a lower %MAE compared to MCD64A1, which means that even though the FireCCILT11 values are closer to FireCCI51, the trend is more similar to MCD64A1. When this analysis was repeated using monthly data, the values showed higher correlations, with r values of 0.89 (%MAE = 21%) compared to MCD64A1 and 0.95 (%MAE = 10%) with FireCCI51. At this level of disaggregation, FireCCILT11 is more similar to FireCCI51. The DC in the common time series of FireCCI51-FireCCILT11 is more than 0.63 (Oe=0.21 and Ce=0.47) and the DC of MCD64A1-FireCCILT11 is 0.44 (Oe=0.39 and Ce=0.66). As average, FireCCILT11 detected 3.5% more BA than FireCCI51 and ≈ 14% more BA than MCD64A1 for the common years. FireCCILT11 estimated more BA in each year compared to MCD64A1, and compared to FireCCI51 detected more BA in most years, except 2004, 2005, 2007 and 2008. The year with the largest difference between FireCCILT11 and FireCCI51 was 2001 and FireCCILT11-MCD64A1 was 2013. The FireCCILT11 values were closer to FireCCI51 than MCD64A1, although the FireCCILT11 trend was softer than FireCCI51 and MCD64A1.

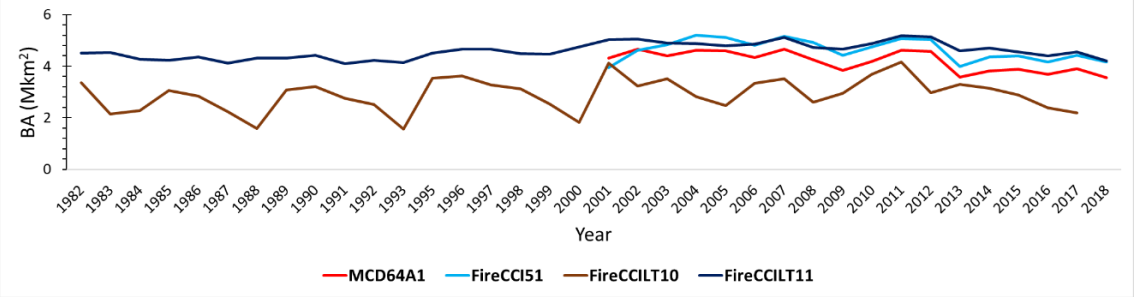

Figure 3.5. Annual BA (Mkm2) trends of MCD64A1, FireCCI51, FireCCILT10 Beta and FireCCILT11.

Comparing the new version with its precursor, FireCCILT11 showed a much more linear trend (without noticeable peaks), particularly during the AVHRR2 period (1982-2000), when FireCCILT10 was much affected by the satellites' orbital drift and the number of available observations (Table 3.3). The SZA and FireCCILT10 were highly correlated in tropical regions (r = -0.89) and globally (r = -0.89) in the AVHRR2 period (<2000), while SZA and FireCCILT11 had a low correlation in tropical regions (r = -0.36) and globally (r = -0.23). The impact of both the number of observations and the solar angle was clearly reduced with the new version of the product, particularly for tropical areas. In fact, the

median of monthly BA between AVHRR2-AVHRR3 periods offers a very high correlation of 0.98, maintaining the monthly trends in the time series.

Table 3.3. Correlation analysis (r Pearson) between the number of observations, SZA, and the BA of FireCCILT10 Beta and FireCCILT11 for the global, tropical and extratropical regions, and the time series of each product. Time periods are grouped as the complete time series, the AVHRR2 period, and the AVHRR3 period.

	#Observations vs. SZA			#Observations vs. BA			SZA vs. BA		
FireCCILT10 beta	1982-2017	1982-2000	2001-2017	1982-2017	1982-2000	2001-2017	1982-2017	1982-2000	2001-2017
Global	-0.90	-0.87	-0.87	0.62	0.64	0.41	-0.81	-0.89	-0.62
Tropical	-0.77	-0.59	-0.78	0.47	0.35	0.32	-0.81	-0.89	-0.61
Extratropical	-0.92	-0.91	-0.87	0.29	0.01	0.28	-0.24	0.06	-0.38
FireCCILT11	1982-2018	1982-2000	2001-2018	1982-2018	1982-2000	2001-2018	1982-2018	1982-2000	2001-2018
Global	-0.82	-0.72	-0.86	0.56	0.12	0.58	-0.62	-0.23	-0.68
Tropical	-0.79	-0.65	-0.83	0.53	0.17	0.37	-0.63	-0.36	-0.62
Extratropical	-0.81	-0.71	-0.85	-0.07	-0.02	0.61	0.14	0.33	-0.54

3.3.3. Regional comparison with MODIS BA products

Table 3.4 shows the average BA by continental region. Similar values were found among the MODIS products and FireCCILT11. Generally, estimations from the FireCCILT11 dataset were higher than for the other products. African regions (NHAF and SHAF) offered the highest BA values in the three products, being FireCCILT11 higher than the MODIS products. FireCCILT11 and FireCCI51 detected in general a similar BA quantity, while MCD64A1 had in most cases lower values. In Australia (AUST), FireCCILT11 detected a BA value in between the two MODIS products although closer to the values of MCD64A1. Boreal regions offered the same BA in North America (BONA) in the three BA products and similar values in Asia (BOAS) between FireCCI products, being much lower in MCD64A1. The lowest burned region changed among products: Equatorial Asia (EQAS) in FireCCILT11, Middle East (MIDE) in FireCCI51 and Europe (EURO) in MCD64A1.

Table 3.4: Average BA in the continental regions for the MODIS (FireCCI51, MCD64A1) and AVHRR-LTDR (FireCCILT11) products in the common time series (2001-2018).

		Continental regions*						
		BONA	TENA	CEAM	NHSA	SHSA	EURO	MIDE
BA (Mkm^2)	FireCCI51	0,45	0,57	0,41	0,98	4,60	0,33	0,25
	MCD64A1	0,45	0,51	0,49	0,96	5,16	0,19	0,25
	FireCCILT11	0,45	0,79	0,51	1,05	5,48	0,46	0,47
		NHAF	SHAF	BOAS	CEAS	SEAS	EQAS	AUST
	FireCCI51	27,19	29,77	2,94	4,23	2,60	0,26	8,67
	MCD64A1	23,00	27,24	1,68	3,51	2,49	0,27	9,23
	FireCCILT11	27,37	29,85	2,77	4,66	2,79	0,32	9,20

*Boreal North America (BONA), Temperate North America (TENA), Central America (CEAM), Northern Hemisphere South America (NHSA), Southern Hemisphere South America (SHSA), Europe (EURO), Middle East (MIDE), Northern Hemisphere Africa (NHAF), Southern Hemisphere Africa (SHAF), Boreal Asia (BOAS), Central Asia (CEAS), Southeast Asia (SEAS), Equatorial Asia (EQAS) and Australia and New Zealand (AUST).

Figure 3.6 shows the temporal variation of BA in the different continental regions for the three BA products. Trends were similar in most of the regions in the common time series. BONA, NHSA, NHAF, SHAF presented analogous trend and values in the BA products. CEAM, BOAS, EQAS and AUST had similar trends and values with slight differences in isolated years or abrupt peaks where FireCCILT11 had softer trends than the MODIS products. In TENA, SHSA, CEAS and SEAS, FireCCILT11 detected similar values of the MODIS products but FireCCILT11 trends were smoother although they conserved the main peaks and trends. Only in regions with little burned area (EURO or MIDE), the estimations were different, although the trends were similar.

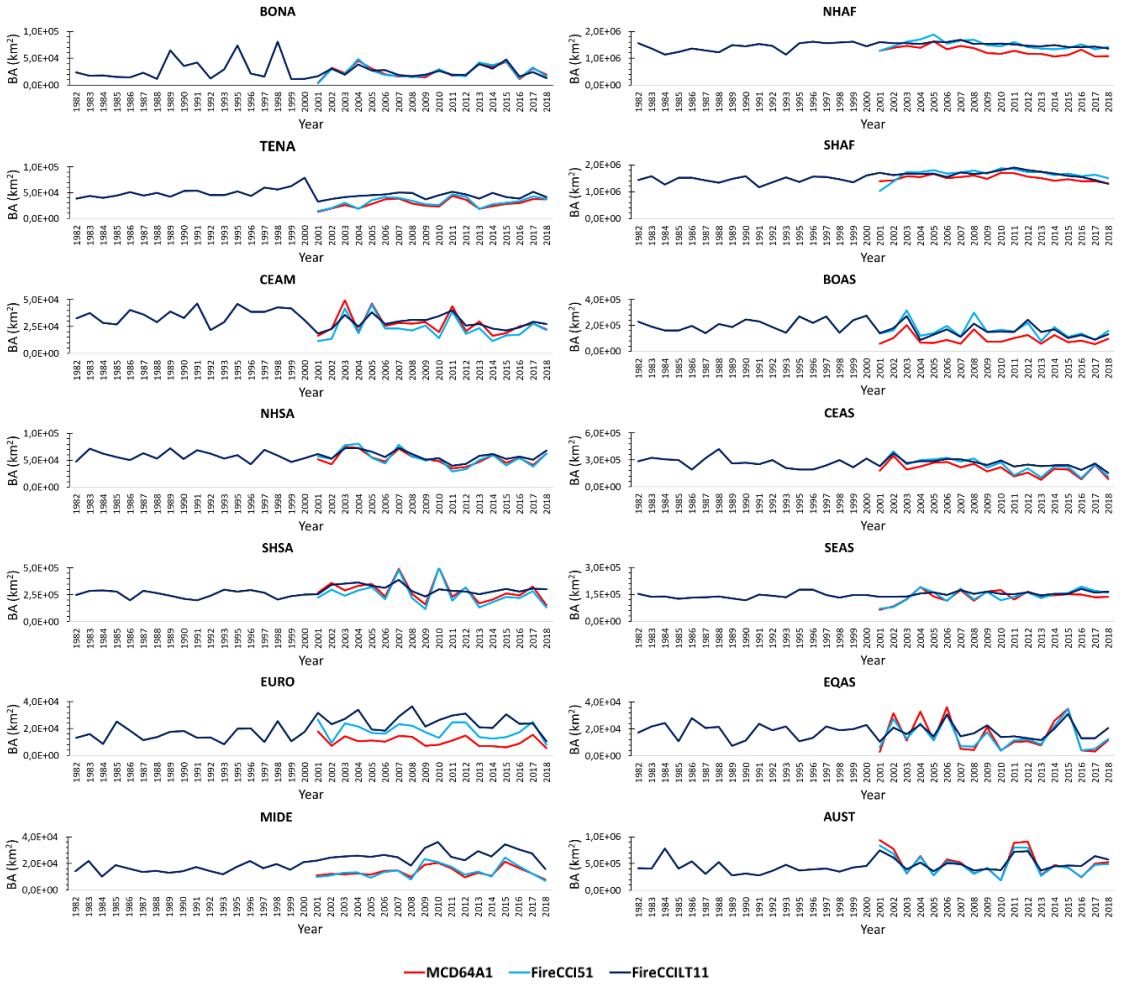

Figure 3.6. Annual BA trends of MCD64A1, FireCCI51 and FireCCILT11 in the different continental regions. See Table 3.4 for the continental regions names.

3.3.4. Comparison with reference fire perimeters

BA data from official perimeters were compared to the four BA products (MCD64A1, FireCCI51, FireCCILT10 and FireCCILT11: Figure 3.7 and Table 3.5). For Australia, national statistics showed similar trends among all BA products, although the former provided higher estimations, while the precursor product (FireCCILT10) had the lowest. FireCCILT11 and national statistics presented a Pearson's correlation of 0.89 and a %MAE of 26% in the common time series (2000-2018).

Canada's official perimeters showed similar trends with all BA products except from FireCCILT10 Beta, and the AVHRR2 period was analogous between the official perimeters and FireCCILT11. The correlation was 0.81 and %MAE 33% in the time series, and similar in the AVHRR2 (r=0.85 and %MAE=45%) and AVHRR3 (r=0.84 and %MAE=23%) periods, with higher BA occurrence for 1989, 1995 and 1998. The

incorporation of a Boreal model proved to be particularly efficient in this area, which was clearly underestimated by the beta version (FireCCILT10), which also underestimated Alaskan fires. These state fire perimeters had a similar trend with all other BA products, although the latter generally underestimate BA. For the pre-MODIS era, the FireCCILT11 product underestimated the BA peaks, although correlation of annual BA values was also high for this period (r = 0.91, %MAE = 61%).

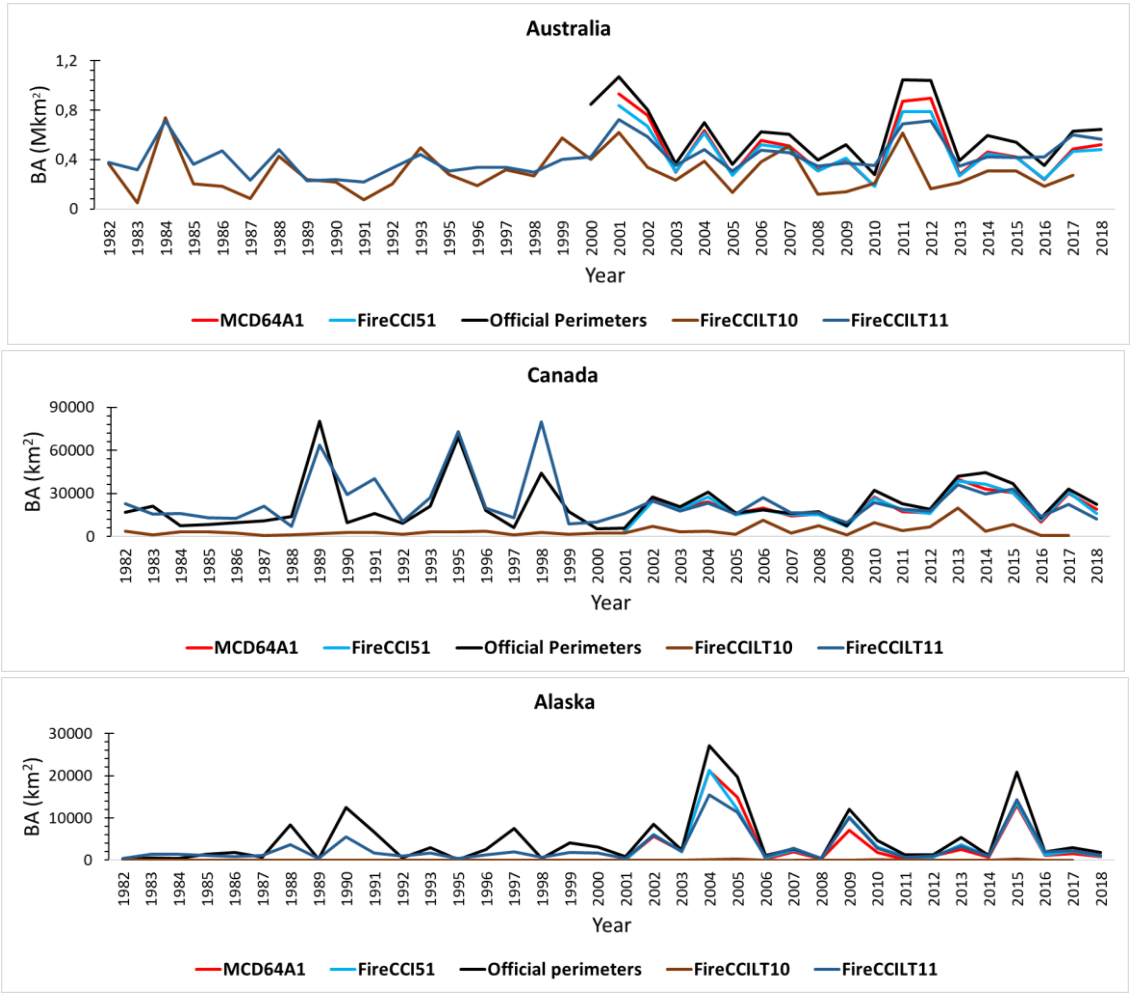

Figure 3.7. Comparison of BA trends among national official perimeters and BA products.

Table 3.5. Correlation analysis (r Pearson) and %MAE between FireCCILT11 in different regions and the official perimeters. Time periods are grouped as the complete time series with official perimeters, the AVHRR2 period, and the AVHRR3 period.

Official perimeters Vs FireCCILT11

Australia			Canada			Alaska		
	R Pearson	%MAE		R Pearson	%MAE		R Pearson	%MAE
2000-2018	0.89	26%	1982-2018	0.81	33%	1982-2018	0.96	42%
2000-2001	-	-	1982-2000	0.85	45%	1982-2000	0.91	61%
2001-2018	0.94	24%	2001-2018	0.84	23%	2001-2018	0.99	33%

We further compared the product with existing regional studies (Table 3.6 and Figure 3.8), although in this case the uncertainty was higher, as those products included also potential errors. The BA estimations done for the Russian republic of Kalmykia (Dubinin et al. 2010) showed a similar trend to FireCCILT11, although with more significant differences in the BA estimation prior to 2001. For the Siberian study (García-Lázaro et al. 2018), the trends and correlation (r = 0.79) were very similar among the BA products during the MODIS era, but this relation was much lower (r = 0.17) before the year 2001. The %MAE had similar values both considering the two differentiated periods and the whole time series. The García-Lázaro et al.'s (2018) study assumed a fully burned pixel (0.05°) if it was detected while FireCCILT11 assigns proportions. Therefore, these authors showed a higher BA detected in the period 1982-2000 but it had a ≈70% less burned pixels than FireCCILT11.

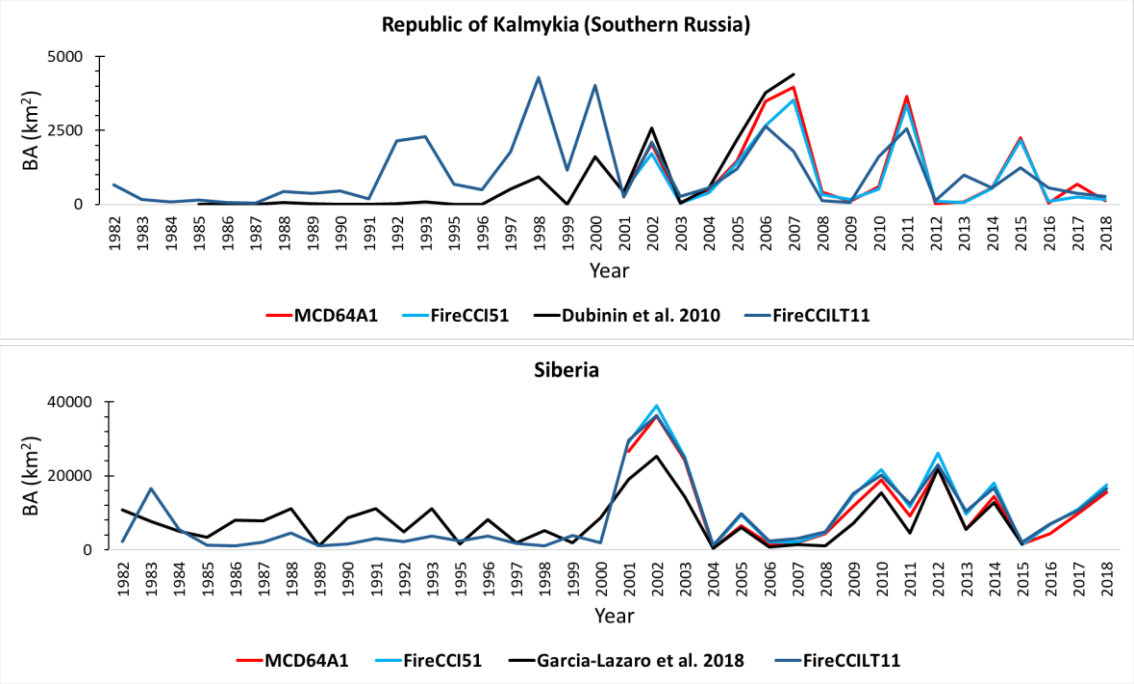

Figure 3.8. Comparison between BA products using regional studies.

Table 3.6. Correlation analysis (r Pearson) and %MAE between FireCCILT11 and the regional BA studies. Time periods are grouped as the complete time series with regional BA studies, the AVHRR2 period, and the AVHRR3 period.

Republic of Kalmykia (Southern Russia)			Siberia		
	R Pearson	%MAE		R Pearson	%MAE
1985-2007	0,48	121%	1982-2015	0,79	62%
1985-2000	0,84	465%	1982-2000	0,17	70%
2001-2007	0,89	40%	2001-2015	0,96	54%

3.4. Discussion

This paper introduces an updated long-term BA product (FireCCILT11) generated from LTDR AVHRR images, covering the period from 1982 to 2018. The product was built upon a beta version released in 2019, aiming to solve some of the problems found in that version.

Generating a BA product from a 5-km-resolution pixel product implies significant challenges, particularly when the input data presents considerable problems of temporal consistency and stability (Giglio and Roy 2020; Otón et al. 2019). Besides, a coarse spatial resolution makes the detection of burned areas in heterogeneous landscapes difficult, particularly in those areas where fires tend to burn in small patches. The size-resolution effect was studied by Boschetti et al. (2004) using the Pareto boundary methodology, finding similar limitations. In addition, the LTDR BA algorithm had to be built without active fire information, which is undoubtedly very important for BA detection (Giglio et al. 2009; Alonso-Canas and Chuvieco 2015). Active fires were detected with full resolution AVHRR images (Flannigan and Vonder Haar 1986; Matson et al. 1987), but with high uncertainty because of the low thermal sensitivity of channel 3 (Flasse and Ceccato 1996). This lack of active fire information increases the difficulty of classifying BA from the LTDR dataset and likely decreases the temporal reporting accuracy. Moreover, the orbital instability of the NOAA satellites and unexpected reception problems further complicates the classification task.

The design of the LTDR BA algorithm took into account these issues and tried to mitigate their impacts. The new version corrects some of the main issues detected in the FireCCILT10 Beta product, particularly the impact of the SZA variations, the changes in the AVHRR configuration, and the poor algorithm performance in boreal regions. In addition, the cloud mask and the methods to establish the detection threshold and BA proportions were improved, which are now regional- and image-based. BA proportions made FireCCILT11 the only global BA product without a binary classification, taking into consideration the great variability within a pixel of low spatial resolution, and striving to make a more realistic detection. The new approach maintains the previous spectral index used as the main input for BA detection and the classification based on RF models. The FireCCILT11 spatial and temporal trends improved significantly compared to FireCCILT10 Beta. FireCCILT11 showed consistency during both AVHRR2 and AVHRR3 periods and showed similar global and regional BA trends to FireCCI51 and MCD64A1. Despite its lower spatial resolution, the use of BA proportions allowed to obtain a total BA similar to the MODIS products. Annual and monthly estimation trends were similar to both MCD64A1 and FireCCI51 BA products. The most burned continent, common

among the global BA products, was Africa, which accounted for a mean of 66% of global BA in FireCCILT11 and MCD64A1, and 68% in FireCCI51.

Comparison with national fire perimeters for Boreal and Tropical countries also showed more consistent trends of FireCCILT11 than its precursor. The tropical region of Australia showed a high correlation (r = 0.89, %MAE = 26%) with the FireCCILT11 BA, although it refers to a short time series (starting in 2000). Boreal regions showed consistent trends with the new product (Canada: r = 0.81, %MAE = 33%; Alaska: r = 0.96, %MAE = 42%), particularly in the detection of peak years, but estimations of the FireCCILT11 were generally lower than those coming from national statistics, which is expected considering the coarse resolution of the LTDR data. For common years with MODIS-based BA products, the FireCCILT11 dataset showed lower agreement with national perimeters than those products, but still maintained similar temporal variation, identifying extreme years. The comparison of estimations provided by FireCCILT11 with other studies (in the Republic of Kalmykia: r=0.48, %MAE=121%; and Siberia: r=0.79, %MAE=62%) showed high temporal variations and BA differences due to the uncertainty of these studies.

Other regional BA databases were also considered for the inter-comparison, such as: California Department of Forestry and Fire Protection's Fire and Resource Assessment Program (FRAP, Available online: https://frap.fire.ca.gov/, last accessed on July 2021), Washington Large Fires (Available online: https://geo.wa.gov/datasets/6f31b076628d4f8ca5a964cbefd2cccc_0, last accessed on July 2021), Wildland Fire Decision Support System (WFDSS, Available online: https://wfdss.usgs.gov/wfdss_help/WFDSS_Help_Historical_Fire_Data.html, last accessed on July 2021), Monitoring Trends in Burn Severity (MTBS, Eidenshink et al. 2007), and the European Forest Fire Information System (EFFIS, Available online: https://effis.jrc.ec.europa.eu/, last accessed on July 2021), but they were deemed not useful because they were not internally consistent or showed incoherencies between different databases of the same region. For this reason, we were not able to performed additional comparisons in other parts of the world in the pre-MODIS era.

Some limitations such as sensor degradation -orbital drift, loss of quality, lack of data- have been minimized but their effects cannot be totally removed. The lack of active fires and the different issues of Channel 3 decrease the temporal accuracy. In addition, the thresholding approach for regional adaptation of BA proportions may provoke border effects in between continental tiles. Still, the use of these regions allowed us to calculate continental thresholds for BA detection and assign BA proportions to cases where no BA was detected in the MODIS era in either FireCCI51 or FireCCILT11. The global thresholding used in the previous approach (Otón et al. 2019) caused that many burned

pixels were lost, and that error was reduced with the new approach. FireCCILT11, like current MODIS products, is expected to underestimate total BA because of the poor detection of small burned patches (Roteta et al. 2019), but further studies should estimate this factor for different regions.

Based on previous limitations, some improvements could be tested in the future, such as introducing new classification approaches (i.e., deep learning models with contextual approaches) or improving the pre-processing with more advanced SZA correction methods. However, considering its limitations, the new FireCCILT11 BA product provides a consistent BA global dataset which extends nearly twenty years the current MODIS BA products. Despite its coarse resolution, this new product detects consistently BA trends globally and regionally, improving significantly the previous beta product, both globally and particularly for boreal regions.

3.5. Conclusion

FireCCILT11 is a global long-term BA database, spanning from 1982 to 2018. It was generated from AVHRR-LTDR data (AVH09, version 5). The algorithm was based on a previous version that was used to generate the beta FireCCILT10. The new version, FireCCILT11, used the same synthetic index (LBI) to increase the fire signal over monthly composites and the same RF approach. The main novelties of the new product include an improved approach for cloud masking, an extension of the RF modelling approach (using now global and boreal models), a new training dataset, and a new method to obtain thresholds per month and region, reducing the impact of the inter-annual variations of the SZA. The inter-comparison with existing global BA products showed high correlations of monthly BA estimations with existing MODIS BA products, MCD64A1 ($r = 0.89$, %MAE = 21%) and FireCCI51 ($r = 0.95$, %MAE = 10%), during their overlapping time series. High correlation values were observed for both pre- and post-MODIS era in those regions where national fire statistics provide long-term estimations. Comparison of temporal trends between FireCCILT11 and official perimeters (Australia: $r = 0.89$, %MAE = 26%; Canada: $r = 0.81$, %MAE = 33%; Alaska: $r = 0.96$, %MAE = 42%) showed a good performance as well. SZA did not inflate any BA pattern in the time series and neither did the number of observations.

Although the FireCCILT11 product has some limitations, such as the coarse spatial resolution and potential border effects, it provides a consistent global BA product based on AVHRR sensors, which complements existing BA datasets, extending them backwards almost 20 years.

3.6. Acknowledgements and product availability

The FireCCILT11 dataset was developed within the ESA Climate Change Initiative (CCI) programme's Fire_cci project (https://climate.esa.int/en/projects/fire/, last accessed on July 2021). The data is freely available through the CCI Open Data Portal (https://climate.esa.int/en/odp/#/dashboard, last accessed on July 2021).

3.7. References

Alonso-Canas, I., & Chuvieco, E. (2015). Global burned area mapping from ENVISAT-MERIS and MODIS active fire data. Remote Sensing Of Environment, 163, 140-152

Beck, H.E., McVicar, T.R., van Dijk, A.I., Schellekens, J., de Jeu, R.A., & Bruijnzeel, L.A. (2011). Global evaluation of four AVHRR–NDVI data sets: Intercomparison and assessment against Landsat imagery. Remote Sensing Of Environment, 115, 2547-2563

Boschetti, L., Flasse, S.P., & Brivio, P.A. (2004). Analysis of the conflict between omission and commission in low spatial resolution dichotomic thematic products: The Pareto Boundary. Remote Sensing Of Environment, 91, 280-292

Boschetti, L., Roy, D.P., Giglio, L., Huang, H., Zubkova, M., & Humber, M.L. (2019). Global validation of the collection 6 MODIS burned area product. Remote Sensing Of Environment, 235, 111490

Breiman, L. (2001). Random forests. Machine learning, 45, 5-32

Bylander, T. (2002). Estimating generalization error on two-class datasets using out-of-bag estimates. Machine learning, 48, 287-297

Canadian Forest Service (2017). Canadian National Fire Database – Agency Fire Data. Natural Resources Canada, Canadian Forest Service, Northern Forestry Centre, Edmonton, Alberta. Available online: http://cwfis.cfs.nrcan.gc.ca/ha/nfdb, last accessed on July 2021.

Carmona-Moreno, C., Belward, A., Malingreau, J.P., Hartley, A., Garcia-Alegre, M., Antonovskiy, M., Buchshtaber, V., & Pivovarov, V. (2005). Characterizing interannual variations in global fire calendar using data from Earth observing satellites. Global Change Biology, 11, 1537-1555

Cihlar, J., Manak, D., & D'Iorio, M. (1994). Evaluation of compositing algorithms for AVHRR data over land. IEEE Transactions On Geoscience and Remote Sensing, 32, 427-437

Copernicus (2019). Algorithm Theoretical Basis Document, Version 1.0. D1.5.2-v1.0_ATBD_ICDR_LC_v2.1_PRODUCTS_v1.0.1. UCLouvain, Belgium, 62p. Available online: https://cds.climate.copernicus.eu/, last accessed on July 2021.

Chuvieco, E., Englefield, P., Trishchenko, A.P., & Luo, Y. (2008). Generation of long time series of burn area maps of the boreal forest from NOAA–AVHRR composite data. Remote Sens. Environ., 112, 2381-2396

Chuvieco, E., Lizundia-Loiola, J., Pettinari, M.L., Ramo, R., Padilla, M., Tansey, K., Mouillot, F., Laurent, P., Storm, T., & Heil, A. (2018). Generation and analysis of a new global burned area product based on MODIS 250 m reflectance bands and thermal anomalies. Earth System Science Data, 10, 2015-2031

Chuvieco, E., Martín, M.P., & Palacios, A. (2002). Assessment of different spectral indices in the red-near-infrared spectral domain for burned land discrimination. International Journal of Remote Sensing, 23, 5103-5110

Chuvieco, E., Mouillot, F., van der Werf, G.R., San Miguel, J., Tanasse, M., Koutsias, N., García, M., Yebra, M., Padilla, M., & Gitas, I. (2019). Historical background and current developments for mapping burned area from satellite Earth observation. Remote Sensing Of Environment, 225, 45-64

Chuvieco, E., Ventura, G., Martín, M.P., & Gomez, I. (2005). Assessment of multitemporal compositing techniques of MODIS and AVHRR images for burned land mapping. Remote Sensing Of Environment, 94, 450 – 462

Devasthale, A., Karlsson, K.-G., Quaas, J., & Graßl, H. (2012). Correcting orbital drift signal in the time series of AVHRR derived convective cloud fraction using rotated empirical orthogonal function. Atmospheric Measurement Techniques, 5, 267-273

Dice, L.R. (1945). Measures of the amount of ecologic association between species. Ecology, 26, 297-302

Dubinin, M., Potapov, P., Lushchekina, A., & Radeloff, V.C. (2010). Reconstructing long time series of burned areas in arid grasslands of southern Russia by satellite remote sensing. Remote Sensing Of Environment, 114, 1638-1648

Dwyer, E., Pereira, J.M.C., Grégorie, J.-M., & DaCamara, C.C. (2000). Characterization of the spatio-temporal patterns of global fire activity using satellite imagery for the period April 1992 to March 1993. Journal of Biogeography, 27, 57-69

Eidenshink, J., Schwind, B., Brewer, K., Zhu, Z.-L., Quayle, B., & Howard, S. (2007). A project for monitoring trends in burn severity. Fire Ecology, 3, 3-21

El Saleous, N., Vermote, E., Justice, C., Townshend, J., Tucker, C., & Goward, S. (2000). Improvements in the global biospheric record from the Advanced Very High Resolution Radiometer (AVHRR). International Journal of Remote Sensing, 21, 1251-1277

ESA (2013). Land Cover CCI: Algorithm Theoretical Basis Document Version 2. Land_Cover_CCI_ATBDv2_2.3, ESA: Louvain, Belgium, 191p. Available online: https://climate.esa.int/media/documents/Land_Cover_CCI_ATBDv2_2.3.pdf, last accessed on July 2021).

Eva, H., & Lambin, E.F. (1998). Remote Sensing of Biomass Burning in Tropical Regions: Sampling Issues and Multisensor Approach. Remote Sensing Of Environment, 64, 292-315

Flannigan, M.D., & Vonder Haar, T.H. (1986). Forest fire monitoring using NOAA satellite AVHRR. Canadian Journal of Forest Research, 16, 975-982

Flasse, S.P., & Ceccato, P. (1996). A contextual algorithm for AVHRR fire detection. International Journal of Remote Sensing, 17, 419-424

García-Lázaro, J., Moreno-Ruiz, J., Riaño, D., & Arbelo, M. (2018). Estimation of burned area in the Northeastern Siberian Boreal Forest from a long-term data record (LTDR) 1982–2015 time series. Remote Sensing, 10, 940

GCOS (2016). The Global Observing System for Climate: Implementation Needs. Geneva, Switzerland: GCOS-200. World Meteorological Organization

Giglio, L., Boschetti, L., Roy, D.P., Humber, M.L., & Justice, C.O. (2018). The Collection 6 MODIS burned area mapping algorithm and product. Remote Sensing Of Environment, 217, 72-85

Giglio, L., Loboda, T., Roy, D.P., Quayle, B., & Justice, C.O. (2009). An active-fire based burned area mapping algorithm for the MODIS sensor. Remote Sensing Of Environment, 113, 408-420

Giglio, L., Randerson, J.T., & Werf, G.R. (2013). Analysis of daily, monthly, and annual burned area using the fourth generation global fire emissions database (GFED4). Journal of Geophysical Research: Biogeosciences, 118, 317-328

Giglio, L., & Roy, D. (2020). On the outstanding need for a long-term, multi-decadal, validated and quality assessed record of global burned area: Caution in the use of Advanced Very High Resolution Radiometer data. Science of Remote Sensing, 2, 100007

Hansen, M., Song, X., DiMiceli, C., Carroll, M., Sohlberg, R., Kim, D.-H., & Townshend, J. (2018). MEaSURES Vegetation Continuous Fields ESDR: Algorithm Theoretical Basis Document (ATBD), Version 2.0. Available from: https://lpdaac.usgs.gov/documents/144/VCF5KYR_ATBD.pdf (accessed on July 2021).

James, M., & Kalluri, S.N. (1994). The Pathfinder AVHRR land data set: an improved coarse resolution data set for terrestrial monitoring. International Journal of Remote Sensing, 15, 3347-3363

Ji, L., & Brown, J.F. (2017). Effect of NOAA satellite orbital drift on AVHRR-derived phenological metrics. International Journal of Applied Earth Observation and Geoinformation, 62, 215-223

Kucêra, J., Yasuoka, Y., & Dye, D.G. (2005). Creating a forest fire database for the Far East of Asia using NOAA/AVHRR observation. International Journal of Remote Sensing, 26, 2423-2439

Lizundia-Loiola, J., Otón, G., Ramo, R., & Chuvieco, E. (2020). A spatio-temporal active-fire clustering approach for global burned area mapping at 250 m from MODIS data. Remote Sensing Of Environment, 236, 111493

Los, S.O., Justice, C., & Tucker, C. (1994). A global 1 by 1 NDVI data set for climate studies derived from the GIMMS continental NDVI data. International Journal of Remote Sensing, 15, 3493-3518

Matson, M., Stephens, G., & Robinson, J. (1987). Fire detection using data from the NOAA-N satellites. International Journal of Remote Sensing, 8, 961-970

McGregor, J., & Gorman, A.J. (1994). Some considerations for using AVHRR data in climatological studies: orbital characteristics of NOAA satellites. International Journal of Remote Sensing, 15, 537-548

Melchiorre, A., & Boschetti, L. (2018). Global analysis of burned area persistence time with MODIS data. Remote Sensing, 10, 750

Moreno-Ruiz, J.A., García-Lázaro, J.R., Arbelo, M., & Cantón-Garbín, M. (2020). MODIS Sensor Capability to Burned Area Mapping—Assessment of Performance and Improvements Provided by the Latest Standard Products in Boreal Regions. Sensors, 20, 5423

Moreno-Ruiz, J.A., García-Lázaro, J.R., Arbelo, M., & Riaño, D. (2019). A Comparison of Burned Area Time Series in the Alaskan Boreal Forests from Different Remote Sensing Products. Forests, 10, 363

Mouillot, F., Schultz, M.G., Yue, C., Cadule, P., Tansey, K., Ciais, P., & Chuvieco, E. (2014). Ten years of global burned area products from spaceborne remote sensing—A review: Analysis of user needs and recommendations for future developments. International Journal of Applied Earth Observation and Geoinformation, 26, 64-79

Otón, G., & Chuvieco, E. (2018). ESA CCI ECV Fire Disturbance: O2.D2 Algorithm Theoretical Basis Document (ATBD) for AVHRR LTDR data, version 1.1. Available from: https://climate.esa.int/en/projects/fire/key-documents/ (accessed on July 2021).

Otón, G., Ramo, R., Lizundia-Loiola, J., & Chuvieco, E. (2019). Global Detection of Long-Term (1982–2017) Burned Area with AVHRR-LTDR Data. Remote Sensing, 11, 2079

Otón, G., Ramo, R., Lizundia-Loiola, J., & Chuvieco, E. (2020). Correction: Otón, G., et al. Global Detection of Long-Term (1982–2017) Burned Area with AVHRR-LTDR Data. Remote Sensing 2019, 11, 2079. Remote Sensing, 12, 2324

Otsu, N. (1979). A threshold selection method from gray-level histograms. IEEE transactions on systems, man, and cybernetics, 9, 62-66

Padilla, M., Olofsson, P., Stehman, S.V., Tansey, K., & Chuvieco, E. (2017). Stratification and sample allocation for reference burned area data. Remote Sensing Of Environment, 203, 240-255

Padilla, M., Stehman, S.V., Hantson, S., Oliva, P., Alonso-Canas, I., Bradley, A., Tansey, K., Mota, B., Pereira, J.M., & Chuvieco, E. (2015). Comparing the accuracies of remote sensing global burned area products using stratified random sampling and estimation. Remote Sens. Environ., 160, 114-121

Pedelty, J., Devadiga, S., Masuoka, E., Brown, M., Pinzon, J., Tucker, C., Vermote, E., Prince, S., Nagol, J., Justice, C., Roy, D., Ju, J., Schaaf, C., Liu, J., Privette, J., & Pinheiro, A. (2007). Generating a long-term land data record from the AVHRR and MODIS

instruments. In, Geoscience and Remote Sensing Symposium, 2007. IGARSS 2007. IEEE International (pp. 1021-1025): IEEE

Pedregosa, F., Varoquaux, G., Gramfort, A., Michel, V., Thirion, B., Grisel, O., Blondel, M., Prettenhofer, P., Weiss, R., & Dubourg, V. (2011). Scikit-learn: Machine learning in Python. the Journal of machine Learning research, 12, 2825-2830

Pinty, B., & Verstraete, M.M. (1992). GEMI: a non-linear index to monitor global vegetation from satellites. Vegetatio, 101, 15-20. https://doi.org/10.1007/bf00031911.

Plank, S., & Martinis, S. (2018). A Fully Automatic Burnt Area Mapping Processor Based on AVHRR Imagery—A TIMELINE Thematic Processor. Remote Sensing, 10, 341

Ramo, R., & Chuvieco, E. (2017). Developing a Random Forest Algorithm for MODIS Global Burned Area Classification. Remote Sensing, 9, 1193

Ramo, R., García, M., Rodríguez, D., & Chuvieco, E. (2018). A data mining approach for global burned area mapping. International Journal of Applied Earth Observation and Geoinformation, 73, 39-51

Riaño, D., Ruiz, J.A.M., Isidoro, D., & Ustin, S.L. (2007a). Global spatial patterns and temporal trends of burned area between 1981 and 2000 using NOAA-NASA Pathfinder. Global Change Biology, 13, 40-50, doi: 10.1111/j.1365-2486.2006.01268.

Riaño, D., Ruiz, J.M., Martínez, J.B., & Ustin, S. (2007b). Burned area forecasting using past burned area records and Southern Oscillation Index for tropical Africa (1981–1999). Remote Sensing Of Environment, 107, 571-581

Rodriguez-Galiano, V.F., Ghimire, B., Rogan, J., Chica-Olmo, M., & Rigol-Sanchez, J.P. (2012). An assessment of the effectiveness of a random forest classifier for land-cover classification. ISPRS Journal of Photogrammetry and Remote Sensing, 67, 93-104

Roteta, E., Bastarrika, A., Padilla, M., Storm, T., & Chuvieco, E. (2019). Development of a Sentinel-2 burned area algorithm: Generation of a small fire database for sub-Saharan Africa. Remote Sensing Of Environment, 222, 1-17

Roy, D. (1997). Investigation of the maximum normalized difference vegetation index (NDVI) and the maximum surface temperature (Ts) AVHRR compositing procedures for the extraction of NDVI and Ts over forest. International Journal of Remote Sensing, 18, 2383-2401

Stengel, M., Stapelberg, S., Sus, O., Finkensieper, S., Würzler, B., Philipp, D., Hollmann, R., Poulsen, C., Christensen, M., & McGarragh, G. (2020). Cloud_cci Advanced Very High Resolution Radiometer post meridiem (AVHRR-PM) dataset version 3: 35-year climatology of global cloud and radiation properties. Earth System Science Data, 12, 41-60

Stroppiana, D., Pinnock, S., Pereira, J.M.C., & Grégorie, J.M. (2002). Radiometric analysis of SPOT-VEGETATION images for burnt area detection in Northern Australia. Remote Sensing Of Environment, 82, 21-37

Tian, F., Fensholt, R., Verbesselt, J., Grogan, K., Horion, S., & Wang, Y. (2015). Evaluating temporal consistency of long-term global NDVI datasets for trend analysis. Remote Sensing Of Environment, 163, 326-340

Tucker, C.J., Pinzon, J.E., Brown, M.E., Slayback, D.A., Pak, E.W., Mahoney, R., Vermote, E.F., & El Saleous, N. (2005). An extended AVHRR 8-km NDVI dataset compatible with MODIS and SPOT vegetation NDVI data. International Journal of Remote Sensing, 26, 4485-4498

Villaescusa-Nadal, J.L., Franch, B., Roger, J.-C., Vermote, E.F., Skakun, S., & Justice, C. (2019). Spectral adjustment model's analysis and application to remote sensing data. IEEE Journal of Selected Topics in Applied Earth Observations and Remote Sensing, 12, 961-972

Weber, H., & Wunderle, S. (2019). Drifting Effects of NOAA Satellites on Long-Term Active Fire Records of Europe. Remote Sensing, 11, 467

Yates, C.P., Edwards, A.C., & Russell-Smith, J. (2009). Big fires and their ecological impacts in Australian savannas: size and frequency matters. International Journal of Wildland Fire, 17, 768-781

Yue, C., Ciais, P., Cadule, P., Thonicke, K., & van Leeuwen, T.T. (2015). Modelling the role of fires in the terrestrial carbon balance by incorporating SPITFIRE into the global vegetation model ORCHIDEE – Part 2: Carbon emissions and the role of fires in the global carbon balance. Geosci. Model Dev. Discuss, 8, 1321-1338

Capítulo 4

VALIDATION OF LOW SPATIAL RESOLUTION AND NO-DICHOTOMY GLOBAL LONG-TERM BURNED AREA PRODUCT BY PARETO BOUNDARY

This study was published in the SPIE conference proceedings (Earth Resources and Environmental Remote Sensing/GIS Applications XII [pp. 293-299]) in 2021.

Abstract

The validation of low-resolution remote sensing products using high-resolution data may be affected by different error factors that would eventually imply unrealistic accuracy estimations. The usual validation methodologies were designed for high or medium resolution but may be not very adequate for coarse resolution, particularly when trying to separate those errors associated to classification from those related to the actual pixel size. The Pareto Boundary methodology can be a good alternative to discriminate between those two sources of errors. We tested its application to a recently released global burned area product based on AVHRR data. This product was developed within the Fire_cci project of the European Space Agency (ESA). The product, named FireCCITL11, has the coarsest resolution (0.05°) and the longest time series (1982-2018) compared to all other global BA products. Furthermore, FireCCILT11 is the only global BA product without a dichotomy classification which detects BA proportions.

The accuracy of the FireCCILT11 was validated by Pareto Boundary and an independent reference dataset of Landsat at 0.05°. FireCCILT11 was usually close to boundary curve or below it, which indicates suitable performance. Commission errors (Ce) were usually lower than Omission errors (Oe) in the time series, like other BA products such as those based on MODIS sensor. Both types of accuracy errors present low values, although there were unbalanced years. Year 2014 showed the lowest errors for the entire time series with balanced errors (Ce = 0.12 and Oe = 0.14).

4.1. Introduction

Validation of a remote sensing product is generally performed by comparing classification of medium- and high-resolution satellite products (Padilla et al. 2017; Padilla et al. 2015). However, standard procedures may not be appropriate to validate low-resolution products, as they may mix classification errors with those related to the actual pixel size. Therefore, the accuracy estimations may be unrealistic (Boschetti et al. 2006). An alternative is to resample the high resolution product to the spatial resolution of the low resolution one, thus mitigating the impact of two very contrasting pixel sizes. Low resolution has less data variance and reduced information, so that resampling high resolution decreases the variance (Justice et al. 1989) and allows a fair comparison. Pareto boundary methodology (Boschetti et al. 2004) takes into account this issue and facilitates a fair approach for validation of low-resolution products. This methodology seeks to learn whether the errors are due to the performance of the product or, on the contrary, to the spatial resolution of the sensor itself. This method has been used in several studies of low resolution such as snow studies (Pepe et al. 2010) or burned area

(BA) (Anaya and Chuvieco 2012; Katagis et al. 2014; Moreno-Ruiz et al. 2020; Moreno-Ruiz et al. 2019; Oliva et al. 2011).

Currently, the FireCCILT11 (Otón et al. 2021) product presents the longest time series (1982-2018) and the coarsest spatial resolution (0.05°) among existing BA products. The most used are the MCD64A1 (Giglio et al. 2018) (NASA's official BA product, with a spatial resolution 500m) and the FireCCI51 (Lizundia-Loiola et al. 2020) (ESA CCI's official product, spatial resolution 250m). We present in this paper a recently developed BA product, part of the Fire_cci project of the European Space Agency. The spatial and temporal consistency of the product was checked with the global BA products available, official perimeters (regional but long-term) and regional studies (literature) (Otón et al. 2021). Despite its consistent results, a validation is an interesting way to learn the performance of this product in places where there is no other information available, although the process is labor-intensive.

We present in this paper, the validation of the FireCCILT11 product, based on the Pareto Boundary approach. In addition to its coarse resolution, this BA product presents a particularity with respect to other global BA datasets, as it was generated from a non-dichotomy classification.

4.2. Methods

4.2.1. Global long-term Burned Area product

FireCCILT11 (spatial resolution 0.05°≈5 km) is a monthly global BA product which covers the period from 1982 to 2018 (except 1994), the longest time series currently available using satellites images. This long-term BA product was developed from the AVH09 product of the Land Long-Term Data Record (LTDR) data based on images acquired by the Advanced Very High Resolution Radiometer (AVHRR 2/3) sensor on board of the National Oceanic and Atmospheric Administration (NOAA) satellites from 1981 until the present (NOAA 7-19). LTDR data was produced by NASA, degrading the Global Area Coverage (GAC: 4x4 km) format of the AVHRR sensor at 0.05° since the AVHRR full original resolution (approx. 1 km2) was not available globally until the nineties. FireCCILT11 was generated from the LTDR resolution at 0.05°, along with BA summaries at 0.25° resolution. This product detects BA proportions, understanding the great variability of a pixel of coarse resolution and making realistic detections. FireCCILT11 presented consistent trends with global BA products and official perimeters (Otón et al. 2021).

4.2.2. Landsat dataset

Independent reference data has to be developed to accurately assess a product (Franquesa et al. 2020; Justice et al. 2000). For the purposes of this paper, a Landsat BA dataset was created covering an area in Southern Hemisphere Africa (in coincidence with the SAFNet boundaries (Roy et al. 2005)). BA was mapped using multi-temporal pairs of Landsat images masking out non-observed areas. Additionally, Long units (consecutive pairs of images) of Landsat were generated because these were more adequate in low-resolution products and reduce the influences of temporal reporting accuracy (Lizundia-Loiola et al. 2020; Padilla et al. 2018). Long unit dataset was developed in Africa (Figure 4.1) in a place with the largest availability of images on the continent (Southeast of Angola) according to Wulder et al. (2016) from 1989 to 2018 (27 years), and 183 images were used in total. Africa was selected because it is the most burned continent (Lizundia-Loiola et al. 2020) and we sought a scene which was cloud-free as long as possible. The objective was to map the fire season, and all the consecutive available images were included, although it was not possible to achieve the same temporal coverage in all years. Some years only have 3 consecutive images available (1992, 1997, 2007 and 2008), others only 2 (2009 and 2012) and others, only one or none (those before 1989 and 1999, 2000 and 2010 as well). Also, some years have non-interpretable areas (1998 and 2006) or Landsat 7 SLC-off gaps (2003, 2004, 2007, 2009, 2011 and 2012). Therefore, obtaining a long-term data set of independent reference data had many limitations and problems. The location to be studied was described as having large fires (Ramo et al. 2021) in the central months of the fire season but with a weak burned signal, while the first months of the fire season were characterized by small fires (Lizundia-Loiola et al. 2020).

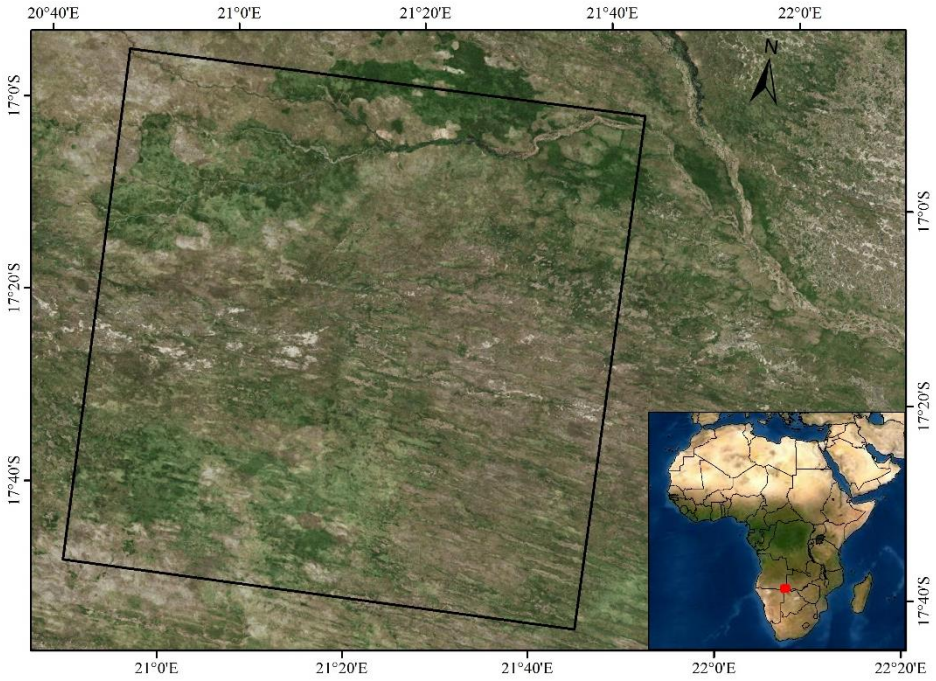

Figure 4.1. Location of the validation area in the Southeast of Angola (Africa).

4.2.3. Validation

The assessment of FireCCILT11 accuracy was calculated with the most common statistical measures in current BA validations (Lizundia-Loiola et al. 2020; Padilla et al. 2017; Padilla et al. 2015; Roteta et al. 2019), such as Ce, Oe, relative Bias (relB) and Dice Coefficient (DC). The statistical DC (Dice 1945) incorporates the omission and commission error of the BA class, and indicates the conditional probability that a burned pixel in the reference data will be detected as burned by the classification. Also, trends and Pearson correlation (r) were designed to show the correlation and behavior of the product with the independent reference data.

$$Ce = \frac{False\ Positives}{Total\ Burned\ of\ the\ Product\ \ Classification} \tag{4.1}$$

$$Oe = \frac{False\ Negatives}{Total\ Burned\ of\ the\ Reference\ \ Classification} \tag{4.2}$$

$$Dice\ Coefficient = \frac{2 \cdot True\ Positives}{2 \cdot True\ Positives + False\ Positives + False\ Negatives} \tag{4.3}$$

$$relB\ = \frac{False\ Positives - False\ Negatives}{Total\ Burned\ of\ the\ Reference\ \ Classification} \tag{4.4}$$

4.2.4. Pareto Boundary

Previous statistics can be misleading in low resolution if we do not have a reference. Therefore, we need a methodology that shows what we can expect from low resolution and what we cannot. Pareto boundary methodology (Boschetti et al. 2004) accomplished that function. This method tells us whether the accuracy of the product is due to either the performance of the algorithm or the low resolution. Initially, Pareto boundary was generated to binary classifications but it was able to be adapted to proportions. Also, that method was developed to work with the same resolutions, which means that high resolution should be resampled to the low resolution. High resolution resampled (Hr), which maintained BA proportions, was categorized in different BA percentages (0%, 10%, 20%, n%) and binarized (Hb, burned-unburned), dichotomy classifications (Hb) were obtained and were validated against High resolution resampled (Hr). Boundary curve was the trade-off between omission and commission error developed between high resolution resampled (Hr) and the dichotomy classifications (Hb). A binary low resolution (Lbr) product could never pass the boundary curve because its spatial resolution did not hold that much accuracy. But a low-resolution proportion (Lr) product was in fact able to do it, if a performance was very accurate (Boschetti et al. 2004). We did two analyses with Pareto boundary: First, low-resolution (Lr) product was categorized (Lbr) according to proportions (0% 10%, 20%, n%) and validated with High-resolution resampled (Hr) to learn whether our product follows a similar trend according to BA proportions. Secondly, low-resolution (Lr) product was validated with High-resolution resampled (Hr) to identify the true accuracy of our product with reference data. In both cases, omission and commission error were calculated.

4.3. Results

Validation between Landsat dataset degraded at low resolution (0.05°) and FireCCILT11 is shown in Table 4.1. Several limitations in the validation dataset reduced the accuracy and altered the assessment of these years. Commission errors were usually lower than omission errors in the time series; although both presented low values, there were unbalanced years. The AVHRR2 period had fewer years to validate with that Landsat dataset and had the years with the greatest unbalanced, presenting higher differences in the errors than the AVHRR3 period. Relative Bias noticed underestimation of BA except in some years with limitations, both in the AVHRR2 period and in the AVHRR3 period. The AVHRR2 period had more underestimation. The AVHRR3 period showed higher DC values than the AVHRR2 period although both had years with high DC values. Year 1989 was the best year of the validation years in the AVHRR2 period with a high DC

of 0.63. 2014 was the best year of the time series with balanced errors around 10 and DC of 0.87.

The correlation in the time series between Landsat dataset and FireCCILT11 was 0.53, in the AVHRR2 period was 0.52 and in the AVHRR3 period was 0.72.

Table 4.1. Validation outcomes between FireCCILT11 and the long-term degraded Landsat dataset. * represents the years when the Landsat period is lower or equal to one and a half months, and the long-unit is minimal (2-4 scenes Landsat); ^ is used when there are non-interpretable areas and the study area is reduced; +, when there are Landsat 7 with SLC-Off, and # when the Landsat period is lower or equal to one and a half months and there are Landsat 7 with SLC-Off.

	1989	1990	1991	1992*	1993	1995*	1996	1997*	1998^
Commission error	0,23	0,09	0,04	0,00	0,47	0,45	0,11	0,26	0,00
Omission error	0,47	0,57	0,74	1,00	0,40	0,96	0,90	0,95	0,90
real Bias	-0,31	-0,53	-0,73	-1,00	0,13	-0,93	-0,89	-0,93	-0,90
Dice Coefficient	0,63	0,58	0,41	0,00	0,56	0,07	0,17	0,10	0,17
	2001	2002	2003+	2004#	2005	2006^	2007#	2008*	2009#
Commission error	0,09	0,10	0,42	0,60	0,31	0,14	0,77	0,30	0,40
Omission error	0,41	0,41	0,25	0,37	0,48	0,29	0,21	0,33	0,25
real Bias	-0,35	-0,34	0,30	0,57	-0,24	-0,17	2,46	-0,03	0,26
Dice Coefficient	0,72	0,71	0,66	0,49	0,60	0,78	0,36	0,69	0,67
	2011+	2012#	2013	2014	2015	2016	2017	2018	
Commission error	0,92	0,47	0,08	0,12	0,07	0,09	0,08	0,21	
Omission error	0,05	0,32	0,24	0,14	0,29	0,34	0,27	0,40	
real Bias	11,25	0,27	-0,17	-0,02	-0,23	-0,28	-0,20	-0,24	
Dice Coefficient	0,14	0,60	0,84	0,87	0,81	0,76	0,81	0,68	

Pareto boundary analysis is shown in Figure 4.2 for several years (1989, 1996, 2003 and 2014). Hypothetical binary FireCCILT11 presented a related curve regarding boundary curve which indicated a consistent pattern according to the different percentiles of proportions. The detection of different proportion of burned followed the same pattern in FireCCILT11 as Landsat. FireCCILT11 presented errors close to the boundary curve for most years, highly improving a hypothetic binary FireCCILT11. FireCCILT11 never even had a higher error than binary FireCCILT11, showing an adequate performance of the proportions. Despite some years in Table 4.1 with high errors, Pareto boundary showed a high performance of the algorithm and the main cause of high errors was due to spatial resolution. A great example was 1996 where there was a high Omission error and low DC, but FireCCILT11 was beneath boundary curve, which showed a good performance of the algorithm. Improvement would be possible for some years, bringing them closer to boundary curve, but the performance of FireCCILT11 was high and some years were in the boundary curve or beneath it. The AVHRR2 period presented results similar to the

AVHRR3 period, and showed a high performance of the algorithm that only in Table 4.1 it was not possible to display. The behavior of FireCCILT11 was higher than a dichotomy product, even if that was high-resolution degraded. The validation of FireCCILT11 (Table 4.1) and Pareto boundary methodology (Figure 4.2) showed a consistent and coherent product in the whole time series.

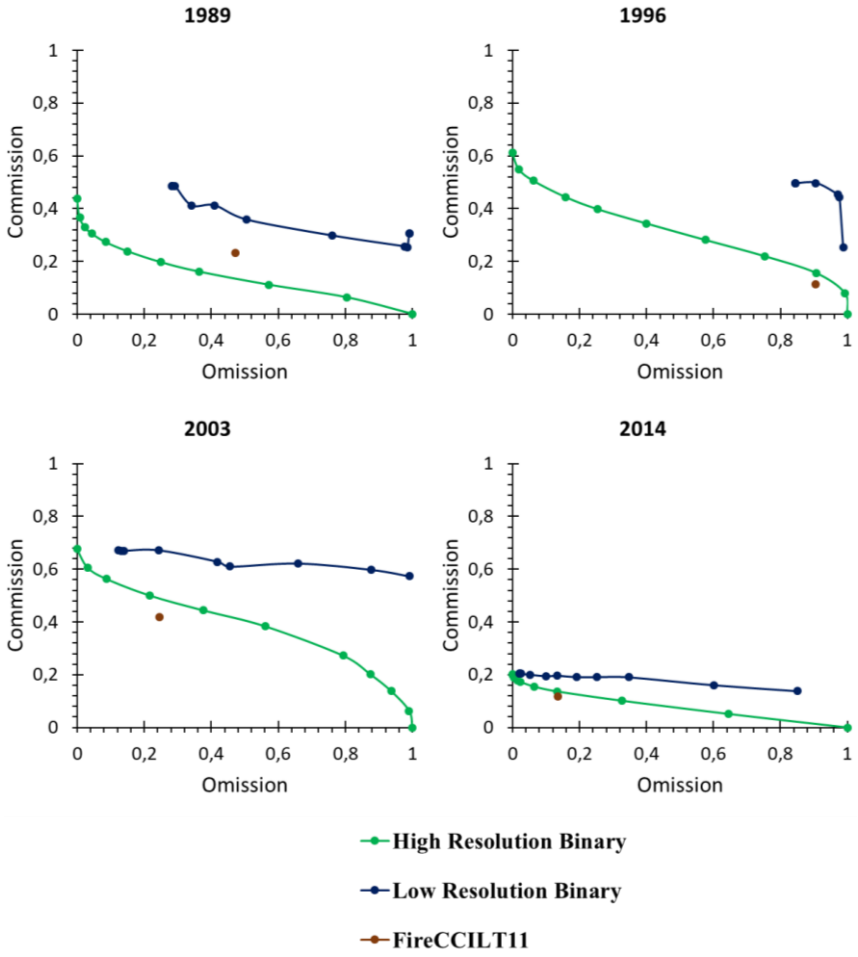

Figure 4.2. Pareto boundary with a long-term Landsat dataset which was resampled at low resolution and binarized in percentiles of proportions (green), FireCCILT11 binarized according to percentiles of proportion (blue) and FireCCILT11 (brown).

4.4. Discussion

A long-term BA algorithm and product (FireCCILT11) were validated in this paper. A first limitation was the poor representation and variability of heterogeneous areas in the low resolution data (Justice et al. 1989). The degradation of GAC, and later transformation to LTDR, created a loss of variability in the signal bias (Eva and Lambin 1998) that made change detection difficult.

The creation of Landsat dataset to validate according to CEOS-LPVS protocols (Boschetti et al. 2006; Padilla et al. 2017; Padilla et al. 2015) (http://lpvs.gsfc.nasa.gov, accessed August 2021) is unrealistic for a long-term series product since the human effort will be too high and the obtaining of images could be unavailable (Wulder et al. 2016). Therefore, a small but long-term Landsat dataset was created in the most affected fire region. We used more images (183) and years (27) than other studies such as Roy et al. (2005) where in 11 African locations, 53 images were used in a single year (2001), Boschetti et al. (2006) which used 33 Landsat scenes and images in 2000, and Roy and Boschetti (2009) which used 11 Landsat (consecutive acquisitions) in 2001. MCD64A1 (Giglio et al. 2018) validation used a similar number of images in 108 Landsat scenes (consecutive acquisitions).

Considering the spatial resolution in general, it was shown clearly that the smaller fire sizes include a higher likelihood of error, which has also been observed in other studies (Fraser et al. 2004). That was the main problem in dichotomy products but soft classifications or products based in proportion of BA were able to improve the accuracy and reduce errors, especially in medium and low resolution (Pepe et al. 2010), like FireCCILT11. Current MODIS products underestimated BA, and they assumed a fully burned pixel. The same applies to African analysis, where Roy et al. (2005) found underestimation of the area burned at subcontinental scale in MCD45 (500 m), GlobCarbon (1 km), and L3JRC (1 km), as well as worse performance, as function of a decreased sensor resolution. Analysis by Anaya and Chuvieco (2012) in South America compared the three latter BA and also found high omission errors, greater than commission errors. FireCCILT11 was not an exception and showed higher errors of omission than commission, BA proportions reduced the errors but the coarse resolution always had an error associated with its loss of variability.

Spatial resolution was also a limitation in the validation (Boschetti et al. 2004). High-resolution datasets were common in these analyses but low-resolution products were not. If the main objective was to discern the performance of a product, it was not possible to work with too much spatial resolution difference. The accuracy of the product and the algorithm had to be validated with the same spatial resolution and in this way, the interpreter was able to differentiate whether the error was due to the algorithm or to the spatial resolution. Pareto Boundary (Boschetti et al. 2004) in FireCCILT11 indicated a possible improvement in some years. Omission errors were higher than commission errors, which were very low most times. The loss of variability in the low-resolution images did not allow detection of small fires or low fire signal. FireCCILT11 had analogous patterns to the reference data according to BA proportions which observed good performance in the different proportions in the burned pixel. FireCCILT11 was usually close to boundary curve or below it, which showed good

performance of the algorithm. Spatial resolution was the main effect in high errors and it was inevitable. Depending on the AVHRR period, FireCCILT11 had a noticeable difference in the errors and DC, but Pareto Boundary associated the error to spatial resolution because the curve boundary was near, or the AVHRR2 sensor had less quality than AVHRR3. FireCCILT11, like the other BA products, tended to underestimate BA, as did MODIS products (Giglio et al. 2018; Lizundia-Loiola et al. 2020; Moreno-Ruiz et al. 2020; Padilla et al. 2015) or LTDR products (Moreno-Ruiz et al. 2013; Otón et al. 2019). Therefore, Pareto Boundary demonstrated a high performance of the FireCCILT11 and the main cause of errors was due to spatial resolution.

4.5. Conclusions

FireCCILT11 is the single consistent and global long-term BA database which spans from 1982 to 2018. The product was assigned to complement current global BA products, which were mainly based on MODIS data and with a shorter time series (>2000). Moreover, this new product was based on AVHRR sensors, different from the other global BA products that were only provided by MODIS.

The validation was done with an independent reference dataset which covered 27 years and 183 images in Africa. Long units of Landsat were limited for images available, clouds, non-interpretable areas and sensor problems, although they complied with the SAFNet boundaries. A novel validation was developed with BA proportions which improved the BA detection and reduced errors. FireCCILT11 showed higher omission than commission errors, and therefore underestimated BA like all other global BA products. In addition, the low resolution presented an associated error, due to its loss of variability. FireCCILT11 was usually close to the Pareto Boundary curve or below it, and the proportions of BA were analogous to the high-resolution dataset. The AVHRR2 period showed more uncertainty than AVHRR3 due to the quality sensor, although both periods were consistent and were adjusted to boundary curve. The main error in the performance of FireCCILT11 was due to spatial resolution, demonstrating a high performance of the FireCCILT11 algorithm.

4.6. References

Anaya, J.A., & Chuvieco, E. (2012). Accuracy Assessment of Burned Area Products in the Orinoco Basin. Photogrammetric Engineering and Remote Sensing, 78, 53-60

Boschetti, L., Brivio, P.A., Eva, H.D., Gallego, J., Baraldi, A., & Gregoire, J.M. (2006). A sampling method for the retrospective validation of Global Burned Area products. IEEE Transactions On Geoscience and Remote Sensing, 44, 1765-1773

Boschetti, L., Flasse, S.P., & Brivio, P.A. (2004). Analysis of the conflict between omission and commission in low spatial resolution dichotomic thematic products: The Pareto Boundary. Remote Sensing Of Environment, 91, 280-292

Dice, L.R. (1945). Measures of the amount of ecologic association between species. Ecology, 26, 297-302

Eva, H., & Lambin, E.F. (1998). Remote Sensing of Biomass Burning in Tropical Regions: Sampling Issues and Multisensor Approach. Remote Sensing Of Environment, 64, 292-315

Franquesa, M., Vanderhoof, M.K., Stavrakoudis, D., Gitas, I.Z., Roteta, E., Padilla, M., & Chuvieco, E. (2020). Development of a standard database of reference sites for validating global burned area products. Earth System Science Data, 12, 3229-3246

Fraser, R.H., Hall, R.J., Landry, R., Lynham, T., Raymond, D., Lee, B., & Li, Z. (2004). Validation and calibration of Canada-wide coarse-resolution satellite burned-area maps. Photogrammetric Engineering and Remote Sensing, 70, 451-460

Giglio, L., Boschetti, L., Roy, D.P., Humber, M.L., & Justice, C.O. (2018). The Collection 6 MODIS burned area mapping algorithm and product. Remote Sensing Of Environment, 217, 72-85

Justice, C., Belward, A., Morisette, J., Lewis, P., Privette, J., & Baret, F. (2000). Developments in the'validation'of satellite sensor products for the study of the land surface. International Journal of Remote Sensing, 21, 3383-3390

Justice, C., Markham, B., Townshend, J., & Kennard, R. (1989). Spatial degradation of satellite data. International Journal of Remote Sensing, 10, 1539-1561

Katagis, T., Gitas, I.Z., Toukiloglou, P., Veraverbeke, S., & Goossens, R. (2014). Trend analysis of medium-and coarse-resolution time series image data for burned area mapping in a Mediterranean ecosystem. International Journal of Wildland Fire, 23, 668-677

Lizundia-Loiola, J., Otón, G., Ramo, R., & Chuvieco, E. (2020). A spatio-temporal active-fire clustering approach for global burned area mapping at 250 m from MODIS data. Remote Sensing Of Environment, 236, 111493

Moreno-Ruiz, J.A., García-Lázaro, J.R., Arbelo, M., & Cantón-Garbín, M. (2020). MODIS Sensor Capability to Burned Area Mapping—Assessment of Performance and Improvements Provided by the Latest Standard Products in Boreal Regions. Sensors, 20, 5423

Moreno-Ruiz, J.A., García-Lázaro, J.R., Arbelo, M., & Riaño, D. (2019). A Comparison of Burned Area Time Series in the Alaskan Boreal Forests from Different Remote Sensing Products. Forests, 10, 363

Moreno-Ruiz, J.A., García-Lázaro, J.R., Riaño, D., & Kefauver, S.C. (2013). The Synergy of the 0.05º (5km) AVHRR Long-Term Data Record (LTDR) and Landsat TM Archive to Map Large Fires in the North American Boreal Region From 1984 to 1998. IEEE Journal of Selected Topics in Applied Earth Observations and Remote Sensing, 7, 1157-1166

Oliva, P., Martin, P., & Chuvieco, E. (2011). Burned area mapping with MERIS post-fire image. International Journal of Remote Sensing, 32, 4175-4201

Otón, G., Lizundia-Loiola, J., Pettinari, L., & Chuvieco, E. (2021). Development of a Consistent Global Long-Term Burned Area product (1982-2018) based on AVHRR-LTDR data. International Journal of Applied Earth Observation and Geoinformation, 103, 102473

Otón, G., Ramo, R., Lizundia-Loiola, J., & Chuvieco, E. (2019). Global Detection of Long-Term (1982–2017) Burned Area with AVHRR-LTDR Data. Remote Sensing, 11, 2079

Padilla, M., Olofsson, P., Stehman, S.V., Tansey, K., & Chuvieco, E. (2017). Stratification and sample allocation for reference burned area data. Remote Sensing Of Environment, 203, 240-255

Padilla, M., Stehman, S.V., Hantson, S., Oliva, P., Alonso-Canas, I., Bradley, A., Tansey, K., Mota, B., Pereira, J.M., & Chuvieco, E. (2015). Comparing the accuracies of remote sensing global burned area products using stratified random sampling and estimation. Remote Sens. Environ., 160, 114-121

Padilla, M., Wheeler, J., & Tansey, K. (2018). ESA CCI ECV Fire Disturbance: D4.1.1 Product Validation Report, version 2.1. Available online: https://climate.esa.int/en/projects/fire/key-documents/, last accessed on October 2020.

Pepe, M., Boschetti, L., Brivio, P.A., & Rampini, A. (2010). Comparing the performance of fuzzy and crisp classifiers on remotely sensed images: A case of snow classification. International Journal of Remote Sensing, 31, 6189-6203

Ramo, R., Roteta, E., Bistinas, I., Van Wees, D., Bastarrika, A., Chuvieco, E., & Van der Werf, G.R. (2021). African burned area and fire carbon emissions are strongly impacted by small fires undetected by coarse resolution satellite data. Proceedings of the National Academy of Sciences, 118, 1-7

Roteta, E., Bastarrika, A., Padilla, M., Storm, T., & Chuvieco, E. (2019). Development of a Sentinel-2 burned area algorithm: Generation of a small fire database for sub-Saharan Africa. Remote Sensing Of Environment, 222, 1-17

Roy, D., Frost, P., Justice, C., Landmann, T., Roux, J., Gumbo, K., Makungwa, S., Dunham, K., Du Toit, R., Mhwandagara, K., Zacarias, A., Tacheba, B., Dube, O., Pereira, J., Mushove, P., Morisette, J., Santhana, S., & Davies, D. (2005). The Southern Africa Fire Network (SAFNet) regional burned area product validation protocol. International Journal of Remote Sensing, 26, 4265-4292

Roy, D.P., & Boschetti, L. (2009). Southern Africa Validation of the MODIS, L3JRC and GlobCarbon Burned-Area Products. IEEE Transactions On Geoscience and Remote Sensing, 47, DOI 10.1109/TGRS.2008.2009000

Wulder, M.A., White, J.C., Loveland, T.R., Woodcock, C.E., Belward, A.S., Cohen, W.B., Fosnight, E.A., Shaw, J., Masek, J.G., & Roy, D.P. (2016). The global Landsat archive: Status, consolidation, and direction. Remote Sensing Of Environment, 185, 271-283

Capítulo 5

ANALYSIS OF TRENDS IN THE FIRECCI GLOBAL LONG TERM BURNED AREA PRODUCT (1982–2018)

This analysis was published in the Fire Journal (4, 74) in 2021.

Abstract

We present an analysis of the spatio-temporal trends derived from long-term burned area (BA) data series. Two global BA products were included in our analysis, the FireCCI51 (2001–2019) and the FireCCILT11 (1982–2018) datasets. The former was generated from Moderate Resolution Imaging Spectroradiometer (MODIS) 250 m reflectance data, guided by 1 km active fires. The FireCCILT11 dataset was generated from Land Long-Term Data Record data (0.05°), which provides a consistent time series for Advanced Very High Resolution Radiometer images, acquired from the NOAA satellite series. FireCCILT11 is the longest time series of a BA product currently available, making it possible to carry out temporal analysis of long-term trends. Both products were developed under the FireCCI project of the European Space Agency. The two datasets were pre-processed to correct for temporal autocorrelation. Unburnable areas were re-moved and the lack of the FireCCILT11 data in 1994 was examined to evaluate the impact of this gap on the BA trends. An analysis and comparison between the two BA products was performed using a contextual approach. Results of the contextual Mann-Kendall analysis identified significant trends in both datasets, with very different regional values. The long-term series presented larger clusters than the short-term ones. Africa displayed significant decreasing trends in the short-term, and increasing trends in the long-term data series, except in the east. In the long-term series, Eastern Africa, boreal regions, Central Asia and South Australia showed large BA decrease clusters, and Western and Central Africa, South America, USA and North Australia presented BA increase clusters.

5.1. Introduction

Fire is a global phenomenon that affects ecosystems and the atmosphere (GCOS 2016; Granier et al. 2011; Urbanski et al. 2008; Ward et al. 2012). It is a critical component of the Climate System and therefore it has been identified as one of the Essential Climate Variables (ECVs) by the Global Climate Observing System (GCOS 2016). Consequently, Fire Disturbance was selected as one of the projects of the Climate Change Initiative (CCI) Programme of the European Space Agency (ESA). FireCCI aims to produce consistent, long-term and global Burned Area (BA) datasets, mostly oriented towards climate modellers (Chuvieco et al. 2018). This BA information is critical to assess the environmental impacts of biomass burning, as well as to analyse fire regime characteristics and temporal changes.

During the last two decades, several global BA datasets have been produced and made available to the international community (Chuvieco et al. 2019). The most reliable ones

are based on the Moderate Resolution Imaging Spectroradiometer (MODIS) sensor, including the MCD64A1 (NASA's official product: Giglio et al. 2018) and the FireCCI51 (ESA CCI's official product: Lizundia-Loiola et al. 2020a). The spatial resolution of these datasets is 500 m and 250 m, respectively, and they cover a time span of 20 years (2001 up to date).

Despite the interest of short time series products, several authors have indicated the convenience of generating a longer time series to extend the analysis of global fire-environment relationships (GCOS 2016). Climate modellers (Chuvieco et al. 2019; Mouillot et al. 2014) recommended extending the BA datasets backwards, using historical data, to improve their knowledge on climate dynamics (Hantson et al. 2016). The obvious choice for a long-term product would be based on the Advanced Very High Resolution Radiometer (AVHRR) sensor, on board the National Oceanic and Atmospheric Administration (NOAA) satellites since 1979. However, the lack of a global and consistent archive of AVHRR-NOAA data at its full original resolution (approx. 1 km2) was preventing the community from undertaking this effort. An alternative was to use a coarser resolution dataset, based on the Global Area Coverage (GAC: 4 × 4 km) format of the AVHRR sensor. NASA delivered a corrected time series, named Land Long-Term Data Record (LTDR, Pedelty et al. 2007), which assembles GAC data at 0.05-degree resolution from 1981 to 2021 (although after 2018 the dataset is quite noisy).

In spite of the challenges of detecting BA from this coarse resolution, with the limited spectral resolution of AVHRR and lacking active fire information, a BA product based on this time series has been recently released within the FireCCI project. The product is named FireCCILT11 (Otón et al. 2021b), and covers the period from 1982 to 2018. It was based on a previous beta version published in 2019 (Otón et al. 2019), trying to mitigate its temporal inconsistencies.

Trend analyses have been quite common in the remote sensing literature, including for temperature (Eastman et al. 2009) and vegetation (Mishra et al. 2015; Neeti and Eastman 2011; Neeti et al. 2012). The trend analysis of global BA datasets has been conducted at a regional (Silva et al. 2019; Urbieta et al. 2019; Zubkova et al. 2019) and global (Andela et al. 2017; Earl and Simmonds 2018; Forkel et al. 2019) scale. These studies aimed to detect regional variations of trends, to identify contrasting temporal changes. For instance, Andela et al. (2017) analysed global trends in BA, showing regions with increasing and decreasing trends, linked mainly to regional land use changes.

Regarding BA analysis, regional studies used long-term data but global studies used short-term data, although they were not limited geographically. Silva et al. (2019) analysed the spatial and temporal trends of BA in the Iberian Peninsula and Urbieta et

al. (2019) studied spatio-temporal changes in fire frequency and size in Spain. Both of these studies dealt with time series for over 30 years. Zubkova et al. (2019) analysed changes in fire activity in Africa from 2002 to 2016, while Andela et al. (2017) analysed long-term trends in burned area for the period 1998–2015, based on the fourth version of Global Fire Emissions Database (GFED4, Giglio et al. 2013). Earl and Simmonds (2018) studied global and regional spatiotemporal fire trends from 2001 to 2016 using active fires of MODIS (MOD14A1), and Forkel et al. (2019) analysed global and regional BA trends from 1996 to 2015 with GFED4 and FireCCI50 data (Chuvieco et al. 2018).

The objective of this study was to analyse global trends in BA using the FireCCILT11 long-term BA product, which extends almost 20 years (1982–2018) backwards from the other available BA datasets. The introduction of FireCCILT11 is a novelty in this kind of analysis. We aimed to detect areas where BA time series displayed significant positive or negative trends, and evaluate whether trends were consistent at different time spans and spatial resolutions.

5.2. Materials and Methods

The three main steps of our trend mapping methodology are shown in Figure 5.1.

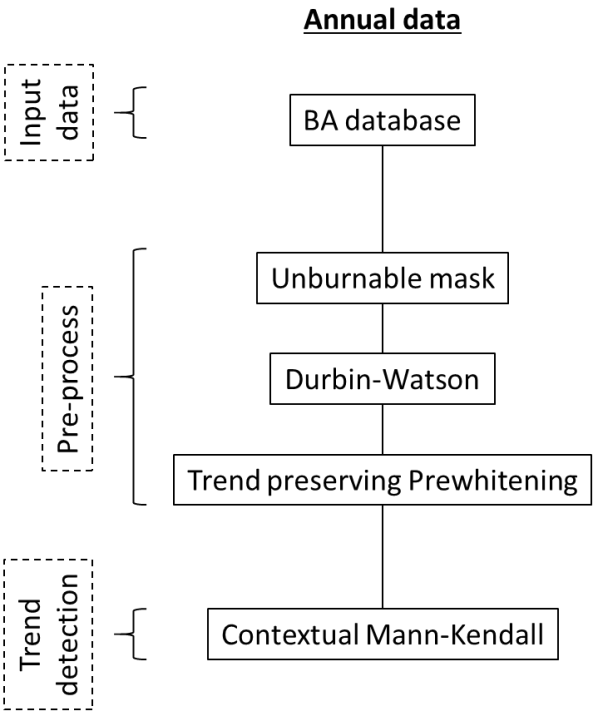

Figure 5.1. Outline of the methodology used to process the FireCCILT11 and FireCCI51 data.

5.2.1. Data

First, the temporal and spatial series of two global burned area products, FireCCILT11 (Otón et al. 2021b) and FireCCI51 (Lizundia-Loiola et al. 2020a) were obtained. Both products were included in the trend analysis to clarify the impact of spectral and spatial resolution, on one hand, and the length of the time series, on the other, in the significance of the detected trends.

5.2.1.1. FireCCILT11

Global long-term BA information was obtained from the FireCCILT11 product (Otón et al. 2021b), which is the longest (1982–2018) global BA dataset currently available based on satellite images. The FireCCILT11 product does not include the year 1994 due to a long gap of ten months caused by the extended noise and sensor degradation of the original AVHRR images, which makes the LTDR data useless for BA mapping. FireCCILT11 includes monthly BA data estimates at 0.05° cell resolution, although the formatted product also offers monthly BA summaries at 0.25° resolution. BA detection was based on the LTDR-AVH09 product, generated by NASA from the AVHRR 2/3 sensors using seven NOAA satellites. Although the coarse resolution of the LTDR data hampers accurate detection of burned pixels, the FireCCILT11 product has shown consistent trends with other global BA products, as well as with national fire perimeters (Alaska Interagency Coordination Center 2021; Canadian Forest Service 2017; North Australia & Rangelands Fire Information 2021) of those regions where long-term fire statistics exist (Otón et al. 2021b). In addition, FireCCILT11 was long-term validated (Otón et al. 2021a) and both AVHRR periods presented similar accuracy.

5.2.1.2. FireCCI51

The second global BA product used in our trend analysis was the FireCCI51 (Lizundia-Loiola et al. 2020a) dataset, also developed within the CCI programme. The product covers the period 2001–2019, and offers monthly BA data at 250 m and 0.25° resolution. This dataset was used to calibrate the classification algorithm used to generate the FireCCILT11 product, and therefore both products are quite consistent in the common temporal period. The FireCCI51 dataset was generated from MODIS 250 m reflectance da-ta, guided by 1 km active fires images. Both products are freely downloadable from the ESA CCI data portal (European Space Agency and Fire_cci project team 2021).

5.2.1.3. Analysis of Burned Area Datasets

Several factors were considered to analyse the impact of the datasets on the detection of trends. First, the impact of spatial resolution was tested by running the process on each product at several resolutions: the original detail of the FireCCILT11 product (0.05°), the summary BA provided by the official formatted product at 0.25°, and the commonly used climate modelling grid at 0.5° resolution.

Another important issue was the potential effect of the 1994 gap of the FireCCILT11 product. To test the effect of this gap, in addition to the original FireCCILT11 dataset (used as control), three BA products were created using several criteria to fill the 1994 gap by means of: (a) the maximum value of BA at each grid cell in the time series, (b) the mini-mum value of BA at each grid cell in the time series, (c) the mean value of BA at each grid cell in the time series.

5.2.2. Pre-Processing

Second, the input data were pre-processed according to the previous dataset analysis (Section 5.2.1.3.). Unburnable areas were discarded using a global Land Cover (LC, Copernicus 2019; ESA 2013) product. Temporal autocorrelation was detected using the Durbin-Watson statistic (Durbin and Watson 1950), and was removed using trend-preserving prewhitening (Wang and Swail 2001).

5.2.2.1. Unburnable Mask

Global and annual LC information is available from the ESA's CCI Land Cover v2.0.7 (CCI-LC, ESA 2013) product and the Copernicus Climate Change Service (C3S) Global Land Cover (C3S-LC, Copernicus 2019) products v2.1.1. These products are annual, CCI-LC from 1992 to 2015 and C3S-LC from 2016 to 2020, and the combination of both ex-tends from 1992 to 2020. They have a spatial resolution of 300 m and are fully consistent with each other (Copernicus Programme 2021). We generated a burnable land mask (Otón et al. 2021b), reclassifying the land cover information into burnable and unburnable binary classes, and resampling it to the AVH09 resolution (0.05 degrees) using the criteria that if any pixel is burnable then the whole grid cell is classified as burnable. Unburnable areas correspond to the land cover classes bare soil, water, urban areas, and permanent snow and ice, while the burnable areas are all the vegetated classes in the land cover products. After that process, a single land cover mask was created, keeping only the grid cells that were burnable during the whole time series, to avoid no-data issues in the dataset.

5.2.2.2. Temporal Autocorrelation

Trend analysis requires pre-processing to mitigate the effects of temporal autocorrelation (Wang and Swail 2001; Yue and Wang 2002). Temporal autocorrelation is the absence of independence between observations in a time series. It may lead to false rejections of the null hypothesis (type I error) and to overestimation of trend significance (Douglas et al. 2000), and affects the variance of the Mann-Kendall test statistic (Yue and Wang 2002). We relied on the Durbin-Watson test (Durbin and Watson 1950) to assess temporal autocorrelation and on the pre-whitening procedure of Wang and Swail (2001) to remove it. The pre-whitened time series displays the same trend as the original series, but their data are free of temporal autocorrelation (Wang and Swail 2001).

5.2.3. Trend Detection

After addressing the spatial resolution, unburnable areas and temporal autocorrelation in both datasets, and the 1994 data gap issue in the long-term dataset, annual BA spatiotemporal trends were analysed.

Contextual and temporal trends were generated with the contextual Mann-Kendall (CMK) approach (Neeti and Eastman 2011) and the slope estimation for annual data. The Mann-Kendall test (Kendall 1975; Mann 1945) is a classic non-parametric test to assess monotonic trends (Chandler and Scott 2011), which addresses each cell independently, assuming independent data. Neeti and Eastman (2011) developed the contextual Mann-Kendall (CMK) test, a version of the original test that assesses trends in a 3 × 3 cell spatial neighbourhood centred at each cell in a regular grid. The rationale for the CMK test is to rely on local spatial autocorrelation, which takes into account a cluster of neighbour pixels, reducing the noise contributed by remote trends of individual pixels and producing more reliable trend significance estimates (Fuller and Wang 2014). However, the CMK test also assumes data independence, but reliance on a local spatial window reduces the data variance, resulting in increased likelihood of false trend detection (Yue and Wang 2002). This effect was taken into account by adjusting the variance, following the approach of Douglas et al. (2000).

The slope of the BA trend in each grid cell was estimated with the non-parametric Theil-Sen (TS) regression (Sen 1968; Theil 1950). This slope estimator is given by the median of the slopes calculated between observations at all pair-wise time steps. The TS estimator is very robust to the presence of outliers, such that it can tolerate up to 29.3% (breakdown point) bad observations in its input data-points without degradation of its

slope estimation accuracy. This estimator is recommended for time series with large inter-annual variability such as annual BA, or data gap such as 1994 in the FireCCILT11 product. The significance of CMK trend was tested using the Z-score, selecting a confidence level of 95% ($p \leq 0.05$), with the Z test statistic following standard normal distribution.

5.3. Results

5.3.1. Burned Area Dataset Analysis

As explained in Section 5.2.1.3, the BA datasets (FireCCILT11 and FireCCI51) were resampled individually to three spatial resolutions (0.05°, 0.25°, 0.5°) to learn which one was more consistent to detect BA trends on a global scale. CMK was calculated for each resolution of each product, as shown in Figure 5.2 in the case of FireCCILT11. The 0.5° resolution maintained a high trade-off between spatial detail and trend detection in order to study global patterns. In addition, the 0.5° spatial process was faster than higher resolutions and required less computational power. Higher resolutions (0.05° and 0.25°) presented slight trends and were more disaggregated than the lowest resolution. For these reasons it was decided to perform the analysis at 0.5° spatial resolution.

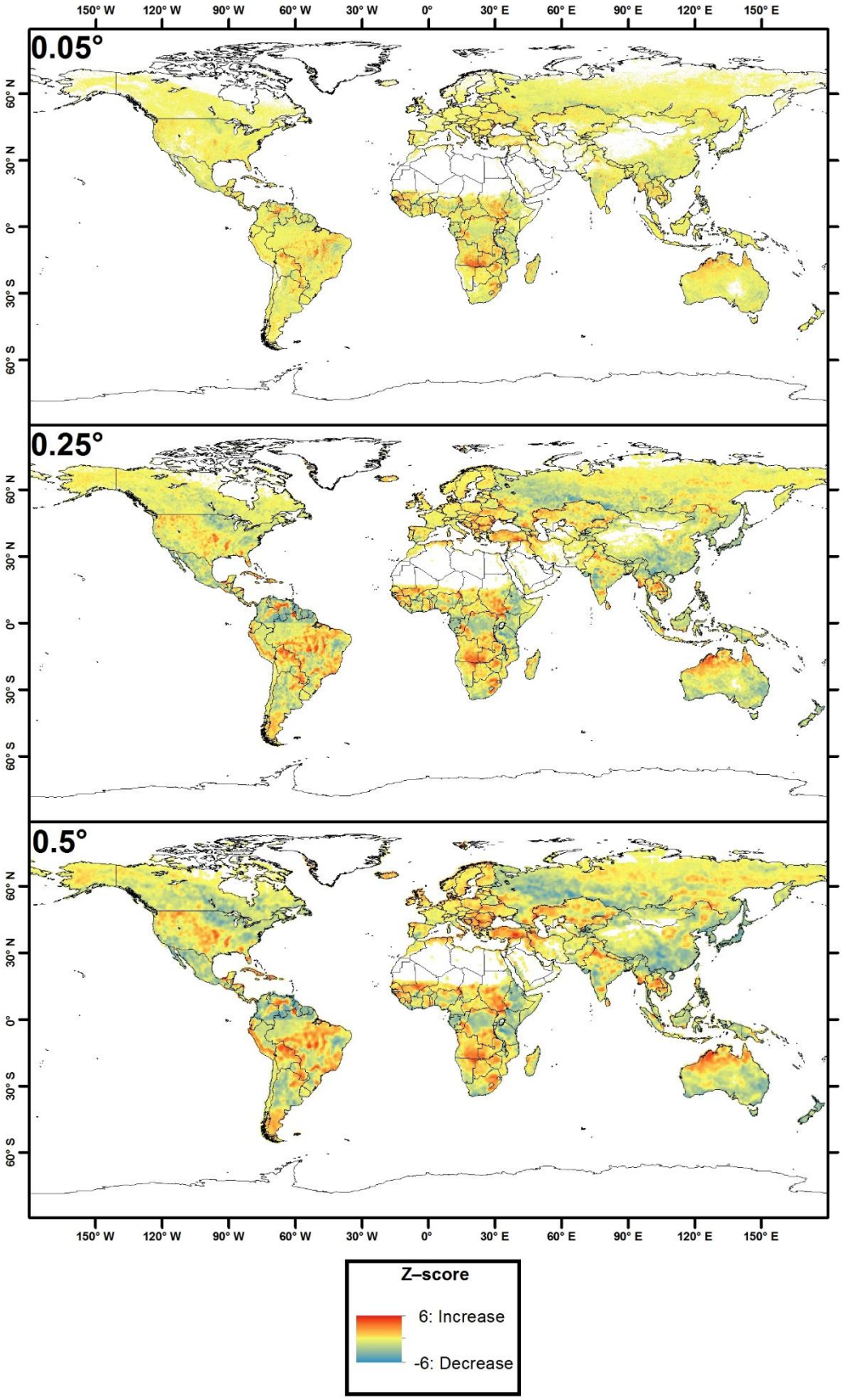

Figure 5.2. Comparison of Z–score, obtained by the CMK approach, between the three different spatial resolution in the FireCCILT11 (1982–2018) dataset.

Additionally, the effect of the 1994 gap was analysed for the four datasets (control, max, min, and mean). These datasets were generated at 0.5° and CMK was performed. Figure 5.3 shows the comparison among the significant trends, with a confidence level of 95%, in the different datasets. The three datasets created showed values with differences of less than 30% from the control dataset in negative significant trends and less than 15% in positive significant trends. The max and the min datasets obtained 13% less negative trends than the control dataset, while the mean dataset had a 10% more. Regarding positive trends, the maximum dataset obtained 29% less trends, the minimum dataset 6% more and the mean dataset 3% less than the control dataset.

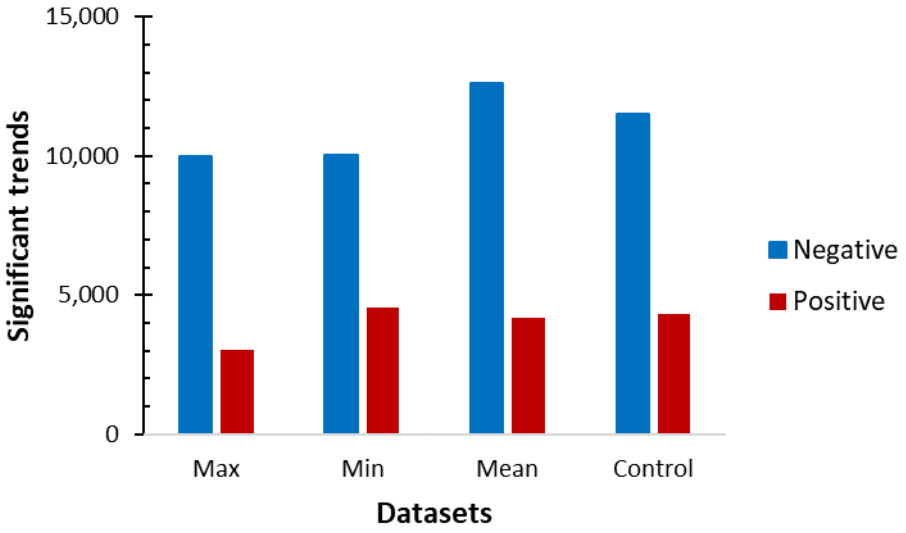

Figure 5.3. Comparison between the significant trends in the four datasets (confidence level of 95%).

These results showed that CMK and the Theil-Sen estimator are very robust to the presence of outliers, since they can tolerate a substantial fraction of bad observations without losing accuracy. The results were not much affected when the missing observations for 1994 were replaced with either the maximum, the minimum or the mean of all observed values. Due to the consistent trends, the dataset was generated with the control approach, without the year 1994.

Despite choosing the most consistent dataset according to previous analyses, limitations were found in the dataset. The trend detection procedure reflected all these imperfections contained in the products. First, continental regions (Giglio et al. 2013) were used for computing the BA data for the FireCCILT11 product. This regional adaptation has the potential to introduce discontinuities in trends between regions. For instance, a strong border effect was found in South America. In particular, this effect occurs at the border of two continental regions (Giglio et al. 2013) Northern Hemisphere

South America (NHSA) and Southern Hemisphere South America (SHSA). This border effect was more evident at lower spatial resolution because the aggregation of pixels and trends makes it more visible. When the resolution was higher, such as the original resolution (0.05°), this border effect was smoother, as well as in the remaining trends (Figure 5.2). Second, some anomalous trends or discontinuities were found in the FireCCILT11 product in the year 2000, when there was a change in the sensor, namely from AVHRR-2 (1982–2000) to AVHRR-3 (2001–2018). This type of problem affected 5% of clusters (30 out of 594) with significant trends, and corresponding to BA commission errors in the FireCCILT11 product. Those clusters were visually identified and excluded from further analysis. Despite that, FireCCILT11 got a consistent BA in NHSA and the remaining continental regions. No other anomalies were found in FireCCI51.

5.3.2. Contextual Mann-Kendall Test and Slope Estimation

5.3.2.1. Short-Term Series

In the case of the short-term (2001–2018) dataset, spatial trends are shown in Figure 5.4. Significant trends (with a confidence level of 95%) are shown in Figure 5.5. Large decrease clusters were predominant with respect to smaller increase clusters. Burned area change trends vary regionally. Northern tropical Africa presented decreasing trends, while Equatorial Africa showed a combination of decreasing (East) and increasing (West) trends. The traditional fire regions of South America (Los Llanos and El Gran Chaco) had negative trends, while the new fire areas in the Central and North East showed positive trends. In North America, mostly positive trends were observed, particularly in the SE of USA. Asia presented decreasing trends in Central Asia, and increasing trends in India and Central Siberian Plateau. Finally, Australia presented decreasing BA clusters in the North, and in-creasing trends in the South.

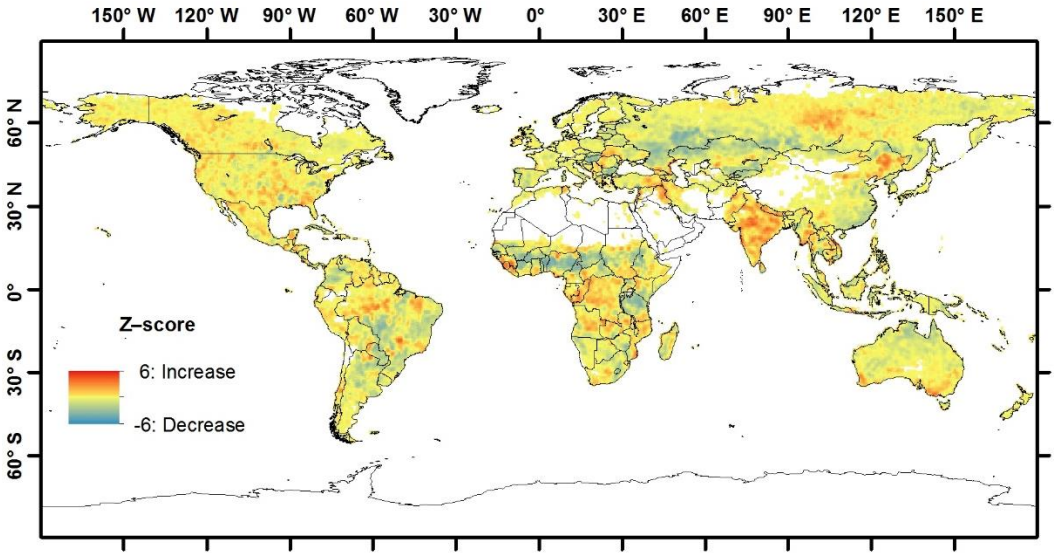

Figure 5.4. Spatial representation (0.5°) of Z–score of the increase and decrease trends of BA in the short-term series (FireCCI51, 2001–2018).

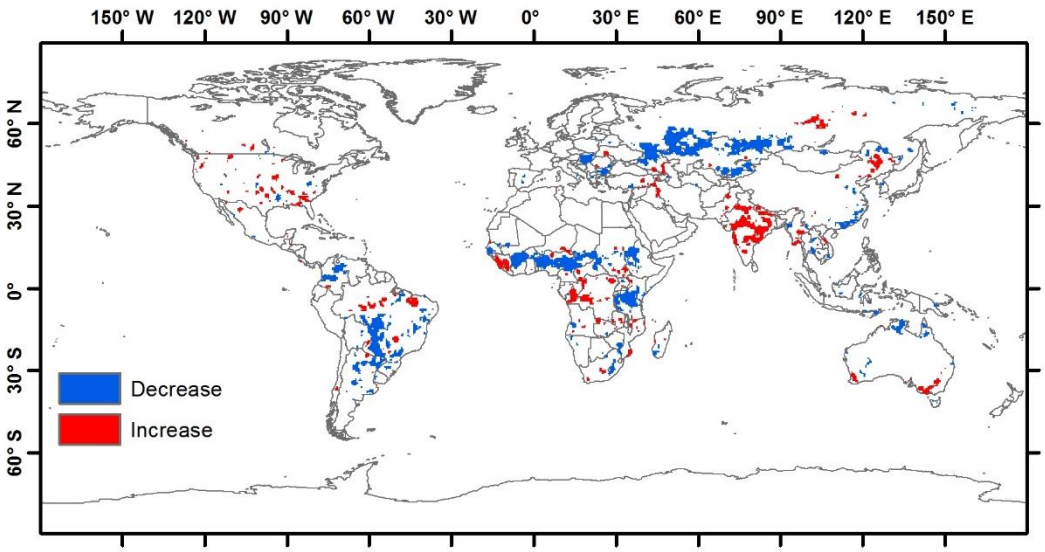

Figure 5.5. Significant trends of BA in the short-term series (2001–2018) for the high-resolution BA product (FireCCI51), selecting a confidence level of 95%.

The common time series of FireCCILT11 (Figure 5.6) with FireCCI51 was analysed and it showed similar trends, although the short-term series of FireCCILT11 presented smaller clusters. The detection resolution of FireCCI51 allowed more accurate measures and trends. Despite that, both products in the common time series showed mostly high spatial similarities. Figure 5.7 shows the spatial correlation between FireCCI51-FireCCILT11 in the period 2001–2018. High spatial correlations are displayed with Pearson correlation (r) > 0.75 in pixels of all regions.

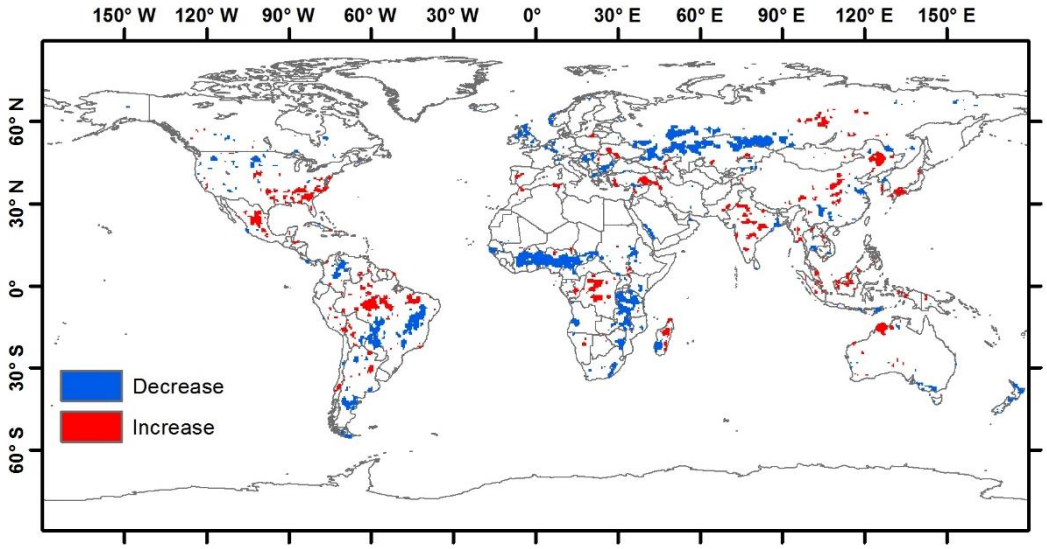

Figure 5.6. Significant trends of BA (with a confidence level of 95%) in the short-term series (2001–2018) for the low-resolution BA product (FireCCILT11).

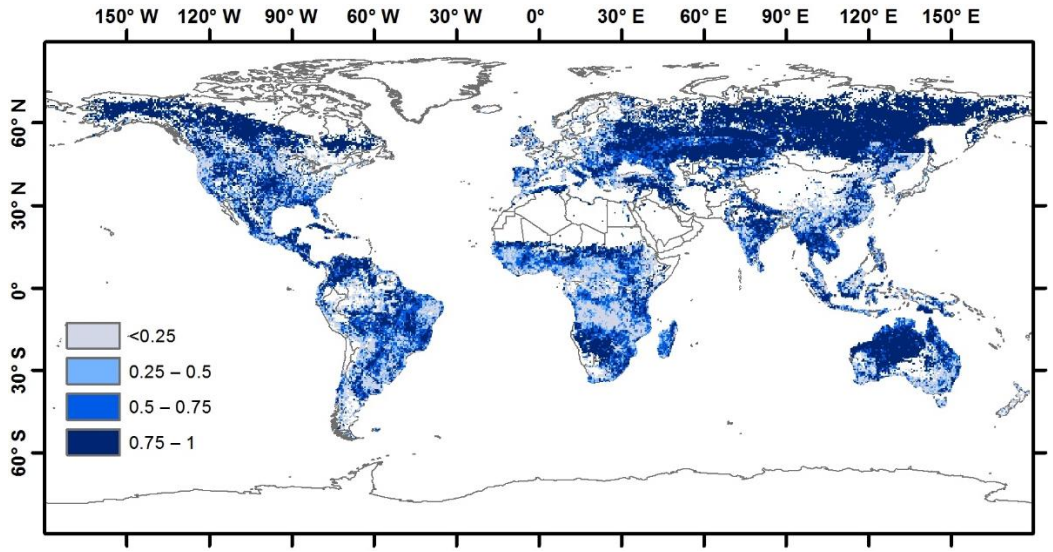

Figure 5.7. Spatial correlation between the common time series (2001–2018) of both BA datasets.

Comparing significant trends in both products in the common time series, Figure 5.8 shows the agreement and disagreement in the significant patterns. Agreement is where the same significant trends are located in the same place in both products. Disagreement showed where each product had a significant opposite trend in the same location. Agreement was widely predominant in all regions, with decreasing trends predominating over increasing trends, and disagreement was minor. Agreement in decreasing trends were present in Africa, South America (Los Llanos and El Gran Chaco) and Asia (central region). Agreement in increasing trends appeared in Africa (central region), America (USA and centre of Brazil) and Asia (Siberia and India). Australia did not present spatial agreement in significant tends.

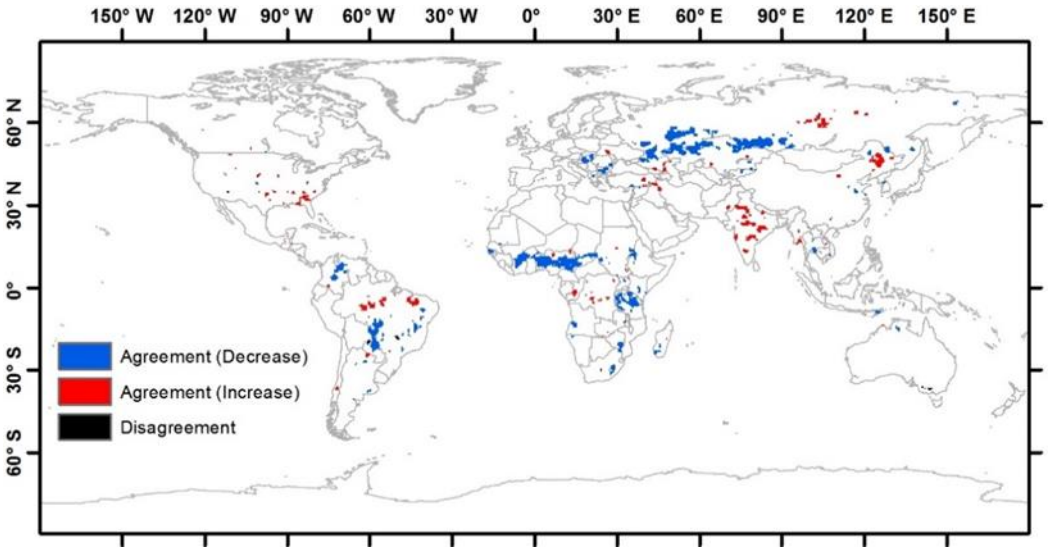

Figure 5.8. Spatial comparison (Agreement-Disagreement) of significant trends between the common time series (2001–2018) of the burned area datasets.

The long time series analysis was only feasible with the low-resolution product (FireCCILT11). We first analysed the non-common period, covering from 1982 to 2000 (Figure 5.9). Small increase clusters were predominant with respect to large decrease clusters, although increase and decrease trend patterns were found regardless of the region. Africa (Northern tropical and SE), North America, Central South America, and West and Central Europe presented mostly positive trends, although in small regions and scattered, showing an increase of BA in this period. Eastern Europe, South America and Australia had large significant change in a few areas with negative trends. Asia presented both trends in Central, and increase trends in India.

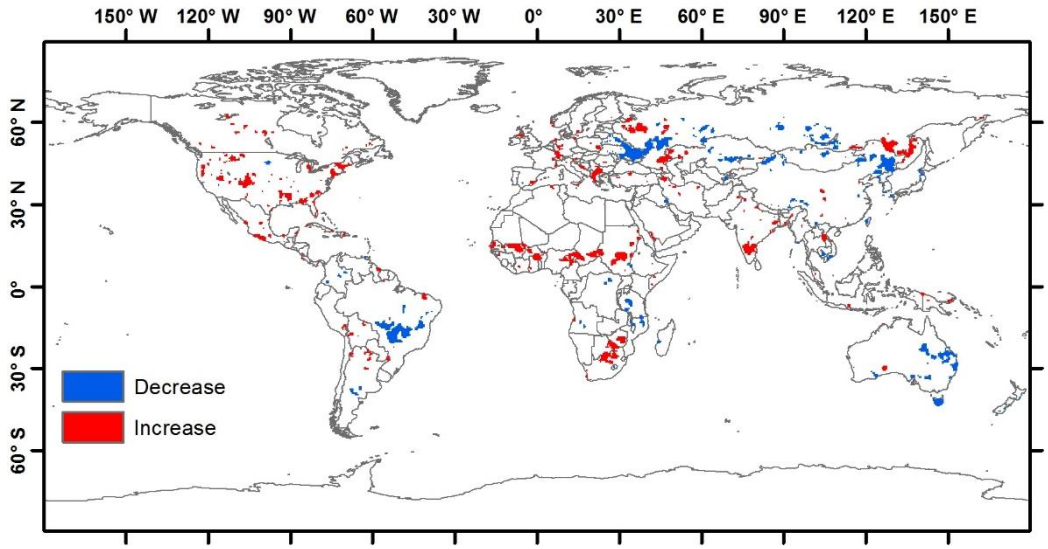

Figure 5.9. Significant trends of BA (with a confidence level of 95%) in the short-term series from 1982 to 2000 (FireCCILT11).

Comparing between periods of FireCCILT11, the first period (1982–2000) showed smaller clusters than the second period (2001–2018). The former period had more uncertainty than the latter period due to the AVHRR2 sensor had less quality than AVHRR3. The first period had more increase than decrease clusters, while in the second period the opposite occurred. The agreement and change of trend in the significant patterns are shown in Figure 5.10. The significant trends between periods did not coincide in the same places, although where those patterns concurred, a change of trend was widely predominant. Therefore, opposite trends between periods are found in Africa (Northern tropical and SE) and Central Asia (East and West). Small clusters of agreement in decrease trends are present in Central Africa (East), South America (Central) and Asia (East), and small clusters of agreement in increase trends are found in America (South and SE) and India. Europe and Australia did not present spatial disagreement in significant tends.

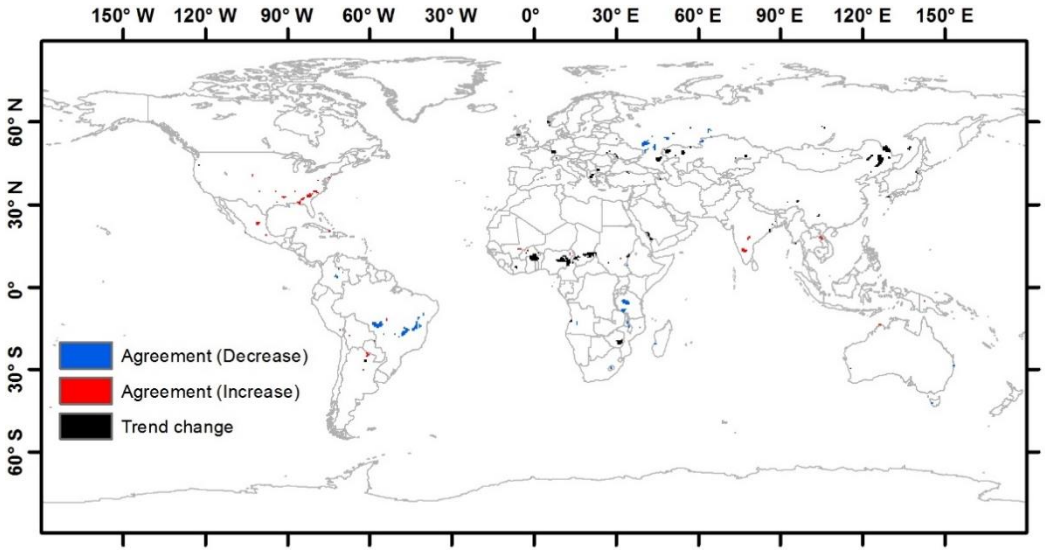

Figure 5.10. Spatial comparison (Agreement-Trend change) of significant trends between the 1982–2000 period and the 2001–2018 period of the FireCCILT11 BA product.

5.3.2.2. Long-Term Series

BA spatiotemporal trends in the full times series (1982–2018) of the BA dataset (FireCCILT11) showed larger regions with significant trends (Figure 5.11), which is related to the longer period.

Increase and decrease trends were found in every continent and region. Africa presented significant trends, mostly positive in the Northern Tropical (East, North and West) and Central region, and negative in the Northern Tropical (Centre), Eastern and South ones (Figure 5.11). South America had significant increase clusters in the borders

of the Amazon basin (Central and Southern Brazil), Peruvian Andes, the Chaco region and Southern Argentina, while regions with negative trends were found in Eastern Brazil, and Central and Northern Argentina. Central America areas (Petén, South of the Yucatan Peninsula in Guatemala, Central and Northeast Honduras) displayed significantly increasing trends. North America presented small clusters of BA increase in the North-West, Central and South-East regions, and decrease trends in Western regions and Eastern Canada. Europe showed significant BA increase (Northern and Eastern regions) and de-crease (Southern Spain). Western and Central Asia presented predominant decreasing trends and small increase clusters in the Southwest and east. Australia displayed increase clusters in the North and decreases in the South.

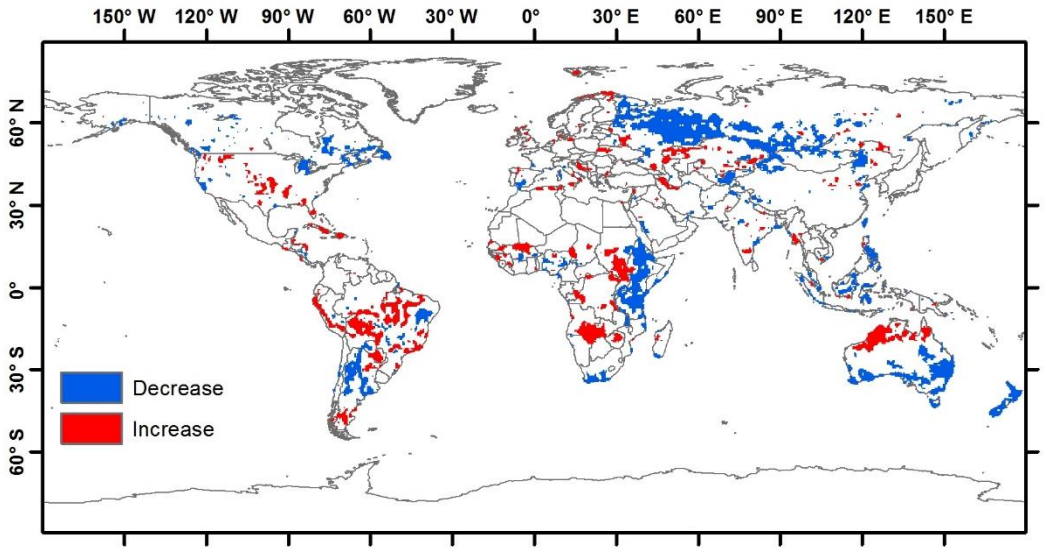

Figure 5.11. Significant trends of BA (with a confidence level of 95%) in the long-term series from 1982 to 2018 (FireCCILT11) at 0.5° resolution.

5.4. Discussion

This study developed a spatiotemporal analysis of global BA trends. The analysis was performed with two BA databases that include short-term (18 years) and long-term (37 years) time series.

FireCCILT11 presented a border effect (Otón et al. 2021b), and the AVHRR2 period showed anomalous trends or discontinuities, because the BA estimates from the 1982–2000 period had more uncertainty than those of the 2001–2018 period, since the AVHRR2 sensor had less quality than AVHRR3, although both periods are consistent (Otón et al. 2021a).

The spatial resolution of this study was 0.5°, common in other analysis (Carmona-Moreno et al. 2005; Yang et al. 2014), which implied a good balance between coverage and internal change. The lack of 1994 BA data was not relevant, because the database had many years of data and the methodology is robust against outliers. The corrections to remove temporal autocorrelations mitigated the impact of it, giving consistency to the datasets, and were applied in other trends (Neeti and Eastman 2011; Neeti et al. 2012) and BA studies (Silva et al. 2019). CMK were consistent methods that took into consideration a contextual approach to analyse spatiotemporal patterns. The contextual approach offered a significant cluster of trends, which are easier to detect than with other time series approaches (Neeti and Eastman 2011; Silva et al. 2019).

The use of two databases with different spatial resolution and temporal extent gives consistency to the study and results (Lizundia-Loiola et al. 2020a; Otón et al. 2021b) because this has allowed us to compare the results in common. This paper has illustrated the use of a long-term BA dataset, not previously available (FireCCILT11) including 37 years. The higher resolution product (FireCCI51) had a shorter time series, which has been analysed in previous studies (Bowman et al. 2020; Chuvieco et al. 2021; Lizundia-Loiola et al. 2020b). We observed that both higher and lower resolution BA datasets showed similar trends in all regions for the common observation period (2001–2018) except in Australia, which may be due in large part to spatial resolution. However, significant changes in trends were observed when comparing this period with the previous two decades, only available in the FireCCILT11 product. Finally, when using the long-term series (37 years), many more significant trends were observed than in the short periods (18 years).

Previous global analyses have shown a global decrease in BA (Andela et al. 2017; Earl and Simmonds 2018; Forkel et al. 2019). However, these studies are generally based on large continental regions, rather than on smaller regions (cells), being therefore affected by smoothing effects. In fact, regional analysis (Urbieta et al. 2019) have suggested that global analysis may be biased by the most burned regions, therefore blurring regional temporal trends. Moreover, it is well known that global BA datasets underestimate BA, particularly in regions with smaller fire patches (Laris 2005; Ramo et al. 2021; Roteta et al. 2019) because they are more capable to detect large fires. The difference in fire sizes detection could also affect the type of BA trends studied.

In both the short and the long time series analysed in this study, Africa presented the most important temporal trends, with a larger tendency to BA decrease, particularly in the most recent decades. A controversy was recently observed on whether those changes are related to increased cropland activity or to changes in precipitation patterns (Zubkova et al. 2019). However, when considering the longer time series, increases in

BA trends were observed in several regions of Northern and Southern tropical Africa, while Eastern Africa shows the most significant decreases (Figure 5.11).

In South America, the decrease in BA was predominant in our short-term series (2001–2018), likewise in Andela et al. (2017) and Forkel et al. (2019) studies, but when analysing the full time series, significant increases were observed in Central South America, which has been the most deforested region in the last decades (Song et al. 2018). North America showed a BA increase in both time series (Andela et al. 2017; Forkel et al. 2019), except in boreal regions which presented BA decrease in the long-term series.

Central Asia displayed a decrease in BA in both time series like Andela et al. (2017), Giglio et al. (2013), Hao et al. (2021) and Forkel et al. (2019), due to a wetter climate and increased grazing (Hao et al. 2021). In Northwest Asia, a change in forest use practices caused a BA decrease in long-term series (Ryzhkova et al. 2020). Finally, the Australian BA decreased in the north within the first years (Andela et al. 2017; Forkel et al. 2019) and increased in the long-term series, while the opposite happened in the south, although Andela et al. (2017) suggested BA decrease in the short time series (1998–2015).

Development of the global FireCCILT11 product relied on a spatial stratification based on the GFED regions, which has the potential to cause discontinuities in spatio-temporal BA patterns at the border between those regions. However, such effects are absent at the great majority of borders. In a few cases, it is possible that the exact location of a border effect will have been determined by the transition between GFED regions (most notably between Europe (EURO) and Boreal Asia (BOAS). However, we believe this is just the sharpening of actual, non-artefactual changes in trends, because there is evidence of steep gradients in fire drivers, not only at the Europe/Boreal Asia border, but also at the border between Boreal and Temperate North America. In the latter case, Jolly et al. (2015) found a rather abrupt change in trends of fire season length between the Western USA and Canadian sides of the border, with a strong increase in season length on the American side and no trend on the Canadian side, similarly to the BA trends we detected. Two re-cent studies support our detection of a decreasing BA trend in Western Russia, although not exactly overlapping the large patch shown in Figure 5.11. Wu et al. (2021) detected significantly negative BA trends, based on data from GFED4, which accounts for small fires (unlike the MODIS MCD64A1 and the FireCCI51 products). Ryzhkova et al. (2020) per-formed a dendrochronological study in Karelia, near the border with Finland and reported a decrease in BA, albeit over the period 1930–2000, much longer than those covered by satellite data. Drobyshev et al. (2021) provide additional indirect evidence, in the form of contrasting fire weather severity trends

(1901–2017) during the fire season, which de-creased in Scandinavia and increased in Western Russia. It is also worth noting that the patch with significantly decreasing BA trend detected in Western Russia, although very large, occurs in a region that does not burn extensively. We acknowledge that most of this evidence is circumstantial, but our analysis is unique in mapping BA annually stretching back to the early 1980 and, therefore, no independent BA data set is available for comparison with of our results.

5.5. Conclusions

This spatiotemporal analysis has shown the BA global trends and patterns in a long-term series. Understanding global BA trends and regional patterns is very important to elucidate the dynamics of fire occurrence and the effect of climate change. Mann-Kendall analysis showed BA trends in a contextual approach, displaying consistent patterns and clusters. Although the spatiotemporal analysis was robust and the patterns were consistent across products and other studies, the results must be carefully analysed, considering the abovementioned limitations of the FireCCILT11 product.

Spatiotemporal trends showed significant differences in the short and long-term series. The short-term series presented smaller significant clusters, and more scattered patterns, and the long-term series displayed larger significant clusters. The common time series in both products showed similar trends and high correlation, although FireCCI51 trends were more consistent and larger due to the original resolution. Comparing significant trends between both short periods (1982–2000 and 2001–2018) of the FireCCILT11 product, small agreement clusters were found and trend changes were common. Different trends in short-term periods and long-term periods were found due to different patterns present in the time series.

Future research will seek to interpret the causes of the BA trends detected. An analysis that relates BA trends with different variables, such as land cover, land use change and climate change, will improve understanding of fire regimes and their dynamics.

5.6. Acknowledgements

This research was funded by the ESA Climate Change Initiative (CCI) programme's Fire_cci project, contract number 4000126706/19/I-NB (https://climate.esa.int/en/projects/fire/, last accessed on 15 October 2021), by the Forest Research Centre, a research unit funded by Fundação para a Ciência e a Tecnologia I.P. (FCT), Portugal (UIDB/00239/2020), and by the Associated Laboratory TERRA.

5.7. References

Alaska Interagency Coordination Center (2021). Alaska Fire History perimeters 1940-2020. Available online: https://fire.ak.blm.gov/predsvcs/maps.php, last accessed on October 2021.

Andela, N., Morton, D.C., Giglio, L., Chen, Y., van der Werf, G.R., Kasibhatla, P.S., DeFries, R.S., Collatz, G., Hantson, S., & Kloster, S. (2017). A human-driven decline in global burned area. Science, 356, 1356-1362

Bowman, D., Williamson, G., Yebra, M., Lizundia-Loiola, J., Pettinari, M.L., Shah, S., Bradstock, R., & Chuvieco, E. (2020). Wildfires: Australia needs national monitoring agency. Nature, 584, 188-191

Canadian Forest Service (2017). Canadian National Fire Database – Agency Fire Data. Natural Resources Canada, Canadian Forest Service, Northern Forestry Centre, Edmonton, Alberta. Available online: http://cwfis.cfs.nrcan.gc.ca/ha/nfdb, last accessed on October 2021.

Carmona-Moreno, C., Belward, A., Malingreau, J.P., Hartley, A., Garcia-Alegre, M., Antonovskiy, M., Buchshtaber, V., & Pivovarov, V. (2005). Characterizing interannual variations in global fire calendar using data from Earth observing satellites. Global Change Biology, 11, 1537-1555

Copernicus (2019). Algorithm Theoretical Basis Document, ICDR Land Cover 2016. Copernicus Climate Change Service: Louvain, Belgium, 62p. Available online: https://cds.climate.copernicus.eu/, last accessed on October 2021.

Copernicus Programme (2021). Land cover classification gridded maps from 1992 to present derived from satellite observations. Available online: https://cds.climate.copernicus.eu/cdsapp#!/dataset/satellite-land-cover, last accessed on October 2021.

Chandler, R., & Scott, M. (2011). Statistical methods for trend detection and analysis in the environmental sciences. United Kingdom: John Wiley & Sons

Chuvieco, E., Lizundia-Loiola, J., Pettinari, M.L., Ramo, R., Padilla, M., Tansey, K., Mouillot, F., Laurent, P., Storm, T., & Heil, A. (2018). Generation and analysis of a new global burned area product based on MODIS 250 m reflectance bands and thermal anomalies. Earth System Science Data, 10, 2015-2031

Chuvieco, E., Mouillot, F., van der Werf, G.R., San Miguel, J., Tanasse, M., Koutsias, N., García, M., Yebra, M., Padilla, M., & Gitas, I. (2019). Historical background and current

developments for mapping burned area from satellite Earth observation. Remote Sensing Of Environment, 225, 45-64

Chuvieco, E., Pettinari, M.L., Koutsias, N., Forkel, M., Hantson, S., & Turco, M. (2021). Human and climate drivers of global biomass burning variability. Science of the Total Environment, 779, 146361

Douglas, E., Vogel, R., & Kroll, C. (2000). Trends in floods and low flows in the United States: impact of spatial correlation. Journal of Hydrology, 240, 90-105

Drobyshev, I., Ryzhkova, N., Eden, J., Kitenberga, M., Pinto, G., Lindberg, H., Krikken, F., Yermokhin, M., Bergeron, Y., & Kryshen, A. (2021). Trends and patterns in annually burned forest areas and fire weather across the European boreal zone in the 20th and early 21st centuries. Agricultural and Forest Meteorology, 306, 108467

Durbin, J., & Watson, G.S. (1950). Testing for serial correlation in least squares regression: I. Biometrika, 37, 409-428

Earl, N., & Simmonds, I. (2018). Spatial and temporal variability and trends in 2001–2016 global fire activity. Journal of Geophysical Research: Atmospheres, 123, 2524-2536

Eastman, J.R., Sangermano, F., Ghimire, B., Zhu, H., Chen, H., Neeti, N., Cai, Y., Machado, E.A., & Crema, S.C. (2009). Seasonal trend analysis of image time series. International Journal of Remote Sensing, 30, 2721-2726

ESA (2013). Land Cover CCI: Algorithm Theoretical Basis Document Version 2., ESA: Louvain, Belgium, 191p. Available online: https://climate.esa.int/media/documents/Land_Cover_CCI_ATBDv2_2.3.pdf, last accessed on October 2021.

European Space Agency and Fire_cci project team (2021). Fire. Available online: https://climate.esa.int/en/odp/#/dashboard, last accessed on October 2021.

Forkel, M., Dorigo, W., Lasslop, G., Chuvieco, E., Hantson, S., Heil, A., Teubner, I., Thonicke, K., & Harrison, S.P. (2019). Recent global and regional trends in burned area and their compensating environmental controls. Environmental Research Communications, 1, 051005

Fuller, D.O., & Wang, Y. (2014). Recent trends in satellite vegetation index observations indicate decreasing vegetation biomass in the southeastern saline everglades wetlands. Wetlands, 34, 67-77

GCOS (2016). The Global Observing System for Climate: Implementation Needs. Geneva, Switzerland: GCOS-200. World Meteorological Organization

Giglio, L., Boschetti, L., Roy, D.P., Humber, M.L., & Justice, C.O. (2018). The Collection 6 MODIS burned area mapping algorithm and product. Remote Sensing Of Environment, 217, 72-85

Giglio, L., Randerson, J.T., & Werf, G.R. (2013). Analysis of daily, monthly, and annual burned area using the fourth generation global fire emissions database (GFED4). Journal of Geophysical Research: Biogeosciences, 118, 317-328

Granier, C., Bessagnet, B., Bond, T., D'Angiola, A., van Der Gon, H.D., Frost, G.J., Heil, A., Kaiser, J.W., Kinne, S., & Klimont, Z. (2011). Evolution of anthropogenic and biomass burning emissions of air pollutants at global and regional scales during the 1980–2010 period. Climatic Change, 109, 163-190

Hantson, S., Arneth, A., Harrison, S.P., Kelley, D.I., Prentice, I.C., Rabin, S.S., Archibald, S., Mouillot, F., Arnold, S.R., & Artaxo, P. (2016). The status and challenge of global fire modelling. Biogeosciences, 13, 3359-3375

Hao, W.M., Reeves, M.C., Baggett, L.S., Balkanski, Y., Ciais, P., Nordgren, B.L., Petkov, A., Corley, R.E., Mouillot, F., & Urbanski, S.P. (2021). Wetter environment and increased grazing reduced the area burned in northern Eurasia from 2002 to 2016. Biogeosciences, 18, 2559-2572

Jolly, W.M., Cochrane, M.A., Freeborn, P.H., Holden, Z.A., Brown, T.J., Williamson, G.J., & Bowman, D.M. (2015). Climate-induced variations in global wildfire danger from 1979 to 2013. Nature communications, 6, 1-11

Kendall, M.G. (1975). Rank correlation methods. London: Charles Griffin

Laris, P.S. (2005). Spatiotemporal problems with detecting and mapping mosaic fire regimes with coarse-resolution satellite data in savanna environments. Remote Sensing Of Environment, 99, 412-424

Lizundia-Loiola, J., Otón, G., Ramo, R., & Chuvieco, E. (2020a). A spatio-temporal active-fire clustering approach for global burned area mapping at 250 m from MODIS data. Remote Sensing Of Environment, 236, 111493

Lizundia-Loiola, J., Pettinari, M.L., & Chuvieco, E. (2020b). Temporal Anomalies in Burned Area Trends: Satellite Estimations of the Amazonian 2019 Fire Crisis. Remote Sensing, 12, 151

Mann, H.B. (1945). Nonparametric tests against trend. Econometrica: Journal of the econometric society, 13, 245-259

Mishra, N.B., Crews, K.A., Neeti, N., Meyer, T., & Young, K.R. (2015). MODIS derived vegetation greenness trends in African Savanna: Deconstructing and localizing the role of changing moisture availability, fire regime and anthropogenic impact. Remote Sensing Of Environment, 169, 192-204

Mouillot, F., Schultz, M.G., Yue, C., Cadule, P., Tansey, K., Ciais, P., & Chuvieco, E. (2014). Ten years of global burned area products from spaceborne remote sensing—A review: Analysis of user needs and recommendations for future developments. International Journal of Applied Earth Observation and Geoinformation, 26, 64-79

Neeti, N., & Eastman, J.R. (2011). A Contextual Mann-Kendall Approach for the Assessment of Trend Significance in Image Time Series. Transactions in GIS, 15, 599-611

Neeti, N., Rogan, J., Christman, Z., Eastman, J.R., Millones, M., Schneider, L., Nickl, E., Schmook, B., Turner, B.L., & Ghimire, B. (2012). Mapping seasonal trends in vegetation using AVHRR-NDVI time series in the Yucatán Peninsula, Mexico. Remote Sensing Letters, 3, 433-442

North Australia & Rangelands Fire Information (2021). Fire scars. Available online: www.firenorth.org.au/nafi2, last accessed on October 2021.

Otón, G., Franquesa, M., Lizundia-Loiola, J., & Chuvieco, E. (2021a). Validation of low spatial resolution and no-dichotomy global long-term Burned Area product by Pareto Boundary. Proc. SPIE 11863, Earth Resources and Environmental Remote Sensing/GIS Applications XII, 1186313.

Otón, G., Lizundia-Loiola, J., Pettinari, L., & Chuvieco, E. (2021b). Development of a Consistent Global Long-Term Burned Area product (1982-2018) based on AVHRR-LTDR data. International Journal of Applied Earth Observation and Geoinformation, 103, 102473

Otón, G., Ramo, R., Lizundia-Loiola, J., & Chuvieco, E. (2019). Global Detection of Long-Term (1982–2017) Burned Area with AVHRR-LTDR Data. Remote Sensing, 11, 2079

Pedelty, J., Devadiga, S., Masuoka, E., Brown, M., Pinzon, J., Tucker, C., Vermote, E., Prince, S., Nagol, J., Justice, C., Roy, D., Ju, J., Schaaf, C., Liu, J., Privette, J., & Pinheiro, A. (2007). Generating a long-term land data record from the AVHRR and MODIS instruments. In, Geoscience and Remote Sensing Symposium, 2007. IGARSS 2007. IEEE International (pp. 1021-1025): IEEE

Ramo, R., Roteta, E., Bistinas, I., Van Wees, D., Bastarrika, A., Chuvieco, E., & Van der Werf, G.R. (2021). African burned area and fire carbon emissions are strongly impacted by small fires undetected by coarse resolution satellite data. Proceedings of the National Academy of Sciences, 118, 1-7

Roteta, E., Bastarrika, A., Padilla, M., Storm, T., & Chuvieco, E. (2019). Development of a Sentinel-2 burned area algorithm: Generation of a small fire database for sub-Saharan Africa. Remote Sensing Of Environment, 222, 1-17

Ryzhkova, N., Pinto, G., Kryshen, A., Bergeron, Y., Ols, C., & Drobyshev, I. (2020). Multi-century reconstruction suggests complex interactions of climate and human controls of forest fire activity in a Karelian boreal landscape, North-West Russia. Forest Ecology and Management, 459, 117770

Sen, P.K. (1968). Estimates of the regression coefficient based on Kendall's tau. Journal of the American Statistical Association, 63, 1379-1389

Silva, J.M., Moreno, M.V., Le Page, Y., Oom, D., Bistinas, I., & Pereira, J.M.C. (2019). Spatiotemporal trends of area burnt in the Iberian Peninsula, 1975–2013. Regional Environmental Change, 19, 515-527

Song, X.-P., Hansen, M.C., Stehman, S.V., Potapov, P.V., Tyukavina, A., Vermote, E.F., & Townshend, J.R. (2018). Global land change from 1982 to 2016. Nature, 560, 639-643

Theil, H. (1950). A rank-invariant method of linear and polynomial regression analysis. Indagationes mathematicae, 12, 173

Urbanski, S.P., Hao, W.M., & Baker, S. (2008). Chemical composition of wildland fire emissions. Developments in Environmental Science, 8, 79-107

Urbieta, I.R., Franquesa, M., Viedma, O., & Moreno, J.M. (2019). Fire activity and burned forest lands decreased during the last three decades in Spain. Annals of Forest Science, 76, 1-13

Wang, X.L., & Swail, V.R. (2001). Changes of extreme wave heights in Northern Hemisphere oceans and related atmospheric circulation regimes. Journal of Climate, 14, 2204-2221

Ward, D., Kloster, S., Mahowald, N., Rogers, B., Randerson, J., & Hess, P. (2012). The changing radiative forcing of fires: global model estimates for past, present and future. Atmospheric Chemistry and Physics, 12.10857–10886.

Wu, C., Venevsky, S., Sitch, S., Mercado, L.M., Huntingford, C., & Staver, A.C. (2021). Historical and future global burned area with changing climate and human demography. One Earth, 4, 517-530

Yang, J., Tian, H., Tao, B., Ren, W., Kush, J., Liu, Y., & Wang, Y. (2014). Spatial and temporal patterns of global burned area in response to anthropogenic and environmental factors: Reconstructing global fire history for the 20th and early 21st centuries. Journal of Geophysical Research: Biogeosciences, 119, 249-263

Yue, S., & Wang, C.Y. (2002). Regional streamflow trend detection with consideration of both temporal and spatial correlation. International Journal of Climatology: A Journal of the Royal Meteorological Society, 22, 933-946

Zubkova, M., Boschetti, L., Abatzoglou, J.T., & Giglio, L. (2019). Changes in fire activity in Africa from 2002 to 2016 and their potential drivers. Geophysical Research Letters, 46, 7643-7653

Capítulo 6

CONCLUSIONES

El estudio del clima y el cambio climático necesitan de datos fiables y de la mayor extensión temporal posible para obtener resultados consistentes que nos ayuden a entender mejor su funcionamiento. Los productos de área quemada aportan valiosa información, a pesar de que sus series temporales son limitadas. Hasta la realización de esta tesis solo se disponían de datos globales y consistentes con la entrada del sensor MODIS en el año 2001. A pesar de que existían imágenes terrestres globales desde 1981, no se había generado ningún producto global de área quemada debido a la cantidad de limitaciones que estos datos presentaban.

Esta tesis ha desarrollado y analizado un nuevo producto global de área quemada, basado en un prototipo inicial, capaz de detectar área quemada y de lidiar con las numerosas limitaciones que presentaban los datos de entrada. El producto presenta un algoritmo novedoso, diseñado con detalle para hacer frente a los problemas presentados. El resultado es un producto consistente y coherente tanto global como regionalmente, con la serie temporal más larga posible (1982-2018). El producto ha permitido el estudio de tendencias espacio-temporales de área quemada para una serie temporal nunca antes desarrollada con teledetección.

A continuación, se muestran los puntos más destacados de este proceso:

- Las limitaciones asociadas a los datos AVHRR y al producto LTDR son de gran importancia, tanto que son capaces de alterar los resultados de área quemada. La resolución espacial, la consistencia temporal entre satélites, la degradación de los sensores, la inconsistencia del infrarrojo medio, las carencias de la capa de nubes, la ausencia de fuegos activos y la falta de datos, son limitaciones que influyeron en el desarrollo del algoritmo. Cada una de ellas tuvo que ser analizada minuciosamente y darle una solución operativa para que no afectase al producto.
- Compuestos mensuales, áreas no combustibles e índices espectrales son comúnmente utilizados en productos de área quemada, pero fueron acompañados de una nueva visión de algoritmo. Para ello, se creó una nueva mascara de nubes basada en un análisis de criterios, un novedoso índice sintético que agrupaba la información de entrada para realzar la señal de quemado, perfiles anuales de los datos, entrenamiento con los productos más preciosos de área quemada, modelos mensuales de RF globales y boreales para una mejor comprensión de las señales, criterios innovadores para convertir las probabilidades de RF a clasificaciones binarias de área quemada teniendo en cuenta las respuesta de cada imagen, el periodo al que pertenecía cada una de ellas, las regiones continentales, y la degradación de los satélites y los sensores.

Además, por primera vez en un producto de área quemada se ofrecieron proporciones de quemado a cada pixel como resultado.

- La evaluación de este novedoso producto de área quemada se llevó a cabo inter-comparándolo con productos MODIS de área quemada globales. Las correlaciones fueron altas, mostrando relaciones mensuales con los productos MCD64A1 (r = 0.89, %MAE = 21%) y FireCCI51 (r = 0.95, %MAE = 10%) durante las series temporales comunes. También se obtuvieron altas correlaciones con los perímetros oficiales que se extendían a la época pre-MODIS, como (Australia: r = 0.89, %MAE = 26%; Canadá: r = 0.81, %MAE = 33%; Alaska: r = 0.96, %MAE = 42%). Además, la degradación de los satélites no influyó a los patrones de área quemada en la serie temporal, y las zonas boreales tuvieron resultados precisos.
- La validación fue novedosa al realizar a una serie temporal de casi 30 años, debido a las limitaciones que también presenta hacer perímetros históricos de validación con Landsat. El producto mostró mayor omisión que comisión, subestimando área quemada como la mayoría de productos. La baja resolución presenta un error asociado a su pérdida de variabilidad. El producto presentó un buen comportamiento y el uso de proporciones fue capaz de reducir errores. Los datos del periodo AVHRR2 del producto tienen mayor incertidumbre que AVHRR3 debido a la calidad de los sensores, aunque ambos periodos son consistentes.
- A pesar de los resultados consistentes, el producto presenta ciertas limitaciones, tales como la baja resolución espacial y potenciales efectos borde debido al uso de regiones continentales en el diseño del algoritmo.

El producto fue analizado espacial y temporalmente debido a que demostró un gran comportamiento y consistencia a pesar de las limitaciones. La serie temporal que hemos trabajado en el producto permite, por primera vez, estudiar tendencias que se extienden casi cuarenta años. De esta manera, podemos comprender mejor las dinámicas de ocurrencia del fuego y el efecto del clima.

Las tendencias espacio-temporales mostraron diferencias significativas entre las series temporales cortas, comparadas con FireCCI51, y largas. Las series temporales cortas presentaron tendencias más pequeñas y dispersas que las series temporales largas. El producto desarrollado en esta tesis reveló tendencias de disminución de área quemada en África oriental, regiones boreales, Asia central y el sur de Australia, y tendencias de aumento de área quemada en África occidental y central, Sudamérica, USA y el norte de Australia.

Por lo tanto, este nuevo producto es el único consistente y global con una serie temporal larga desde 1982 hasta 2018. El producto fue diseñado para que pueda complementar

los actuales productos de área quemada de mayor resolución, los cuales tiene series temporales más cortas. Además, este producto fue basado en AVHRR, un sensor diferente a los utilizados para productos de área quemada con series temporales medias como MODIS.

6.1. Líneas futuras de investigación

La presente tesis puede servir como punto de partida para futuros estudios. Por un lado, en el plano de utilidad del producto, mejorando la comprensión de los regímenes de incendios y sus dinámicas, mediante:

- La búsqueda de interpretación de las causas de las tendencias de área quemada.
- La relación de las tendencias de área quemada con diferentes variables como *land cover*, cambios de uso del suelo y cambio climático.

Y, por otro lado, desarrollando nuevas metodologías o mejorando los datos de entrada.

- El potencial de *Deep Learning* y las *Convolutional Neural Network* (CNN) podría ser de gran interés para trabajar con estos datos, aportando un nuevo concepto de entrenamiento y una mejor adaptación regional. Además, de que es un enfoque no utilizado en detección de área quemada con resoluciones bajas.
- La corrección de la degradación del sensor en los datos originales del LTDR también sería un gran avance que ofrecería datos más fiables al desarrollo del algoritmo.